CHEMICAL REVIEWS

pubs.acs.org/CR Review

Understanding the Electric Double-Layer Structure, Capacitance, and Charging Dynamics

Jianzhong Wu*

Cite This: https://doi.org/10.1021/acs.chemrev.2c00097 Read Online

ACCESS | Metrics & More | Article Recommendations

ABSTRACT: Significant progress has been made in recent years in theoretical modeling of the electric double layer (EDL), a key concept in electrochemistry important for energy storage, electrocatalysis, and multitudes of other technological applications. However, major challenges remain in understanding the microscopic details of the electrochemical interface and charging mechanisms under realistic conditions. This review delves into theoretical methods to describe the equilibrium and dynamic responses of the EDL structure and capacitance for electrochemical systems commonly deployed for capacitive energy storage. Special emphasis is given to recent advances that intend to capture the nonclassical EDL behavior such as oscillatory ion distributions, polarization of nonmetallic electrodes, charge transfer, and various forms of phase transitions in the micropores of electrodes interfacing with an organic electrolyte or ionic liquid. This comprehensive analysis highlights theoretical insights into predictable relationships between materials characteristics and electrochemical performance and offers a perspective on opportunities for further development toward rational design and optimization of electrochemical systems.

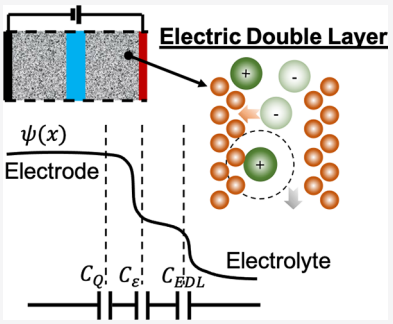

CONTENTS

Special Issue: Computational Electrochemistry

Received: February 7, 2022

1. INTRODUCTION

The interfacial region between an electrode and an electrolyte is highly inhomogeneous in terms of both the electronic density and the spatial distributions of ionic species and solvent molecules. The accumulation of counterions near the electrode surface, concomitant with the depletion of co-ions, is conventionally referred to as the electric double layer (EDL), a concept originally proposed by Helmholtz in 1853.[1] Owing to its fundamental importance in electrochemical energy storage and chemical conversions, the EDL has been emerging as a focal point of both fundamental and applied research in materials chemistry and physics as well as multitudes of engineering disciplines.[2,3]

As shown schematically in Figure 1, the EDL model proposed by Helmholtz consists of two mathematical planes with equal

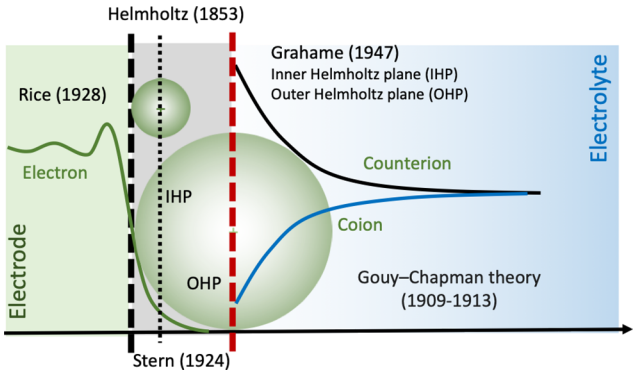

Figure 1. Classical models of the electric double layer (EDL).

but opposite electrical charges, one standing for electrode surface and the other for counterions. The separation between the two parallel planes (viz., double layer) is comparable to the counterion radius, yielding a capacitance that is larger than the typical value of a dielectric capacitor by many orders of magnitude. In practice, an EDL capacitor is typically made of porous electrodes and a concentrated electrolyte or ionic liquid in order to maximize the total capacitance. Alternatively known as supercapacitors or ultracapacitors, EDL capacitors hold great promise for the next generation of electrical energy storage, deionization, blue-energy harvesting, and many other technological applications.[4−10]

Despite its simplicity, the Helmholtz model predicts the EDL capacitance in proper order of magnitude and, thus, often serves as a useful rule of thumb in practical application. While the double-layer model captures the essential features of charge separation or polarization effects due to an applied voltage, it provides little information about the microscopic details of the electrode−electrolyte interface. The inhomogeneous distributions of ionic species near an electrode surface were first described by Gouy in 1909[11] and, independently, by Chapman[12] using the Poisson−Boltzmann (PB) theory. About a decade later, Stern modified the Gouy−Chapman (GC) theory by dividing the electrolyte region into an inner layer not accessible to the ionic species (a.k.a., the Stern layer) and a diffuse layer accounting for the inhomogeneous ion distributions.[13] According to the Stern model, the EDL capacitance is composed of two components reflecting the sequential charge distributions in the inner layer and the diffuse layer

$$\frac{1}{C_{\mathrm{GCS}}} = \frac{1}{C_{\mathrm{inner}}} + \frac{1}{C_{\mathrm{diffuse}}} \tag{1}$$

where C stands for areal capacitance. With further assumptions for the local dielectric constant, the Stern model is able to reproduce experimental data for the EDL capacitance.[14] To take into account specific ion adsorption at the electrode surface, Graham extended the Stern model by distinguishing between solvated and bare ions and introduced the notion of inner and outer Helmholtz planes (IHP and OHP) according to their closest distances from the electrode surface.[15] The definitions of IHP and OHP are necessarily empirical because, from a molecular perspective, neither ion solvation nor the solvent structure at the electrochemical interface is well understood even today. Besides, the serial connection of different contributions to the capacitance is valid only at conditions with a zero potential gradient far away from the electrode surface.[16] The assumption may not be valid for EDLs in a confined space like those for porous electrodes. Nevertheless, these classical concepts of EDL facilitate better understanding of diverse electrochemical processes including ion intercalation, charge transfer, and surface reactions as commonly encountered in capacitive energy storage.

Liquid-state theories were introduced to account for molecular excluded-volume effects on ion distributions in the diffuse layer in the early 1960s.[17] For the first few decades, the theoretical investigations were mostly based on the integral-equation theories or various modifications of the PB equation.[18−20] In 1980, Evans and Sluckin first used classical density functional theory (cDFT) to describe the interfacial properties of charged fluids.[21] As a generic statistical-mechanical procedure naturally applicable to inhomogeneous ionic systems, cDFT has evolved into one of the most popular choices to predict the EDL structure, capacitance, and dynamic behavior.[22−25] While theoretical studies of the diffuse layer are mostly focused on ion distributions, the electronic structure of an electrode has a life of its own. The electronic density of a metallic surface was considered by Rice as early as 1928 based on the Sommerfeld theory of free electrons.[26] Regrettably, little progress was made toward a more accurate description of the electronic structure before the landmark publications by Lang and Kohn on the theory of metal surfaces in the early 1970s.[27,28] An integrated approach to account for both the electronic and ionic density profiles in the EDL has been explored since the 1980s and remains an active field of theoretical development today.[29−32]

The classical EDL models provide useful intuition for understanding a wide range of electrochemical phenomena. However, they do not reflect the whole picture even for relatively simple systems such as a dilute solution of monovalent ions in contact with a perfect metal. Based on the experimental data for the capacitance of a mercury electrode in contact with an aqueous electrolyte solution, Watts-Tobin and Mott predicted additional contributions to the capacitance due to the adsorption of mercury atoms and charge transfer at the electrode−electrolyte interface and due to the reduction of the dielectric constant of water in the inner region of the EDL.[33,34] More recent experiments and theoretical analyses provide direct evidence that solvent molecules, water in particular, are highly organized near a charged surface.[35] The local electric field reduces the molecular polarizability while elevating the average

https://doi.org/10.1021/acs.chemrev.2c00097
Chem. Rev. XXXX, XXX, XXX−XXX

density in comparison to those in the bulk solution, which may lead to a negative capacitance.[36,37] Besides, the chemisorption of ionic species results in changes in the electronic structure of the electrode that cannot be faithfully described by conventional surface reaction models yet are important for understanding nonclassical charging behavior including negative double-layer capacitance and pseudocapacitance.[14,36,38] As the electrolyte concentration increases, the EDL structure exhibits a transition from the Langmuir-type charge compensation to nonclassical charge overscreening and alternative layering of cations and anions.[39] The electrified surface may induce the nucleation of nanocrystals at a threshold concentration that is significantly lower than the bulk solubility limit. Surface crystallization was reported both at a metallic surface[40] and at the vapor−liquid interface of an ionic liquid above the bulk melting temperature.[41] The overscreening of the surface charge and oscillatory ion distributions are magnified for systems containing multivalent ions, ionic liquids, or organic electrolytes of low dielectric constant.[42] The nonclassical behavior of the EDL structure is manifested not just in terms of one-dimensional solvent inhomogeneity or oscillatory ion distributions; they are also evident from the in-plane organization of ionic species and various forms of surface phase transitions.[43,44] To a certain degree, surface phase transition may be expected from the two-dimensional Wigner crystallization or structure ordering of charged particles.[45] However, for ion distributions near a charged surface, phase transition may also take place off-plane reminiscent to surface wetting transitions.[46] The EDL structure is necessarily more complicated for electrolytes within the micropores of electrodes that are commonly utilized for energy storage.[43] In addition to the nonclassical EDL behavior corresponding to a planar surface mentioned above, the physicochemical properties are influenced by the pore size, shape, and surface chemistry. Besides, ionic liquids and organic electrolytes confined within the micropores of an electrode may experience capillary evaporation as well as wetting transitions.[47]

In this review, we take a broad view of theoretical efforts that aim to capture nonclassical EDL structure and dynamic behavior with particular attention to their applications to capacitive energy storage. Various EDL models are presented with a brief historical background in order to highlight the evolution of ideas and facilitate comparison between different approaches. Theoretical predictions of the EDL capacitance are discussed in the context of recent research activities driven by the practical need to improve the energy and power density of supercapacitors. Charging dynamics is discussed mostly from the viewpoint of "local equilibrium thermodynamics" without considering correlation effects on transport coefficients. It should be noted that this review is primarily focused on analytical and semianalytical EDL models derived from a microscopic perspective. Complementary reviews are available summarizing recent research for a better understanding of the EDL through molecular simulation and experiment.[48−53] A comprehensive discussion of conventional EDL methods is referred to the classical texts of electrochemistry (e.g., refs 54−57). In terms of the time frame, this review intends to cover the theoretical progress over the past decade, approximately from 2011 through 2021. Although we have strived to analyze the majority of theoretical work on nonreactive EDL, undoubtedly some important publications might have been left out but not with intention.

2. THEORETICAL METHODS

Approximately, recent developments of equilibrium EDL models may be categorized into the following three major directions: 1) mean-field methods plus corrections for electrostatic correlation aiming to capture the self-organization and phase behavior of ionic fluids in confined geometries; 2) classical density functional theory (cDFT) for representing the EDL capacitance and electrosorption in nanoporous electrodes; and 3) integration of electronic structure methods with the conventional EDL theories. In parallel with theoretical developments, molecular simulation has been playing a pivotal role in acquiring a molecular-level understanding of the capacitive behavior of porous electrodes in concentrated electrolytes, room-temperature ionic liquids (ILs), and solvent-in-salt systems.[51,58]

2.1. What Is Missed in the Poisson−Boltzmann Equation?

The Poisson−Boltzmann (PB) equation is fundamental to the conventional EDL models as well as new developments including those in combination with first-principle calculations. In its original form, the PB equation is concerned with the distribution of point charges in a dielectric continuum as represented by the number densities of ionic species, $\rho_i(\mathbf{r})$. For such a system, the intrinsic Helmholtz energy is given by[59]

$$F = \int d\mathbf{r}[f_{is} + f_c(\psi, q)] \tag{2}$$

where f_{is} corresponds to that for an ideal solution (is)

$$f_{is} = k_B T \sum_i \rho_i(\mathbf{r})[\ln \rho_i(\mathbf{r})\Lambda_i^3 - 1] \tag{3}$$

where Λ_i stands for the thermal wavelength of species i, k_B stands for the Boltzmann constant, T stands for absolute temperature, and $f_c(\psi, q)$ denotes the local density of electrostatic energy due to the Coulomb interactions. According to the mean-field approximation, the latter is affiliated with the local electrical potential $\psi(\mathbf{r})$ and local charge density $q(\mathbf{r})$

$$f_c(\psi, q) = -\frac{\epsilon}{2}|\nabla\psi|^2 + q\psi \tag{4}$$

where ϵ is the background permittivity. In many publications, the permittivity is written as $\epsilon = \epsilon_0\epsilon_r$ with ϵ_0 denoting the permittivity of the free space and ϵ_r denoting the dielectric constant or relative permittivity.

In an electrolyte solution, the local charge density $q(\mathbf{r})$ is uniquely determined by the number densities of ionic species and ion valence Z_i

$$q(\mathbf{r}) = \sum_i \rho_i(\mathbf{r}) Z_i e \tag{5}$$

where e denotes the unit charge. Noting the variational relation

$$\frac{\delta \int \mathrm{d}\mathbf{r} f_c(\psi, q)}{\delta\psi} = \frac{\partial f_c(\psi, q)}{\partial\psi} - \nabla\frac{\partial f_c(\psi, q)}{\partial\nabla\psi} \tag{6}$$

we obtain the Poisson equation by minimizing the Helmholtz energy given by eq 2 with respect to the electrical potential

$$\nabla^2\psi = -\frac{q(\mathbf{r})}{\epsilon} \tag{7}$$

Meanwhile, the functional derivative of the Helmholtz energy with respect to the ion density leads to the Boltzmann distribution

https://doi.org/10.1021/acs.chemrev.2c00097
Chem. Rev. XXXX, XXX, XXX−XXX

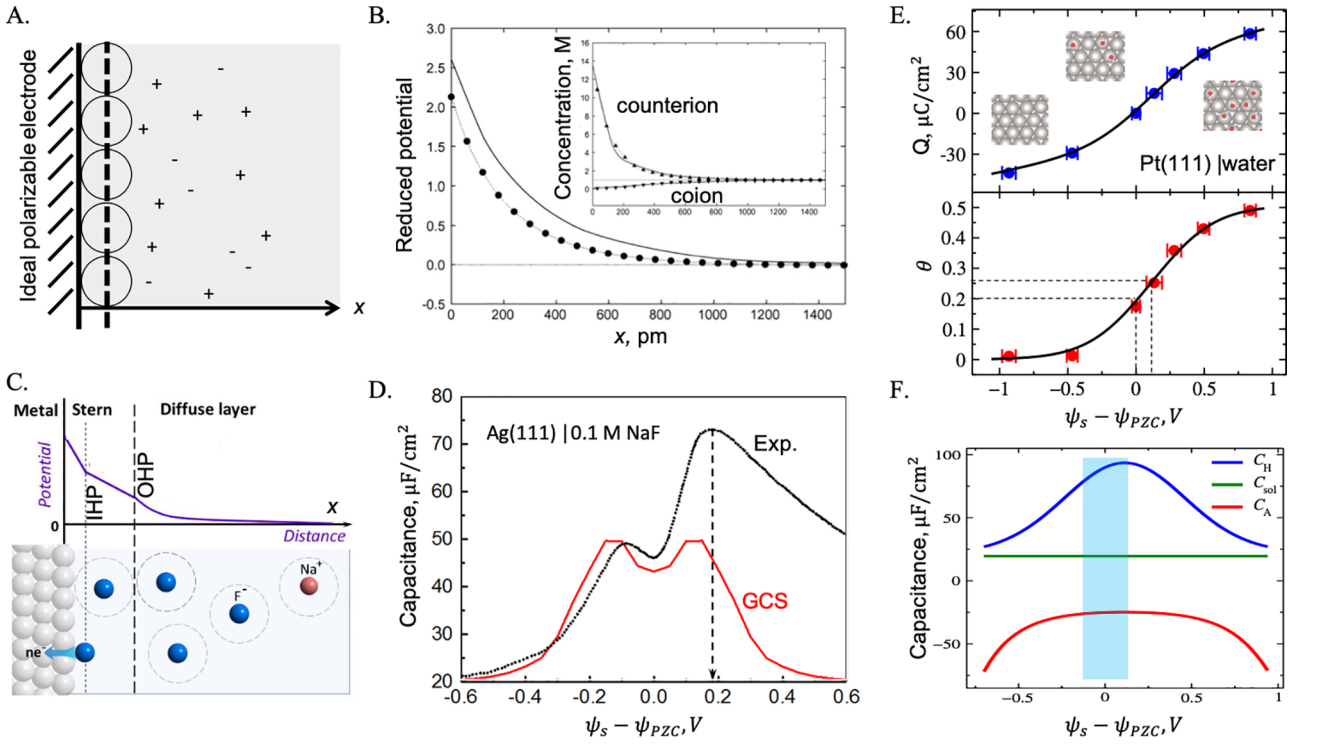

Figure 2. Electric double layer at the interface of a perfect metal and a dilute electrolyte solution. A. Schematic of the Gouy−Chapman-Stern (GCS) model for ion distributions near an ideal polarizable electrode (IPE). B. A comparison of the GCS theory (solid lines) with Monte Carlo (MC) simulation (symbols) for a 1 M monovalent electrolyte in contact with a hard wall with surface charge density $Q = 20\ \mu C/cm^2$. The simulation was based on charged hard spheres with a radius of 0.3 nm for both ionic species. C. The Grahame model with partial charge transfer at a metal−electrolyte interface. D. Comparison of the GCS theory with experimental capacitance for silver metal in a 0.1 M NaF solution at different surface potentials (ψ_s). The difference between theory and experiment may be attributed to the chemisorption of F^- ions at the silver surface. E. Surface charge density (Q) and coverage of chemisorbed water molecules (θ) at the Pt(111) surface calculated from *ab initio* molecular dynamics (MD) simulation. F. Decomposition of the Helmholtz capacitance C_H into the solvent capacitance C_{sol} and the chemisorption capacitance C_A. Here $C_{sol} \approx 20\ \mu F/cm^2$ was estimated from the dielectric constant of water. (B) Reproduced with permission from ref 60. Copyright 2009 Elsevier. (C and D) Reproduced with permission from ref 14. Copyright 2021 American Physical Society. (E and F) Reproduced with permission from ref 37. Copyright 2020 AAAS.

$$\rho_i(\mathbf{r}) = \frac{1}{\Lambda_i^3} \exp\{-\beta[Z_i e\psi(\mathbf{r}) - \mu_i]\} = \rho_i^0 \exp[-\beta Z_i e\psi(\mathbf{r})] \tag{8}$$

where $\mu_i = \delta F/\delta\rho_i(\mathbf{r})$ is the chemical potential of species i, $\beta = 1/(k_B T)$, and ρ_i^0 is the ion density in the bulk. The second equality in eq 8 follows that the electrical potential vanishes in the bulk phase, $\psi(\infty) = 0$, and $\beta\mu_i = \ln(\rho_i^0 \Lambda_i^3)$.

As shown schematically in Figure 2A, the GC theory corresponds to the application of the PB equation to a symmetrical electrolyte ($Z_+ = -Z_- = Z$ and $\rho_+^0 = \rho_-^0 = \rho_0$) near a planar wall of uniform charge density Q. In this case, the local charge density is given by

$$q(x) = -2\rho_0 Ze \sinh[\varphi(x)] \tag{9}$$

where x denotes the distance from the planar surface, and $\varphi \equiv \beta Ze\psi$ is the reduced local electrical potential. With boundary conditions $\psi(x) = \psi_s$ at $x = 0$ and $\psi'(x) = 0$ at $x = \infty$, the one-dimensional Poisson equation can be solved analytically[56]

$$\frac{\tanh[\varphi(x)/4]}{\tanh(\varphi_s/4)} = e^{-\kappa x} \tag{10}$$

where $\kappa \equiv \sqrt{\sum_i \rho_i^0 Z_i^2 e^2/\epsilon k_B T}$ is known as the Debye screening parameter. Assuming that the surface electrical potential is the same as the electrode potential, $\psi_s \approx \psi_m$, we may connect the surface charge density with the surface electrical potential through Gauss's law[56]

$$Q = -\epsilon \left.\frac{\partial\psi(x)}{\partial x}\right|_{x=0} = \sqrt{8\epsilon k_B T \rho_0}\ \sinh(\varphi_s/2) \tag{11}$$

Eq 11 is often referred to as the Grahame equation.

The GC theory predicts that the differential capacitance of the double layer is given by[56]

$$C_d^{GC} = \frac{\partial Q}{\partial \psi_s} = \epsilon\kappa \cosh(\varphi_s/2) \tag{12}$$

Eq 12 is valid only at small surface potential, i.e., $\psi_s \sim k_B T/e$. As the capacitance increases exponentially with the reduced surface potential φ_s, the capacitance versus the surface potential displays a U-shape curve with a minimum capacitance, $C_d^{min} = \epsilon\kappa$, taking place when the surface potential is zero, $\psi_s = 0$. The quantity $C_d = \epsilon\kappa$ is commonly known as the Debye capacitance, which can be derived from the linearized PB equation as used in the Debye−Hückel model for dilute electrolyte solutions.

Noting that $\tanh y = (e^{2y} - 1)/(e^{2y} + 1)$, we can rearrange eq 10 and find an analytical expression for the reduced local electric potential

$$\varphi(x) = 2 \ln\left(\frac{1 + \xi_s e^{-\kappa x}}{1 - \xi_s e^{-\kappa x}}\right) \tag{13}$$

https://doi.org/10.1021/acs.chemrev.2c00097
Chem. Rev. XXXX, XXX, XXX−XXX

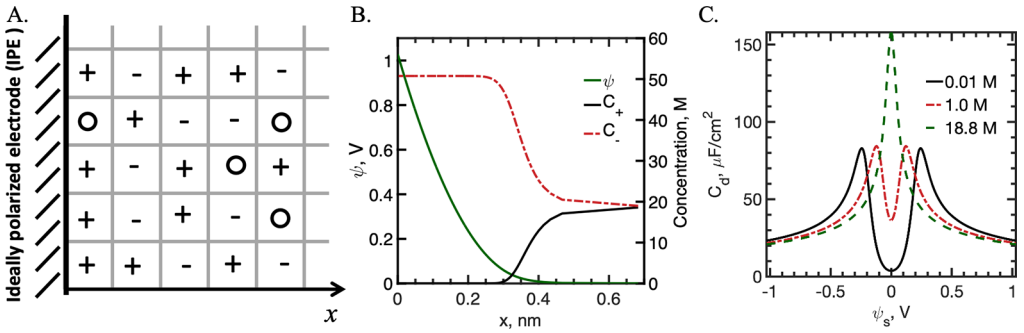

Figure 3. EDL as a lattice gas. A. Ions (±) and solvent molecules (○) randomly placed on a cubic lattice near a planar electrode (IPE). B. The local electrical potential $\psi(x)$ and ion concentrations predicted by the mean-field lattice-gas model with the reduced surface potential $\varphi_s = 40$ and bulk packing fraction $\eta_0 \approx 0.74$, the close packing limit of uniform spheres. C. Differential capacitance versus the surface potential predicted by the lattice model. The "bell-shaped" curve at the highest concentration (18.8 M) corresponds to the close packing limit, and a "camel-shaped" curve appears at low bulk concentrations. The conversion to experimental units was made by assuming $T = 298.15$ K, 0.5 nm for ion diameters, and 2 for the dielectric constant of the electrolyte.

where $\xi_s = \tanh(\varphi_s/4)$. Accordingly, the PB equation predicts the ionic density profiles

$$\rho_+(x)/\rho^0 = \left[\frac{1 - \xi_s e^{-\kappa x}}{1 + \xi_s e^{-\kappa x}}\right]^2$$

$$\rho_-(x)/\rho^0 = \left[\frac{1 + \xi_s e^{-\kappa x}}{1 - \xi_s e^{-\kappa x}}\right]^2 \quad (14)$$

As shown in Figure 2B, eq 14 predicts a monotonic variation of the local ion density with the position, in good agreement with MC simulation for monovalent ions at low to moderate concentrations.

If the EDL is represented by a hard wall in contact with monovalent charged hard spheres in a uniform dielectric medium, the GC theory yields the local electrical potential and ion distributions that agree reasonably well with simulation data even at moderate ion concentrations. For example, Figure 2B compares the theoretical predictions with Monte Carlo (MC) simulation. The ionic density profiles predicted by the GC theory are near quantitative when the ion concentration in the bulk is as large as 2 M. However, the local electrical potential shows more significant discrepancy, suggesting that the good agreement for the ionic density profiles is in part due to the cancellation of errors, i.e., the local electrical potential overestimated by the mean-field approximation is partially compensated by the ionic excluded volume or size effects. It should be noted that the difference between the GC predictions and simulation results is dramatic if the system contains multivalent counterions.

The PB equation neglects the molecular nature of ions and solvent. Besides, it accounts for only the Coulomb interactions in a uniform dielectric medium at the mean-field level. Because the dimensionality of the EDL is mostly microscopic, the properties predicted by the PB equation may deviate significantly from those corresponding to a realistic electrochemical interface.[61] Over the years, a plethora of modifications have been proposed to improve the PB equation by considering dielectric inhomogeneity and/or incorporating electrostatic correlations.[62,63] Because many theoretical efforts were devoted to point-charge models, they have limited implications to concentrated electrolytes commonly used for capacitive energy storage and, thus, will not be discussed in this review. Conventionally, the solvent effects and specific ion adsorptions are accounted for by the Stern model, which is convenient for practical applications but provides little insights on microscopic details. Even for a near ideal electrode in a dilute electrolyte solution (e.g., Ag (111) in contact with the NaF solution), the GCS theory yields a reasonable EDL capacitance only if the Stern-layer dielectric constant is assumed to vary with the local electric field.[14] A recent *ab initio* MD simulation indicates that the specific adsorption of water molecules at the Pt (111) surface may lead to a negative capacitive response (Figure 2F).[37] A combination of the theoretical analysis and experimental data shows that, in addition to the local solvent effects, partial charge transfer must be accounted for in order to describe specific ion adsorption (Figure 2D).[14] While the PB equation may be empirically modified to include water reorganization and nonelectrostatic ion-surface interactions,[64] a first-principles approach is required to describe the chemisorptions of ionic species or solvent molecules.[65]

2.2. Lattice-Gas Model

For concentrated electrolytes and ionic liquids, the excluded volume of chemical species plays an important role in determining the ion distributions and EDL capacitance. The steric or size effects can be incorporated into the PB equation by using either lattice or particle-based models.[66−68] The lattice model for the EDL was first proposed by Bikerman;[69] and the early literature has been summarized in detail by Bazant et al.[70] If the electrolyte solution is represented by the primitive model, i.e., ions are charged hard spheres and the solvent is a dielectric continuum, liquid-state theories and simulation methods have been well established to account for both electrostatic correlations and the geometric constraints of ion packing in a confined space.[71,72] Simpler models are also frequently used to account for the size effects because they are computationally more efficient and analytically more tractable.[73] In particular, the lattice-gas model for ionic liquids proposed by Kornyshev,[74] and independently by Kilic, Bazant, and Ajdari for concentrated electrolytes at about the same time,[75] represents one of the most popular methods for describing the nonclassical behavior of EDL capacitance.

Figure 3A shows the lattice representation of the EDL near an ideal polarizable electrode (IPE), i.e., a perfect metal in contact with an electrolyte without charge transfer at the interface. According to the mean-field approximation, the Helmholtz energy includes an electrostatic component the same as that given by the PB equation and an entropic contribution to

https://doi.org/10.1021/acs.chemrev.2c00097
Chem. Rev. XXXX, XXX, XXX−XXX

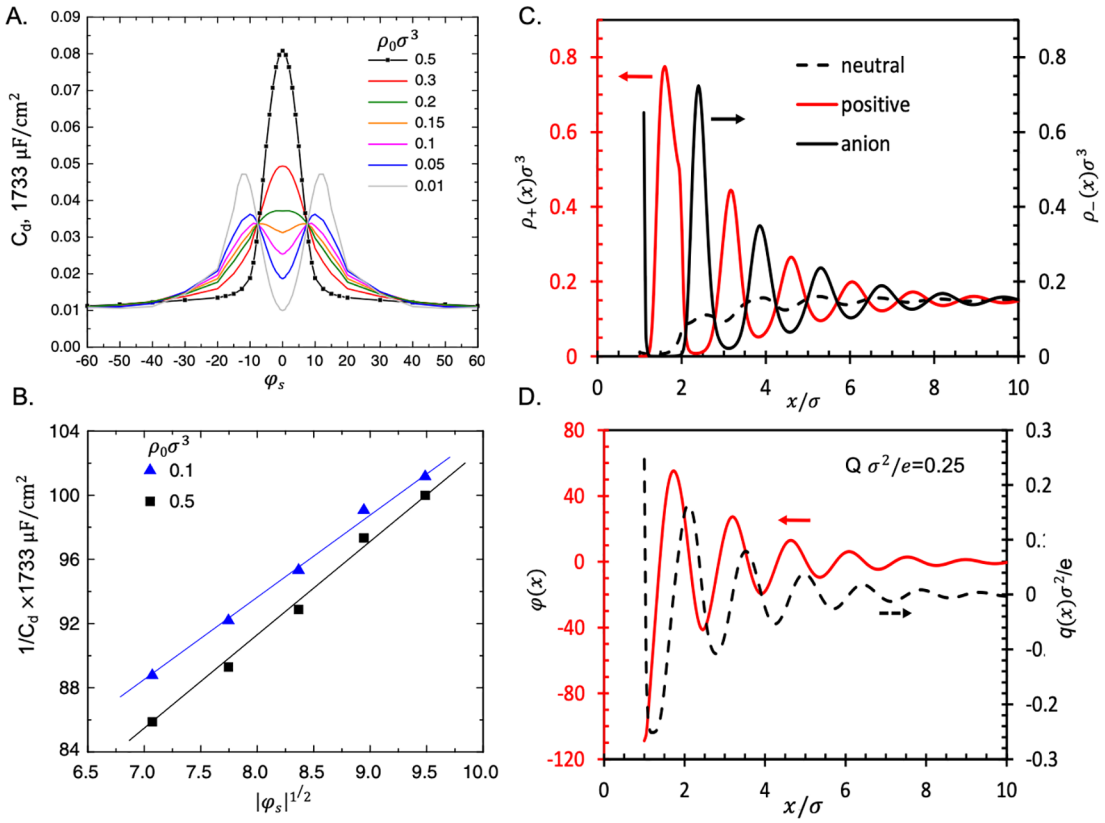

Figure 4. EDL structure and capacitance predicted by the primitive model of electrolytes. A. Differential capacitance versus the reduced surface potential for an organic electrolyte at different bulk concentrations, $\rho_0\sigma^3$, where $\sigma = 0.6$ nm is the ion diameter. B. The inverse-square-root decay of the differential capacitance at high surface voltage. C. The reduced ion densities of cations and anions for an ionic liquid near a surface of charge density $Q\sigma^2/e = 0.25$. Here, each cation was described as a dimer of tangentially connected positive and neutral spheres. D. The reduced local electrical potential, $\varphi(x)$, and integrated charge density, $q(x)$, corresponding to panel C. (A and B) Reproduced with permission from ref 80. Copyright 2011 Elsevier. (C and D) Reproduced with permission from ref 79. Copyright 2016 Royal Society of Chemistry.

account for the random arrangement of chemical species on the lattice[74−76]

$$F = \int \mathrm{d}\mathbf{r}[f_c(\psi, q) + f_{\mathrm{lattice}}] \tag{15}$$

where $f_c(\psi, q)$ is given by eq 4, and f_{lattice} corresponds to that for an ideal mixture of ionic species and solvent molecules

$$f_{\mathrm{lattice}} = \frac{k_B T}{a^3}\left\{\sum_i \rho_i(\mathbf{r})a^3 \ln[\rho_i(\mathbf{r})a^3] + [1 - \eta(\mathbf{r})]\ln[1 - \eta(\mathbf{r})]\right\} \tag{16}$$

In eq 16, a represents the lattice size, $\eta(\mathbf{r}) \equiv \sum_i \rho_i(\mathbf{r})a^3$ corresponds to the fraction of the lattice sites occupied by ionic species (viz., packing fraction), and the last term on the right side arises from the incompressibility assumption as typically adopted in the mean-field theories of polymer systems.

Eq 15 provides a starting point to derive ion distributions and electrical potential in the double layer. Similar to the point-charge model discussed above, minimization of the Helmholtz energy with respect to the electrical potential leads to the Poisson equation, eq 7. Meanwhile, the functional derivative of the Helmholtz energy with respect to the ionic density profiles gives

$$\rho_i(\mathbf{r}) = \frac{\rho_i^0 \exp[-\beta Z_i e\psi(\mathbf{r})]}{1 + \eta_0\{\cosh[-\beta Ze\psi(\mathbf{r})] - 1\}} \tag{17}$$

where $\eta_0 = \sum_i \rho_i^0 a^3$, and the denominator may be understood in terms of the local incompressibility of the electrolyte solution.[77] Eq 17 was first derived by Bikerman.[69] It is sometimes referred to as the Fermi distribution because the mathematical form is similar to that for describing the energy states of Fermions.[74] For a dilute electrolyte in the bulk ($\eta_0 \to 0$) or in the limit of weak surface electrical potential ($\beta Ze\psi(\mathbf{r}) \to 0$), eq 17 reduces to the original Boltzmann distribution, eq 8.

For a symmetric electrolyte near a planar electrode, all variables change only in the direction perpendicular to the surface. Accordingly, the lattice model predicts that the ionic density profiles are given by

$$\rho_\pm(x) = \frac{\rho_0 \exp[-\beta Z_\pm e\psi(x)]}{1 - \eta_0 + \eta_0 \cosh[\beta Ze\psi(x)]} \tag{18}$$

Similar to that in the GC theory, the local electrical potential can be expressed as an implicit function of κx[74]

$$\kappa x = \mathrm{sgn}(\varphi_s)\sqrt{\eta_0/2}\int_{\varphi}^{\varphi_s} \frac{d\varphi}{\sqrt{\ln[1 + 2\eta_0 \sinh^2(\varphi/2)]}} \tag{19}$$

A modified Grahame equation can also be derived by applying the Gauss law at $x = 0$

$$Q = \mathrm{sgn}(\varphi_s)\frac{2Ze\rho_0}{\kappa}\sqrt{\frac{2}{\eta_0}\ln[1 + 2\eta_0 \sinh^2(\varphi_s/2)]} \tag{20}$$

https://doi.org/10.1021/acs.chemrev.2c00097
Chem. Rev. XXXX, XXX, XXX−XXX

where $\eta_0 = 2\rho_0 a^3$ corresponds to the packing fraction of the ionic species in the bulk solution. As expected, the original Grahame equation is recovered at low surface potential ($\varphi_s \ll 1$). According to eq 20, the differential capacitance is given by

$$C_d \equiv \frac{\partial Q}{\partial \psi_s} = \mathrm{sgn}(\varphi_s)\frac{\epsilon\kappa \sinh(\varphi_s)}{1 + 2\eta_0 \sinh^2(\varphi_s/2)}\sqrt{\frac{\eta_0}{2\ln[1 + 2\eta_0 \sinh^2(\varphi_s/2)]}} \tag{21}$$

Eq 21 was first derived by Freise[78] based on Bikerman's model. As $\eta_0 \to 0$, it reduces to that predicted by the GC theory, eq 12. When the lattice is fully occupied by ionic species, $\eta_0 = 1$, eq 21 predicts a maximum capacitance at a neutral surface identical to the Debye capacitance, $C_d = \epsilon\kappa$.

Figure 3B and C presents the EDL structure and capacitance predicted by the lattice model. Like that predicted by the GC theory, the local electrical potential decays monotonically away from the charged surface. However, the assumption of incompressibility leads to the saturation of ion density near the electrode surface. The so-called steric effect can also be captured by the addition of a "condensed" region before the diffuse layer.[75] Different from the U-shape predicted by the GC theory, the differential capacitance shows "bell" and "camel" shapes in response to the variation of the electrode voltage at high and low ion concentrations, respectively. A similar relation between the capacitance and surface potential, including its inverse-square-root decay, $C_d \sim \psi_s^{-0.5}$, was confirmed by subsequent theoretical and simulation studies.[79,80]

The saturation effect on the local ion concentrations predicted by the lattice model is not supported by numerical results from particle-based models or experimental observations.[81] As shown in Figure 4, strong electrostatic correlation and excluded-volume effects may lead to oscillatory ionic density profiles and local electrical potential that are not captured by the mean-field approximation. To remediate this caveat, Bazant, Storey, and Kornyshev (BSK) introduced a modified electrostatic energy using the "Cahn−Hilliard-like" expansion[82,83]

$$f_{\mathrm{BSK}}(\psi, q) = q\psi - \frac{\epsilon}{2}[|\nabla\psi|^2 + (l_c\nabla^2\psi)^2] \tag{22}$$

where $l_c > 0$ is a phenomenological parameter related to nonlinear dielectric response. The parameter l_c has the units of length with a numerical value comparable to the ion size.[82] The nonlinear electrostatic energy may be reformulated in terms of a screened Coulomb potential accounting for both electrostatic and short-ranged correlations.[84−86]

The lattice-gas model can be generalized for electrolytes with asymmetric ionic species by using the Flory−Huggins-type equations.[87,88] Zhang and Huang compared several ways to account for the size asymmetry and discussed their physical significance in terms of the lattice configuration number, the dimensionless excess chemical potential, and the differential capacitance.[89] Alternative modifications of electrostatic energy have also been proposed by weighing the local charge density,[90] by including ionic clusters[91] or polarization effects,[92] and by treating ion pairs as neutral particles when the distance is below a threshold but point charges otherwise.[93] The modified PB methods are able to capture overscreening effects for systems with strong electrostatic interactions. However, they predict the ionic density profiles and local electrostatic potential distinctively different from those generated from particle-based models.[94] In comparison with alternative approaches, one major advantage of mean-field methods lies in their simplicity and efficiency in capturing the generic features of capacitive energy storage and in describing various phase transitions in ionic systems including the voltage-induced charge separation, solvent-demixing, and in-plane structural ordering as to be discussed in the following (Section 3.7). Another advantage of mean-field methods is that they allow for the development of analytical solutions and physical insights that might be difficult to attain through molecular simulations or complicated theories.

2.3. Classical Density Functional Theory

Classical density functional theory (cDFT) represents a generic methodology in statistical mechanics naturally applicable to open systems (viz., grand-canonical ensemble).[95,96] Like the Kohn−Sham DFT−its electronic counterpart, cDFT, is mathematically rigorous within the framework of a specific thermodynamic model. However, the free-energy functional is typically formulated with approximations, ranging from simplistic mean-field assumptions as that used in deriving the PB equation and different flavors of local and weighted density approximations (LDA and WDA), to much more sophisticated methods such as the fundamental measure theory (FMT) and the universality of bridge functional.[97−100] In combination with various transport equations, cDFT can be directly extended to describe time-dependent phenomena such as charging dynamics and ion transport in confined geometry.[101]

As an alternative to the PB equation, cDFT has been used to describe the EDL structure and thermodynamic properties of confined ionic systems for decades.[23,24] While the free-energy functional can be formulated for any thermodynamic system, in principle, existing applications of cDFT to electrochemical systems are mostly based on the primitive model (PM) or the restricted primitive model (RPM) of electrolytes where ions are represented by charged hard spheres of equal size and valence. In comparison with the PB equation, PM/RPM-cDFT introduces two additional terms into the free-energy functional (eq 2)

$$F = \int \mathrm{d}\mathbf{r}[f_{is} + f_c(\psi, q) + f_{hs} + f_{corr}] \tag{23}$$

where f_{hs} accounts for the excluded-volume effects due to the particle size, and f_{corr} arises from electrostatic correlations. Highly accurate functionals are available for both f_{hs} and f_{corr}.[24,102] To achieve quantitative performance, the excluded-volume effects are often described by the modified fundamental measure theory (MFMT)[103−105]

$$\beta f_{hs} = -n_0\ln(1 - n_3) + \frac{n_1 n_2 - \mathbf{n_{v1}}\cdot\mathbf{n_{v2}}}{1 - n_3} + (n_2^3 - 3n_2\mathbf{n_{v2}}\cdot\mathbf{n_{v2}})\frac{n_3 + (1 - n_3)^2\ln(1 - n_3)}{36\pi n_3^2(1 - n_3)^2} \tag{24}$$

where the weighted densities are generated according to

$$n_\alpha(\mathbf{r}) = \sum_i \int \mathrm{d}\mathbf{r}'\rho_i(\mathbf{r}')\omega_i^{(\alpha)}(\mathbf{r} - \mathbf{r}') \tag{25}$$

with the weight functions given by

$$\omega_i^{(0)}(\mathbf{r}) = \frac{\delta(R_i - r)}{4\pi R_i^2},\ \omega_i^{(1)}(\mathbf{r}) = \frac{\delta(R_i - r)}{4\pi R_i},\ \omega_i^{(2)}(\mathbf{r}) = \delta(R_i - r),$$
$$\omega_i^{(3)}(\mathbf{r}) = \Theta(R_i - r),\ \omega_i^{(\mathbf{v1})}(\mathbf{r}) = \frac{\mathbf{r}}{r}\frac{\delta(R_i - r)}{4\pi R_i},\ \omega_i^{(\mathbf{v2})}(\mathbf{r}) = \frac{\mathbf{r}}{r}\delta(R_i - r) \tag{26}$$

Unlike a typical weighted density approximation (WDA), which employs empirical or heuristic weight functions, FMT employs

https://doi.org/10.1021/acs.chemrev.2c00097
Chem. Rev. XXXX, XXX, XXX−XXX

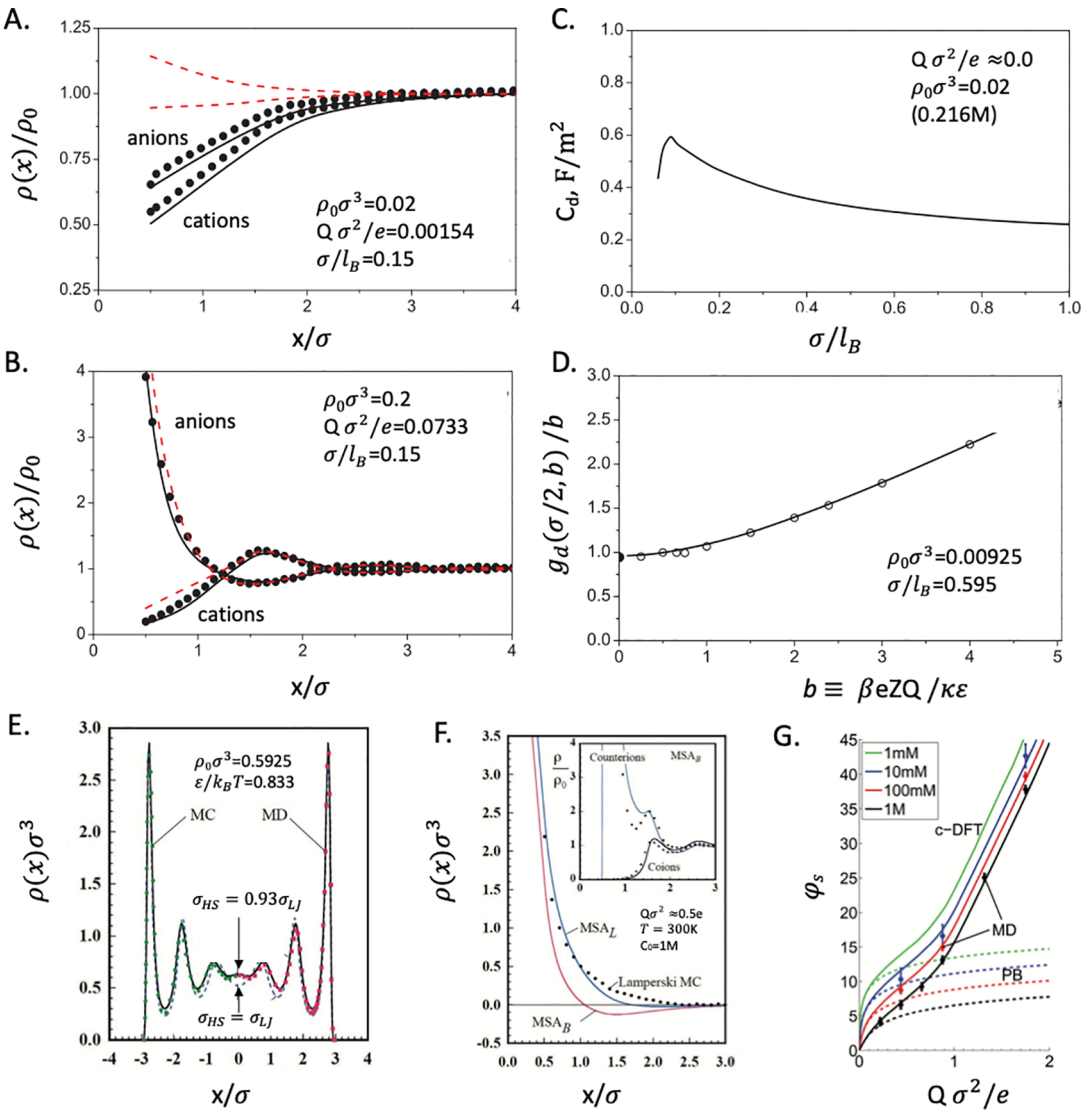

Figure 5. EDL at a planar surface predicted by the primitive model of electrolytes. A and B. Comparison of cDFT (lines) and MC (points) for the ionic density profiles. C. Variation of the EDL capacitance with the reduced temperature (σ/l_B). D. Comparison of cDFT (line) and MC (points) for the difference between the contact densities of cations and anions. E. The local density of a Lennard-Jones (LJ) fluid in a slit pore calculated from MC (green circles) and MD (red squares) in comparison with cDFT (solid and dashed lines) with two different choices of the hard-sphere diameter (σ_{HS}) relative to the LJ diameter (σ_{LJ}). F. Ionic density profiles predicted by different versions of cDFT. G. Comparison of the surface electrical potential predicted by three EDL models. (A–D) Adapted with permission from ref 112. Copyright 2014 Taylor & Francis. (E–G) Adapted from ref 117. Copyright 2012 American Chemical Society.

the Dirac-delta function $\delta(R_i - r)$ and Heaviside step function $\Theta(R_i - r)$ to describe the geometric characteristics of the Mayer function for the interaction between spherical particles of radius R_i. Eq 24 can be derived in conjunction with the scaled-particle theory or the Boublik-Mansoori-Carnahan–Starling-Leland (BMCSL) equation of state for hard-sphere mixtures.[104]

The free energy due to electrostatic correlations is typically formulated in terms of a quadratic functional expansion

$$f_{corr} = f^0_{corr} + \sum_i \Delta\rho_i(\mathbf{r})\Delta\mu_i^{(0)} - \frac{k_BT}{2}\sum_i\sum_j \int d\mathbf{r}\Delta\rho_i(\mathbf{r})\Delta\rho_j(\mathbf{r})\Delta c_{i,j}^{(0)}(|\mathbf{r}-\mathbf{r}'|) \quad (27)$$

where f^0_{corr} corresponds to the correlation free energy of a bulk electrolyte of uniform ion density $\rho_i^{(0)}$, $\Delta\rho_i(\mathbf{r}) = \rho_i(\mathbf{r}) - \rho_i^{(0)}$, and $\Delta\mu_i^{(0)}$ and $\Delta c_{i,j}^{(0)}(|\mathbf{r}-\mathbf{r}'|)$ are the nonmean-field contributions to the ionic chemical potential and the direct correlation function for the bulk system. The reference system may be defined either in terms of the ionic chemical potentials (MSA$_B$) or by weighted local density approximations (MSA$_L$).[106,107] In both cases, the nonmean-field contributions are connected with the mean spherical approximation (MSA) for bulk electrolytes.[108] In addition to the quadratic approximation, a nonmean-field free energy has also been derived from the functionalized MSA (fMSA).[109,110]

With the electrolytes represented by the primitive model and the electrode treated as a hard wall, the ion densities near the surface satisfy the contact-value theorem[111]

$$k_BT\sum_i \rho_i(\sigma_i/2) = \Pi_0 + \frac{\epsilon}{2}|\mathbf{E}(0)|^2 \quad (28)$$

where Π_0 stands for the osmotic pressure of the electrolyte in the bulk solution, and $\mathbf{E}(0)$ is the electric field at the electrode

https://doi.org/10.1021/acs.chemrev.2c00097
Chem. Rev. XXXX, XXX, XXX–XXX

surface. The latter is related to the surface charge density by $|\mathbf{E}(0)| = Q/\epsilon$. If there are only two types of charged hard spheres with the same diameter σ and valence Z, the surface compositions of ionic species satisfy the following contact-value relations[112]

$$g_s(\sigma/2) \equiv [\rho_+(\sigma/2) + \rho_-(\sigma/2)]/2\rho_0 = z_0 + b^2/2$$
$$g_d(\sigma/2) \equiv [\rho_+(\sigma/2) - \rho_-(\sigma/2)]/2\rho_0 \approx z_0 b \quad (29)$$

where $z_0 \equiv \Pi_0/(2\rho_0 k_B T)$ and $b \equiv \beta e Z Q/(\epsilon\kappa)$. The first contact-value relation is equivalent to eq 28, and the second contact-value relation was proposed by Henderson and Boda based on the semiempirical correlation of simulation results.[113] The contact-corrected density functional theory (ccDFT) leverages the statistical-mechanical sum rule, eq 28, to further improve the numerical performance of cDFT calculations.[114,115]

Without specific chemical effects, the thermodynamic properties of ionic systems are dominated by electrostatic interactions and the excluded volume of individual particles. As a result, the primitive model has been a popular choice in the statistical-mechanical studies of electrolyte solutions. Indeed, it has been long recognized that the primitive model is able to describe both thermodynamic and transport properties of bulk electrolyte solutions in quantitative agreement with experimental results.[116] Unlike the PB equation, PM/RPM-cDFT takes into account both particle packing and correlation effects and, thus, is able to capture nonintuitive electrostatic phenomena such as oscillatory ionic distributions and charge inversion (see Figure 4). Understandably, the quantitative performance depends on the formulation of the free-energy functional and specific thermodynamic conditions.

Figure 5 compares several versions of cDFT (MSA_B, MSA_L, and ccDFT) with simulation results for the EDL capacitance, the ion distributions near different planar surfaces, and the dependence of the surface potential on the surface charge density. While quantitative agreement with simulation results can be reached by a judicious selection of the free-energy functional, their discrepancies are significant, in particular at conditions when the electrostatic correlation effects are important (e.g., ion distributions near a neutral surface). Although the second contact-value relation is not exact, Figure 5D indicates that it predicts the difference between the concentrations of cations and anions at contact in excellent agreement with ccDFT predictions. Because of their simplicity, the contact-value relations are particularly useful for determining the surface composition of ionic species on the basis of the surface charge density. Interestingly, ccDFT predicts a nonmonotonic dependence of the differential capacitance in response to temperature changes (Figure 5C). A similar trend was observed in both MC simulation and experiments but not predicted by conventional EDL models. The nonmonotonic temperature dependence of the double-layer capacitance can be reproduced only when electrostatic correlations and ion distributions in the vicinity of the charged surface are adequately described.[118]

It should be noted that cDFT is useful not only for hard-sphere systems. The theoretical procedure is equally applicable to more realistic models of EDL including those containing organic electrolytes and ionic liquids with complicated molecular structures.[22,117,119,120] For example, Figure 5E–G compares simulation data with cDFT and the PB equation for a model EDL consisting of charged Lennard-Jones (LJ) spheres. While cDFT and simulation results show excellent agreement, the PB equation does not yield quantitative performance at high salt concentrations. Neither does it predict accurate ion distributions near a strongly charged surface. For systems containing molecular/polyatomic ionic species, a reliable free-energy functional can also be developed for both coarse-grained and atomistic models.[25,121] One major hurdle in applications of these more sophisticated cDFT methods is numerical complexity. Although cDFT calculations are much faster than MD simulations, typically by several orders of magnitude, the lack of reliable software infrastructure often impedes their broad applications to multidimensional systems. In light of recent developments of GPU algorithms that allow for massive parallel computation,[122] we expect more applications of cDFT to nonprimitive models of ionic systems in the future, especially under conditions when molecular details are needed in order to have a comprehensive description of electrochemical phenomena.

2.4. Grand-Canonical Methods

As early as 1920, Frumkin pointed out that the assumption of a perfect layer of charge at the electrode surface did not explain certain experimental facts about the EDL.[123] To remediate the discrepancies between theoretical predictions and experiments, Rice proposed an EDL model in 1928 with an explicit consideration of the electronic structure in a metallic electrode and its response to ion distributions.[26] Regrettably, the nonideal behavior of the electrode was largely ignored in the following decades until the early 1980s when the electronic properties of a metallic surface in an electrolyte became directly measurable through experimental techniques.[29,124] Theoretical investigations of the EDL electronic structure have been rejuvenated in recent years due to its importance in understanding electrode–electrolyte interactions as well as electrochemical reactions.[30,32,125−127] Even with a relatively simple description of the electrode nonideality, the extended EDL model provides insights into the capacitance as well as mechanical responses of the double layer.[128] Besides, the electronic structure of the electrode is directly responsible for the appearance of quantum capacitance,[129] pseudocapacitance,[2] dielectric screening of ion–ion interactions within the diffuse layer,[130] and the wetting transitions of ionic liquids at metallic surfaces.[46]

With the assumption that there is no electron transfer at the electrode–electrolyte interface (viz., IPE) and that the positions of electrode atoms are frozen, the EDL can be represented by an open system of electrons, ionic species, and solvent molecules as sketched in Figure 6A. Given absolute temperature T and total volume V, the grand potential Ω is a functional of the electron density $\rho_e(\mathbf{r})$ and the density profiles of both ionic species $\rho_i(\mathbf{x_i})$ and solvent molecules $\rho_s(\mathbf{x_s})$, where multidimensional vectors $\mathbf{x_s} \equiv \{\mathbf{r_1}, \mathbf{r_2}, ..., \mathbf{r_{n_s}}\}$ and $\mathbf{x_i} \equiv \{\mathbf{r_1}, \mathbf{r_2}, ..., \mathbf{r_{n_i}}\}$ represent the atomic configurations of a solvent molecule and ion i with n_s and n_i being the number of atoms or interactions sites, respectively. At equilibrium, the grand potential is minimized with respect to these density profiles

$$\delta\Omega[\rho_e(\mathbf{r}), \rho_s(\mathbf{x_s}), \rho_i(\mathbf{x_i})] = 0 \quad (30)$$

With an analytical expression for $\Omega[\rho_e(\mathbf{r}), \rho_s(\mathbf{x_s}), \rho_i(\mathbf{x_i})]$, we can, in principle, predict the density profiles of electrons and ionic species by solving eq 30 and, subsequently, determine the electrochemical properties of the system.

Formally, the grand potential can be written in terms of the electrostatic energy due to interactions among all chemical

https://doi.org/10.1021/acs.chemrev.2c00097
Chem. Rev. XXXX, XXX, XXX−XXX

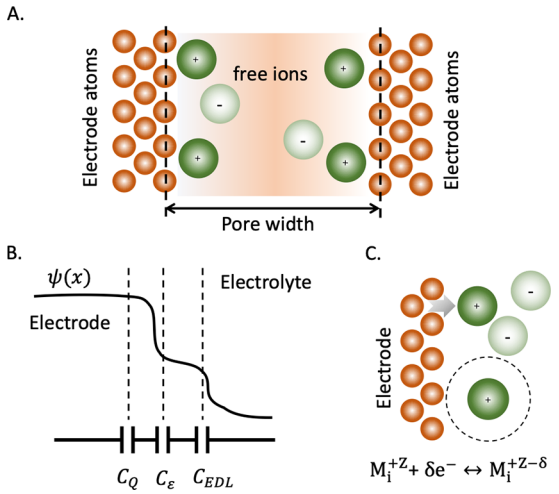

Figure 6. A. Schematic of an electrolyte solution in a porous electrode defined as an open system, i.e., a system with fixed chemical potentials of electrons (μ_e), solvent molecules (μ_s), and ionic species ($\mu_\pm$). B. Local electrical potential and various contributions to the total capacitance: quantum (C_Q), dielectric (C_ϵ), and diffuse layer capacitance (C_{EDL}). C. Charge transfer between the electrode atoms (M_i) and adsorbed ions represented by faradaic reactions.

species, the intrinsic Helmholtz energies of electrons and the electrolyte, and one-body external potentials for electrons and all other chemical species in the system

$$\Omega = \int d\mathbf{r}\left[q(\mathbf{r})\psi(\mathbf{r}) - \frac{\epsilon_0}{2}|\nabla\psi(\mathbf{r})|^2\right] - \int d\mathbf{r}\rho_e(\mathbf{r})[\mu_e - v_e^{ext}(\mathbf{r})] - \sum_\alpha \int d\mathbf{x}_\alpha \rho_\alpha(\mathbf{x}_\alpha)[\mu_\alpha - v_\alpha^{ext}(\mathbf{x}_\alpha)] + \mathcal{F}_e[\rho_e(\mathbf{r})] + \mathcal{F}_a[\rho_s(\mathbf{x}_s), \rho_i(\mathbf{x}_i)] \quad (31)$$

where subscripts e and $\alpha = (s \text{ or } i)$ stand for electrons and solvent molecules or ions, respectively, ϵ_0 is the permittivity of the free space, $\psi(\mathbf{r})$ represents the local electric potential, and $v_e^{ext}(\mathbf{r})$ and $v_\alpha^{ext}(\mathbf{x}_\alpha)$ are the one-body potentials excluding the direct Coulomb energy which is included in the local electrical potential. $\mathcal{F}_e[\rho_e(\mathbf{r})]$ and $\mathcal{F}_a[\{\rho_\alpha(\mathbf{x}_\alpha)\}]$ correspond to the intrinsic Helmholtz energy functionals of electrons and the inhomogeneous electrolyte.

The first line on the right side of eq 31 is identical to that corresponding to the venerable PB equation, eq 4, except that here, the permittivity is referred to that corresponding to the free space and that the local charge density includes contributions from the electrode atoms as well as all chemical species from the electrolyte solution. With the electrode represented by classical atomic particles (viz., nuclei or atomic cores if pseudopotentials are used for the electrode atoms) plus free electrons (viz., any electrons not included in the classical representation of electrode atoms), and the electrolyte represented by a semiempirical force field, the local charge density can be written as

$$q(\mathbf{r}) = -e\rho_e(\mathbf{r}) + \sum_m q_m \delta(\mathbf{r} - \mathbf{r}_m) + \sum_\alpha \sum_{\alpha_k} q_{\alpha_k}\rho_{\alpha_k}(\mathbf{r}) \quad (32)$$

where $\mathbf{r}_m$ and q_m stand for, respectively, the position and electrical charge of a classical particle representing an electrode atom m. The Dirac-δ function $\delta(\mathbf{r} - \mathbf{r}_m)$ arises from fixing the positions of electrode atoms for the formulation of the grand potential. The last term on the right side of eq 32 accounts for the atomic charges of solvent and ionic species, with q_{α_k} and $\rho_{\alpha_k}(\mathbf{r})$ standing for the electrical charge and local density of atom k from species α. Overall, the system satisfies the charge neutrality

$$\int d\mathbf{r} q(\mathbf{r}) = 0 \quad (33)$$

Similar to that in a classical EDL model, the local electrostatic potential and the local charge density are related to each other through the Poisson equation

$$\nabla^2\psi(\mathbf{r}) = -\frac{q(\mathbf{r})}{\epsilon_0} \quad (34)$$

The generic procedure outlined above is applicable to all EDL systems for capacitive energy storage without surface charge transfer. Theoretically, the capacitance can be calculated from

$$C = e^2\frac{\partial^2\Omega}{\partial\mu_e^2} \quad (35)$$

Eq 35 is formally exact. For practical applications, the grand potential must be formulated in terms of the chemical potentials of electrons from the electrode and ionic species in the bulk electrolyte. The electron chemical potential μ_e affects energy storage not only through the surface potential of the electrode but also through variations in the electronic structure and the density of state. The latter contributions are responsible for quantum capacitance (C_Q) and dielectric capacitance (C_ϵ), respectively, as shown schematically in Figure 6B and to be discussed in Section 3.8. If charge transfer takes place at the electrode−electrolyte interface, additional contributions must be considered to account for the electronic structure of the adsorbed species and surface reactions (Figure 6C).

As in cDFT calculations, difficulties in application of the grand-canonical approach are mostly affiliated with the formulation of $\mathcal{F}_e[\rho_e(\mathbf{r})]$ and $\mathcal{F}_a[\{\rho_\alpha(\mathbf{x}_\alpha)\}]$ and numerical details in solving eq 30. For a hybrid system with quantum and classical components, an additional challenge emerges in the development of semiempirical models to describe electron-electrolyte interactions shown as $v_e^{ext}(\mathbf{r})$ and $v_\alpha^{ext}(\mathbf{x}_\alpha)$ in eq 31.[131] While earlier attempts to describe the electronic structure on the electrode side of the double layer adopted the Thomas-Fermi theory or so-called jellium model (viz., the uniform electron gas),[29] recent developments are mostly based on the Kohn−Sham (KS)-DFT in conjunction with various classical EDL models for ion distributions. One of the most successful approaches thus far was established by integration of the KS-DFT with the three-dimensional reference interaction site method (3D-RISM).[132] The original concepts were developed by Kovalenko and Hirata to predict solvation free energies whereby solute−solvent interactions are represented by the Coulomb potential and the LJ model.[133] Other forms of the solute−solvent interactions have also been explored.[134] The effective one-body potential in the KS equation (viz., the solvent effects) is determined self-consistently from the electrode solvation free energy by using the RISM equation. Because the nonelectrostatic part of the solute−solvent interactions is represented by a semiempirical model, the accuracy of the hybrid method depends on the selection of force-field parameters. In extension of the solvation model to EDL, Nishihara and Otani developed an effective screening medium method (ESM) and Green's function techniques to describe

https://doi.org/10.1021/acs.chemrev.2c00097
Chem. Rev. XXXX, XXX, XXX−XXX

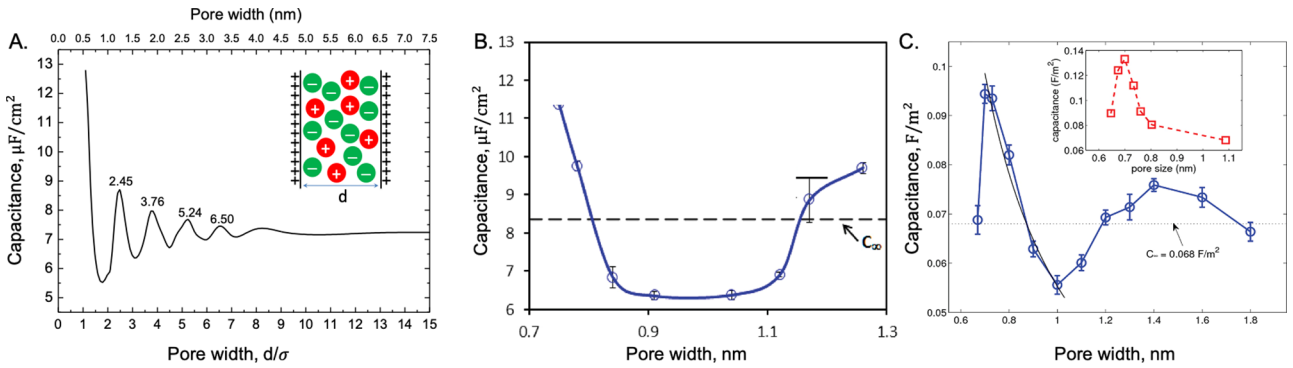

Figure 7. Dependence of capacitance on the pore width for an ionic liquid in a slit pore. A. Integral capacitance at 1.5 V predicted by cDFT based on the restricted primitive model mimicking EMIM-TFSI in carbon pores. B. Variation of the integral capacitance with the slit pore width according to MD simulation for a coarse-grained model of ionic liquids. Here, C_∞ denotes the capacitance of an open planar electrode. C. Integral capacitance from an all-atom MD simulation for EMIM-TFSI in carbon slit pores at 1.41 V. The inset shows the corresponding experimental results. Reproduced from (A) refs 155, (B) 156, and (C) 157. Copyright 2011 American Chemical Society.

electrified interfaces with open boundary conditions.[135] Another popular approach to account for electron−ion interactions explicitly is the joint density-functional theory (Joint-DFT).[31,136,137] In principle, Joint-DFT can be formulated by applying the Hohenberg−Kohn theorem to open systems of electrons and classical particles as shown in eq 31. However, further developments are needed to describe the quantum-classical interactions. Existing applications of Joint-DFT are mostly based on semiempirical solvation models that employ the PB-type equations. Recently, a number of grand-canonical or multicomponent DFT methods have been reported by combining KS-DFT with various forms of the PB equation.[138−142] A hybrid DFT has also been proposed that integrates the orbital-free electronic DFT and the fundamental measure theory within the framework of the statistical field theory (SFT).[143,144]

3. CAPACITIVE ENERGY STORAGE

In this section, we discuss theoretical predictions of EDL capacitance from the perspective of energy storage. Special attention is given to the capacitance dependence on electrolyte and electrode properties as well as thermodynamic conditions. Our discussion is mostly in line with recent efforts driven by the practical needs to maximize energy and power density by tuning the properties of supercapacitor materials. Because the focus of this review is on analytical models, simulation and experimental results are presented mainly as the support for the verification of theoretical predictions.

3.1. Electrodes with Subnanometer Pores

An electrode with a large surface area is, in general, beneficial to capacitive energy storage.[145] However, the areal capacitance is not simply a constant as predicted by the Helmholtz model but depends on, in addition to the electrical potential and electrolyte composition, the pore size and electrode structure. Because the precise meaning and experimental procedure for the characterization of surface area are often poorly defined for materials with microscopic pores, there are substantial difficulties in establishing a quantitative relation between the EDL capacitance of a porous electrode and the pore size and surface area.[146]

The effects of subnanometer pores on capacitive energy storage had been investigated for decades.[147] It was often conjectured that micropores were "inadequate" for supercapacitors because they might be inaccessible to charge carriers and result in sluggish charging dynamics. Conventional wisdom was that mesoporous electrodes with the highest specific surface area would maximize the EDL capacitance. The presumption was challenged by Chmiola and co-workers who reported an anomalously large capacitance for electrodes with subnanometer pores.[148] This landmark work inspired a string of computational and experimental efforts to reexamine the pore-size effects on supercapacitor performance.[149−168]

Although later experimental studies were less affirmative on the anomalous capacitance for electrodes with subnanometer pores,[151] most theoretical works corroborate the rise of capacitance when the pore size is reduced to the subnanometer scale. Regrettably, there is yet no consensus on the physical origin due to the adoption of a wide range of EDL models. Early analytical and MC studies by Kondrat et al. indicate that the anomalous increase of the capacitance may be attributed to screened electrostatic interactions between ions in subnanometer pores.[159,169] The possibility of a voltage-induced first-order transition has been identified for ionic liquids in slit pores either with or without the image charge effects that arise from the discontinuity of the dielectric constant at the electrode−electrolyte interface.[168,169] On the other hand, coarse-grained models and atomistic MD simulations of ionic liquids in slit pores suggest that the increase in capacitance is related to EDL overlap such as the interference of EDLs from the opposite surfaces of a slit pore.[157,170] The enhanced capacitance in microporous carbon electrodes has also been attributed to the separation of the positive and negative ions[171] and to the increase of curvature.[172]

As shown in Figure 7A, cDFT calculations predict an oscillatory dependence of the capacitance on the pore width.[118,155] The maximum capacitance occurs when the pore size is close to the ion diameter, in good agreement with an unusual increase of capacitance reported in the experimental work.[173] The capacitance profile resembles the layering structure of ionic liquids near a charged wall, and the EDL interference is evident from the coinciding peak positions.[170] Using atomistic simulations, Wu et al. examined the EDL structure of ionic liquids in nanopores taking into account the ionic structure and the polarizability of electrode atoms.[156] The simulation results were reproduced in Figure 7B, which shows a U-shaped curve for the dependence of capacitance on the pore width. The oscillatory profile became apparent when larger slit pores were simulated.[157] Figure 7C shows that the capacitance exhibits two peaks, located at 0.7 and 1.4 nm, which are

https://doi.org/10.1021/acs.chemrev.2c00097
Chem. Rev. XXXX, XXX, XXX−XXX

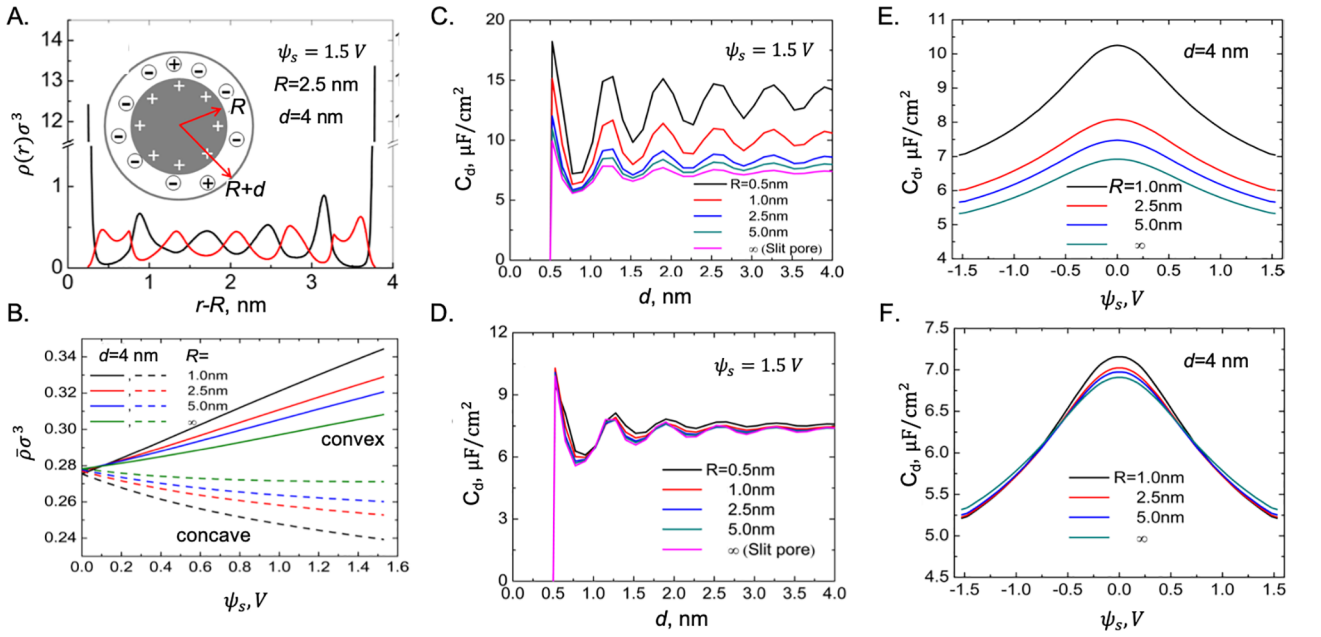

Figure 8. A spherical shell model of the EDL. A. Density profiles of cations and anions predicted by cDFT with the RPM representation of an ionic liquid at 298 K and 1 bar. B. The average densities of counterions (solid lines) and co-ions (dashed lines) inside the spherical shell at different curvatures and surface potentials. C and D: Pore size effects on the integral capacitance at convex (C) and concave (D) surfaces. E and F: Potential effects on differential capacitance at convex (E) and concave (F) surfaces. Adapted from ref 186. Copyright 2016 American Chemical Society.

commensurate with the ion diameter. The first peak decays from 0.7 to 1 nm, in quantitative agreement with experimental results (inset).[157] As the pore size increases from 1.0 to 1.8 nm, the appearance of the second peak affirms the oscillatory behavior predicted by cDFT. The oscillatory dependence of the EDL capacitance on pore width for confined ionic liquids was also reproduced by constant-voltage grand-canonical Monte Carlo (GCMC) simulation.[162,163] Because of the complex structure of realistic porous materials and pore size distribution, the oscillatory profile may explain why the pore size effect is not easily observable in experiments. Based on MD simulation for nanoporous carbon electrodes, Lahrar et al. found that, even with the same average pore size, electrodes with more ordered structure would have a much higher capacitance than those with more disordered structure and a broader pore size distribution.[167] The simulation results corroborate earlier theoretical and experimental results reported by Kondrat et al. indicating that electrodes characterized by the same average pore size may have very different capacitive properties.[174,175]

3.2. Pore Shape and Curvature Effects

As most carbon electrodes contain micropores with complicated morphology and size distributions, the joint effects of pore size and geometry on the EDL capacitance have been extensively studied through both experimental and computational means. From the computational perspective, three types of pore geometries are commonly used in theoretical investigations: (i) planar surfaces (e.g., a flat surface or slit pores), (ii) cylindrical pores with their concave inner surfaces or cylindrical particles with their convex outer surfaces (e.g., carbon nanotubes), and (iii) spherical surfaces (e.g., onionlike carbons). The slit and cylindrical pore models are commonly used for the characterization of porous material by gas adsorption. While these simplistic models do not reflect the complex microscopic structures of porous carbons, they capture the pore size and curvature effects in good agreement with experimental observations.[176−182] More realistic amorphous pore structures have also been adopted in MD simulation for understanding the electrochemical behavior of ionic liquids in porous carbon electrodes.[183]

Reindl et al. studied the curvature effects on the capacitance of electrolytes in contact with planar, spherical, and cylindrical electrodes using the PB equation and cDFT.[184,185] With the so-called civilized model for an aqueous solution of monovalent ions at room temperature, the theoretical analysis indicates that the differential capacitance per unit area falls with the curvature near a macroscopic surface, while the trend is opposite in the limit of small wall radius. The surface charge density has a strong effect on the capacitance for electrodes with small curvatures, whereas the surface-charge effect is negligible for electrodes large curvatures.

In general, a micropore with curved boundaries promotes the separation of positive and negative ions, yielding a higher capacitance. The magnitudes of ion segregation and capacitance increase depend on the curvature as well as the applied potential. The integrated effects can be represented by a generic model proposed by Lian and co-workers that accounts for both pore size and curvature effects.[186] As shown in Figure 8A, the local density of an ionic liquid confined in a spherical shell exhibits an oscillatory profile similar to that in a slit pore. However, the pore curvature has strong effects on the difference between the average densities of cations and anions (Figure 8B), which explains the significant improvement of capacitance as the curvature increases. In addition, the curvature enhances the oscillatory variation of the capacitance with the pore width (Figure 8C). Interestingly, the convex and concave geometries of the electrode−electrolyte interface show divergent curvature effects (Figure 8D). In the former case, the capacitance rises as the interface becomes more curved, but such an effect is almost nonexistent near a concave surface. The differential capacitance also shows significant improvements near a convex surface as the curvature increases. However, such an effect is marginal if the

https://doi.org/10.1021/acs.chemrev.2c00097
Chem. Rev. XXXX, XXX, XXX−XXX

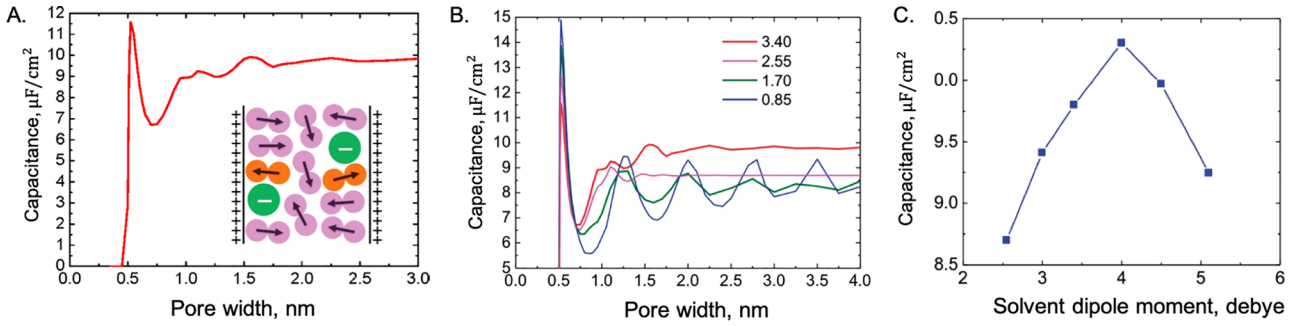

Figure 9. Solvent effects predicted by cDFT. A. Integral capacitance of a nanoporous electrode at 1.5 V as a function of the pore size. Here, the cDFT calculations were based on a civilized model of organic electrolytes with the solvent dipole moment equal to 3.4 debye. The inset illustrates the main features of the EDL structure, with the antialigned dipoles shown in orange color. B. The combined effect of solvent polarity and electrode pore size on the integral capacitance of organic electrolytes. The different lines correspond to solvents with different dipole moments in the units of debye. C. Variation of the integral capacitance with the dipole moment of the solvent. (A) Reproduced from ref 158. Copyright 2012 American Chemical Society. (B and C) Reproduced with permission from ref 193. Copyright 2016 Royal Society of Chemistry.

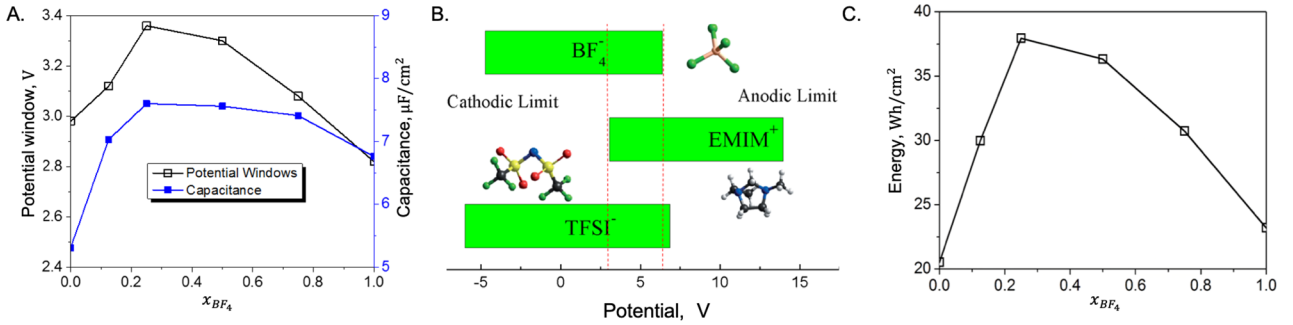

Figure 10. Enhancing the capacitive performance of supercapacitors with ionic-liquid mixtures. A. The operating potential window (OPW) and integral capacitance versus the ionic composition as a function of the mole fraction of BF_4 in EMI-TFSI/EMI-BF_4 mixtures. B. The relation between OPW and the cathodic/anodic limits of individual ions. C. Energy density versus the mole fractions of EMI-BF4 in the ionic-liquid mixture. Reproduced from ref 199. Copyright 2018 American Chemical Society.

surface is concave (Figure 8E and F). Through constant potential MD simulations for an organic electrolyte confined between rippled graphene electrodes, Seebeck et al. showed that the convex part of the electrode makes a higher contribution to the capacitance.[187] The applied voltage determines whether a convex or concave surface contributes to increased capacitance. Although a higher capacitance is typically observed for the convex part of the electrode, at low voltage, the differential capacitance is dominated by changes in the electric double-layer composition in the concave part of the electrode. Qualitatively, the theoretical predictions agree well with MD simulations based on more realistic models of ionic liquids and porous electrodes.[171,188] Both simulation and cDFT studies suggest that capacitive energy storage can be improved by utilizing electrodes with a large number of highly curved pores.

3.3. Solvent Effects on EDL Capacitance

Organic electrolytes such as TEA-BF_4 dissolved in acetonitrile (ACN) or propylene carbonate (PC) are commonly used in commercial EDLC devices. While the solvent effects are important for understanding both the capacitance and charging mechanism,[189] conventional EDL models describe the solvent as a dielectric continuum thus are not able to account for desolvation and other solvent explicit interactions. Although an atomistic representation of solvent molecules is beyond the scope of theoretical analysis, we may glean useful insights from cDFT calculations based on relatively simple ionic-liquid models.[158,190−193]

While there have been many theoretical studies for the pore size effects on the capacitance of ionic liquids, relatively few publications were devoted to organic electrolytes despite their broad use in commercial supercapacitors.[194] Using cDFT and a dimer model for organic solvents, Jiang and Wu investigated the capacitance of an organic electrolyte (TEA-BF_4/ACN) in nanoslit pores.[158] As shown in Figure 9A, except a sharp peak due to desolvation when the pore size is comparable to the ion diameter, there is little variation of the capacitance with the pore size. The trend is not much different from what was observed from experiment.[149,150] In stark contrast to the strong oscillatory dependence of capacitance on pore size for ionic liquids, the peak value is not significantly different from that at the large-pore limit (Figure 9B). When the solvent dipole moment is sufficiently large, the capacitance is near constant because, as schematically illustrated in the inset of Figure 9A, the EDL structure mostly consists of counterions and highly organized solvent molecules. The polarized solvent molecules disrupt the alternation of anion−cation layers near the charged surface, hence dampening the oscillation of capacitance with the pore size.

Figure 9C shows the effects of solvent polarity for organic electrolytes with different dipole moments. The volcano-shaped curve suggests that the capacitance may be maximized by tuning the dipole moment of the solvent. Although the dimer model is oversimplified in representing any realistic organic solvent, this work illustrates the rich behavior of organic electrolytes inside porous electrodes and provides useful guidance for selecting

https://doi.org/10.1021/acs.chemrev.2c00097
Chem. Rev. XXXX, XXX, XXX−XXX

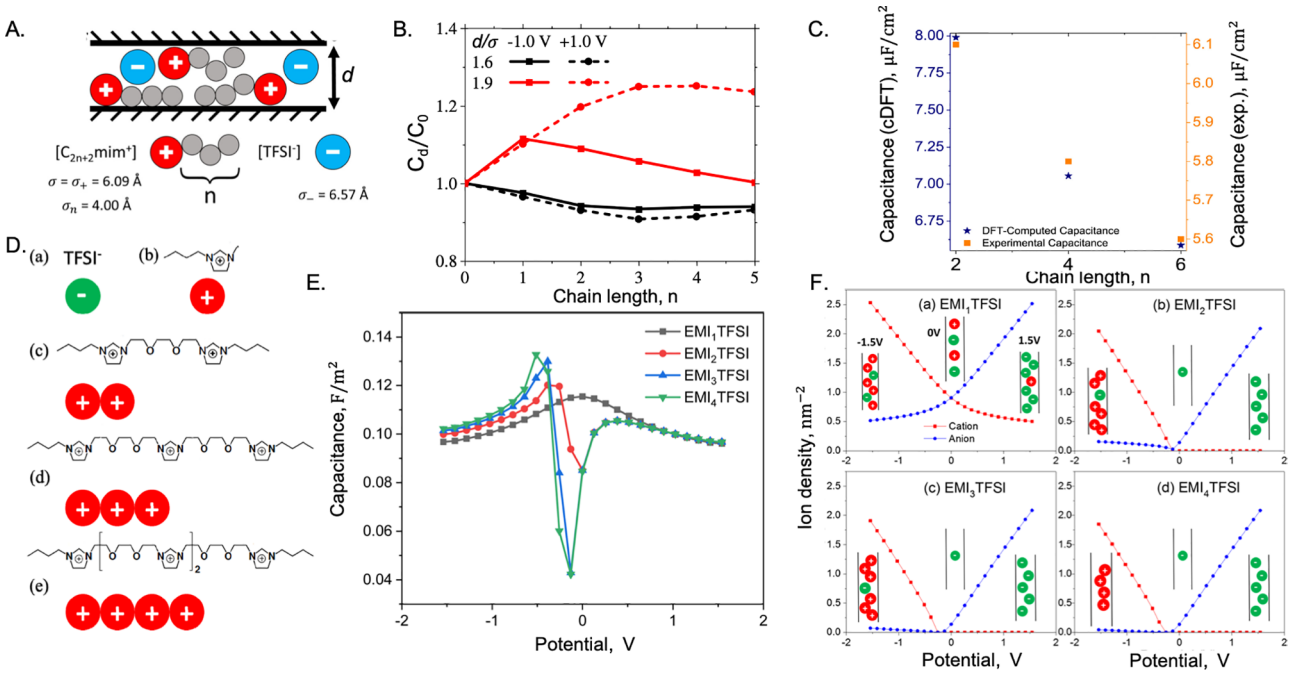

Figure 11. A. Schematic representation of an ionic liquid consisting of imidazolium cations paired with TFSI anions. B. The normalized integral capacitance versus the alkyl chain length of cations. C. A comparison of theoretical and experimental values of capacitance versus the alkyl chain length. D. Oligomeric cations represented by tangentially connected chains of identical charged particles. E. Differential capacitance as a function of the applied potential for oligomeric ionic liquids. F. Average number of densities of oligomeric cations and monomeric anions inside a nanopore of width d = 0.8 nm. (A and B) Reproduced with permission from ref 206. Copyright 2019 Taylor & Francis. (C) Reproduced with permission from ref 207. Copyright 2018 Elsevier. (D and E) Reproduced from ref 211. Copyright 2018 American Chemical Society.

organic electrolytes to enhance the electrochemical performance.

3.4. Advantages of Ionic Mixtures

Mixing an ionic liquid with other ionic liquids or cosolvents alters the bulk properties such as diffusivity, viscosity, and electrical conductivity.[195] Furthermore, ionic-liquid mixtures may have superior operating potential windows (OPWs) and the ability to charge and discharge over long periods of time without losing performance.[196] In combination with experimental studies and first-principle calculations, cDFT predicts that an optimal composition may be identified to maximize the EDL capacitance concomitant with an expanded OPW and improved ionic dynamics.[165,197−201] For example, Lian et al. investigated the potential window, interfacial structure, capacitance, and energy density of ionic-liquid mixtures consisting of one common cation and two anions of different sizes.[197−199] As shown in Figure 10, the theoretical results indicate that the capacitance varies nonlinearly with the ionic composition. It exhibits a maximum for a binary mixture of EmimTFSI/EmimBF$_4$ approximately at a 4:1 ratio. The effect can be attributed to a significant reduction of the layering structures and an enhanced contact density of Emim$^+$ counterions on the electrode surfaces due to the presence of smaller BF_4^- anions. Interestingly, the optimal composition coincides with the maximum OPW and a much improved energy density.

In the presence of ionic species with the same valence and similar nonelectrostatic interactions, cDFT predicts that a charged micropore is always small-ion selective. In particular, small ions often dominate the EDL behavior at high electrode potentials. While small ions enhance both the EDL capacitance and the accessibility of micropores, a mixture containing ions of different sizes may yield a capacitance higher than those corresponding to pure ionic liquids, owing to more efficient ion packing near the charged surface hence a larger charge density.[165,202] Besides, the presence of ions of different sizes affects the potential of zero charge (E_{pzc}) that is directly related to the integral capacitance and electrochemical potential window.[203] At certain conditions, the improvement is on a par with the anomalous capacitance rise for pure ionic liquids in electrodes with ultranarrow pores. The theoretical insights promoted further experimental exploration of the beneficial effect of ionic liquid mixtures for capacitive energy storage.[204] Simultaneous enhancement of the power and energy densities can be achieved by using mixtures with different types of ionic interactions. The enhancement of the differential capacitance, nearly 3 times higher compared to those for pure ionic liquids, was achieved by an appropriate combination of multiple cations and anions with large size asymmetry.[205]

3.5. Tuning Ionic Structure

One major advantage of using ionic liquids in supercapacitors is that a broad range of cations and anions can be selected to optimize the device performance. However, the parameter space is vast because organic ions have highly complex structures with diverse functional groups and branched backbones. While atomistic models are necessary in order to describe the chemical details, theoretical studies based on coarse-grained models are useful to identify the trends on the relation between the ionic structure and capacitance. For example, cDFT was used to investigate the effects of cation side chains on the capacitance of imidazolium-based room-temperature ionic liquids in the micropores of carbon electrodes.[206−209] By quantifying the important characteristics of the ionic species as shown schematically in Figure 11A, the theoretical results indicate

https://doi.org/10.1021/acs.chemrev.2c00097
Chem. Rev. XXXX, XXX, XXX−XXX

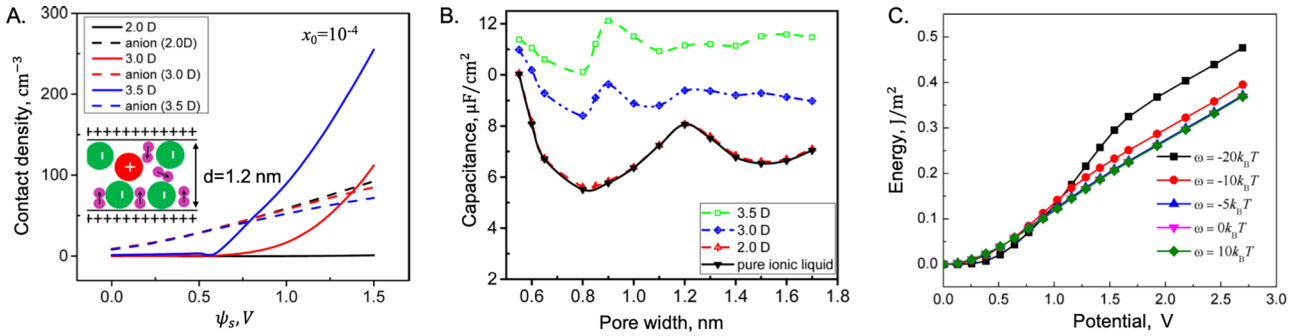

Figure 12. Enhancing the capacitive performance with polar additives. A. Contact densities of the anions (dashed lines) and the negative segment of the additive molecule (solid lines) versus the surface electrical potential. Here, the pore width is fixed at 1.2 nm, and the solid lines correspond to additives with a dipole moment of 2.0, 3.0, and 3.5 debye (D), respectively. B. Integral capacitance versus the pore size for the pure ionic liquid and its mixture with additives of different dipole moments. The surface potential is fixed at +1.5 V. C. Energy per surface area as a function of the applied potential with impurities of different surface energies (ω). (A and B) Reproduced from ref 213. Copyright 2016 American Chemical Society. (C) Reproduced from ref 215. Copyright 2017 American Chemical Society.

that, at moderate electrode potentials, the capacitance can be increased by attaching neutral segments to the cations (Figure 11B). However, the neutral segments may have negative effects on the capacitance for an electrode with large micropores or at high potential (Figure 11C). The opposite trends on the side-chain effects reflect a competition between the depletion of co-ions by the neutral segments (positive effect on capacitance) and the increased overall size of the cations (negative effects). The theoretical results explain why contradictory conclusions were reached regarding the effects of the alkyl chain of imidazolium cations on capacitance.[210]

Figure 11D shows a similar coarse-grained model that was used to investigate the capacitive performance of oligomeric ionic liquids (OILs) in nanoporous electrodes.[211] In contrast to their application to field-effect transistors, the capacitive performance of OILs in nanoporous electrodes is sensitive to the charging potential (Figure 11E). The charging curves could be understood by considering the average number densities of cations and anions inside the nanopores (Figure 11F). At low electrode potential, the average densities of the cations and anions versus the surface potential are near symmetric, suggesting the exchange of co-ions (cations) in the pore with the counterions (anions) from the bulk. In this case, the differential capacitance decreases sharply because ion adsorption becomes saturated at a small electrical potential. At high electrode potential, co-ions are depleted from the pore, and the charging process is dominated by counterion insertion, which leads to a slower decline of the differential capacitance. Unlike monomeric ionic liquids, virtually no oligomeric cations and only a few anions enter the nanopore at low charging potential.[211] When the absolute value of the surface potential increases (for either positively or negatively charged pores), the differential capacitance rises as more counterions are transferred into the pore from the bulk. A further increase of the electrode potential leads to the saturation of counterions inside the nanopore, as manifested in the decline of the differential capacitance. As a result, the differential capacitance–potential curves exhibit a "Bactrian camel shape", which is different from the "bell" shape for monomeric ionic liquid. A bell shape to camel shape transition varies with different oligomeric cations, indicating that the chain length of cations may lead to different charging mechanisms.[211] Although oligomeric cations show little advantage for the electrical charging of a positive electrode, they enhance the energy storage density for negative electrodes. Qualitatively, the cDFT predictions agree with the NMR study of the structure and dynamics of ionic liquids confined in porous carbon electrodes.[212]

3.6. Impurities and Additives

Supercapacitor performance is sensitive to ion distributions at the electrode–electrolyte interface which can be easily altered by adding chemicals to the electrolyte or in the presence of impurity. Such effects have been studied with cDFT based on a coarse-grained model of room-temperature ionic liquids. While the theoretical investigation captures only the generic features of impurity molecules, such as the molecular size, polarity, self-interaction energy, and binding affinities with the electrode surface and surrounding ions, it provides useful insights in understanding both positive and detrimental influences of impurity on ion distributions as well as capacitive energy storage in porous electrodes.[213,214]

Figure 12 illustrates some possible impurity effects on the surface concentration, capacitance, and energy density. Here, the cDFT calculations are based on the primitive model of ionic liquids with the impurity molecule represented by a dimer of oppositely charged spheres. As shown in Figure 12A, the contact density of impurity molecules can reach up to 400 M, and even its molar fraction in the bulk is only $x_0 = 10^{-4}$. As a result, the impurity has drastic effects on the capacitance and energy density (Figure 12B and C). The theoretical predictions demonstrate that additives could be formulated to dramatically increase the EDL capacitance and energy density. By considering the differential capacitance of an aqueous electrolyte in contact with a planar electrode, Cats and van Roij demonstrated that the EDL properties could be influenced by trace amounts of divalent ions.[216]

3.7. Phase Transitions within EDL

An organic electrolyte may experience demixing or vapor–liquid-like phase transition in the bulk phase.[217] Meanwhile, ionic liquids exhibit rich nanostructures and self-assembly behavior in addition to bulk freezing.[218] Whereas there has been a long history of fundamental research on electrowetting and structural transitions at the surface of a planar electrode,[44] it remains a theoretical challenge to describe the phase behavior of ionic systems within the micropores of electrodes and predict their implications on capacitive energy storage. Here, we discuss only two types of phase transition that are relatively well understood, at least from a qualitative perspective. One stems

https://doi.org/10.1021/acs.chemrev.2c00097
Chem. Rev. XXXX, XXX, XXX–XXX

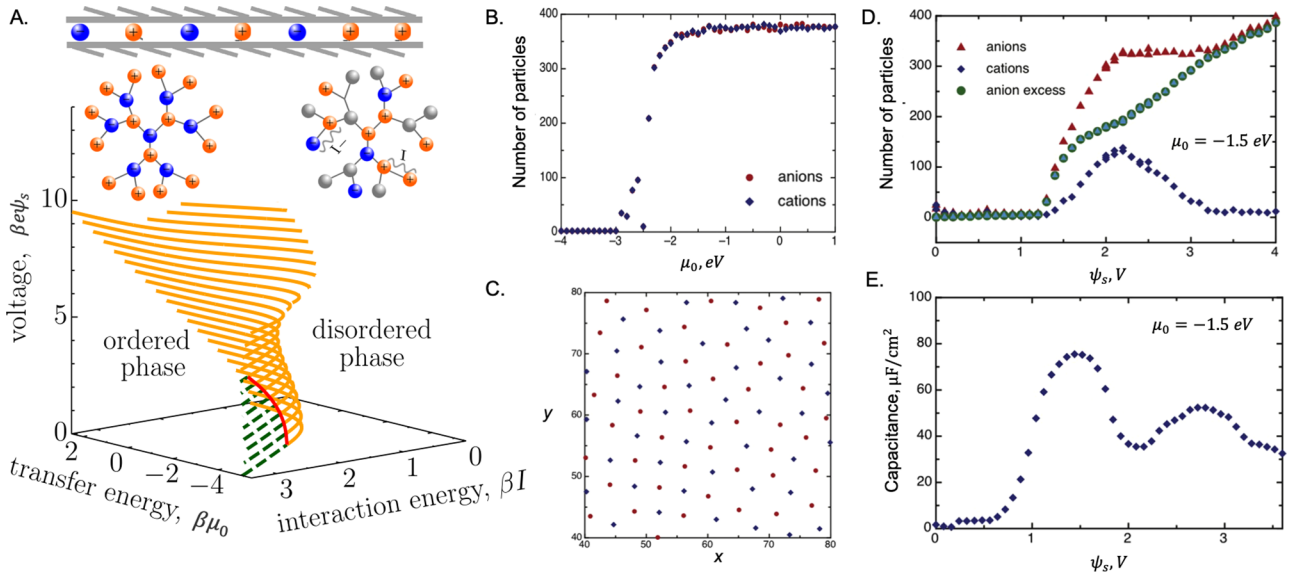

Figure 13. Two-dimensional (2D) representation of an ionic fluid confined between conducting walls. A. The Bethe lattice model predicts ordered-disordered transition in terms of ion transfer energy ($\beta\mu_0$), ion−ion interaction energy (βI), and applied voltage ($\beta e\psi_s$). The dashed green lines and solid orange lines stand for the first-order and second-order phase transitions, respectively, and the thick solid red line shows the tricritical points. B. Ion adsorption into a neutral slit pore predicted by grand-canonical Monte Carlo simulation. The number of particles was calculated within the quasi-2D simulation box of size 120 × 120 au^2. C. Snapshot from the simulation at the electrochemical potential of ions μ_0 = 1 eV. D. Ion adsorption in a slit pore (of 5 au width) versus applied voltage, ψ_s. E. The differential capacitance for the slit-pore system shown in Panel D. (A) Adapted with permission from ref 221. Copyright 2019 American Institute of Physics. (B−E) Adapted with permission from ref 222. Copyright 2020 Elsevier.

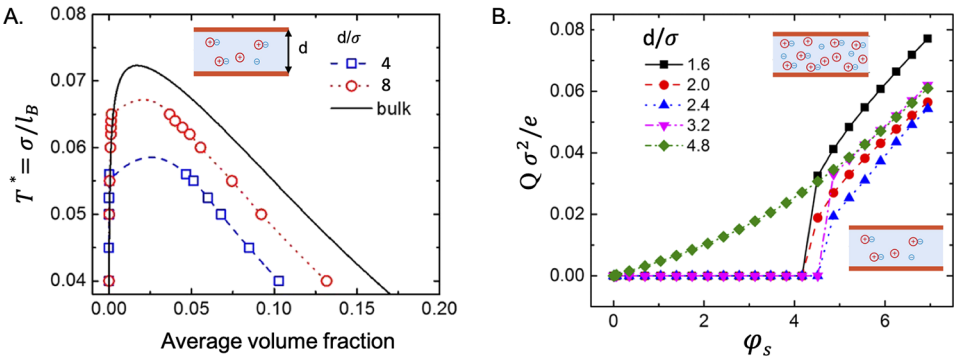

Figure 14. A. Phase diagrams for a model ionic fluid in the bulk (solid curve) and in two neutral slit pores of reduced width d/σ = 4 and 8. B. The surface charge density as a function of surface voltage in slit pores with different widths. Here, the total volume fraction of ions in the bulk is η_0 = 0.1194, and the reduced temperature is T^* = 0.05. All results are predicted by PM/RPM-cDFT. (A) Adapted with permission from ref 226. Copyright 2018 American Institute of Physics. (B) Adapted with permission from ref 47. Copyright 2020 American Institute of Physics.

from a single layer of ionic species in direct contact with the electrode surface or confined within extremely narrow slit pores. In this case, the phase behavior can be mapped into that corresponding to two-dimensional (2D) systems[219] and, at high voltage, is analogous to the Wigner crystallization of classical charged particles.[220] Another type of phase transition is affiliated with the demixing of the ionic system in the bulk phase. Unlike other factors influencing the supercapacitor performance, phase transitions are collective phenomena depending not only on ion-electrode interactions but also on thermodynamic conditions.

With the 2D representation of ionic species in a slit pore, it has been conjectured that electrostatic interactions are strongly screened by the confining surface such that they can be described in terms of nearest-neighbor interactions. In that case, the ionic system (a.k.a., "superionic liquids") may be mapped into the Ising models commonly adopted in the statistical-mechanical description of phase transitions.[223] For example, Figure 13A shows a complete phase diagram predicted by the classical spin-1 Blume-Capel (BC) model. In dimensionless units, the Hamiltonian of the 2D system is given by

$$\beta\mathcal{H} = J\sum_{\{i,j\}} s_i s_j - w\sum_i s_i^2 - h\sum_i s_i \tag{36}$$

where, in the context of a confined electrolyte with cations and anions of the same valence $\pm Z$, the spin variable $s_i = \{\pm 1, 0\}$ denotes a lattice site being taken by a cation, a anion, or void (or a solvent molecule for the case of an organic electrolyte), $w = \beta\mu_0$ represents the reduced chemical potential of ionic species, which is defined by the reversible work to transfer an ion from the bulk solution to the slit pore (viz., the reduced electrochemical potential of the bulk phase), $J = \beta I$ with I being the nearest-neighbor interaction energy, and $h = Ze\psi_s$ corresponds to the reduced electrostatic potential. For spins arranged on a 2D Bethe lattice, the BC model can be solved analytically.[221] It predicts that the 2D system may exhibit first-order, second-order, and re-entrant phase transitions (Figure 13A).

https://doi.org/10.1021/acs.chemrev.2c00097
Chem. Rev. XXXX, XXX, XXX−XXX

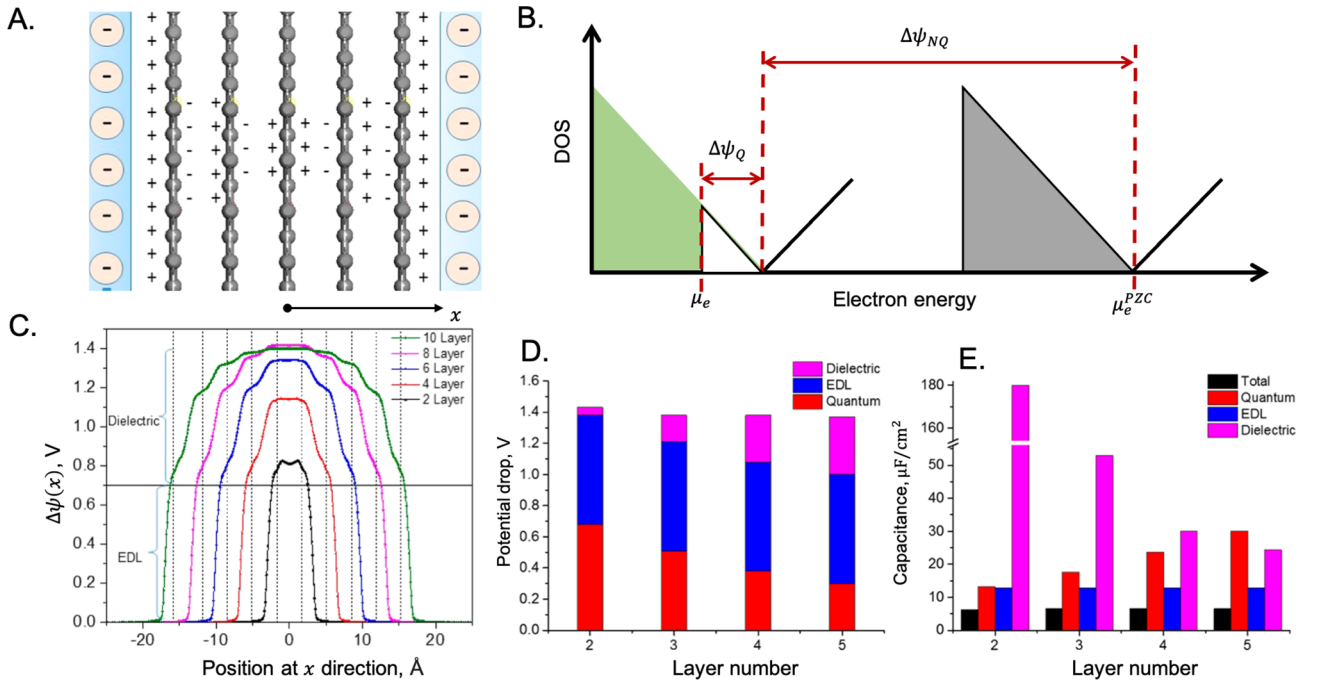

Figure 15. A. A model electrode consisting of a few graphene layers in contact with an electrolyte solution. B. Schematic of the density of states (DOS) at the potential of zero charge (the gray triangle on the right) and that at a positive surface charge (the green triangle on the left). According to the rigid band approximation (RBA), the DOS is shifted as a whole from the neutral state to the charged state in response to the change in the electron chemical potential from μ_e^{pzc} to μ_e. The electrode voltage includes contributions due to the quantum effect (viz., the reduction of the electron density) and nonquantum effect (NQ) related to charge distributions in the electrode and electrolyte. C. The local electrical potential predicted by Joint-DFT for different layers of graphene in a 6 M aqueous electrolyte under the same surface charge density of 9 μC/cm^2. The perpendicular dashed lines indicate the positions of graphene layers, and the horizontal line shows the surface potential predicted by Joint-DFT. D. Breakdown of the potential drop into quantum, dielectric, and EDL contributions for the model electrode. E. Corresponding capacitance contributions. Reproduced from ref 237. Copyright 2016 American Chemical Society.

Qualitatively, possible phase transition in a single layer of ionic species was predicted by an earlier mean-field theory that accounts for two-dimensional ion−ion interactions and image effects.[224] Subsequent MC simulation with an explicit consideration of the screened Coulomb interactions indicates that ion adsorption by a neutral slit pore follows a Frumkin-like isotherm ((Figure 13B and D)), but the adsorption is nonmonotonic in response to the surface potential, resulting in a "double-camel" shape for the capacitance (Figure 13E).[222] The simulation results show enhanced fluctuations in the transition from a gas-like to a "glass-like" structure, rending support for possible phase transitions predicted by the BC model. At zero voltage, cations and anions are self-organized into a square lattice (Figure 13C), corroborating a previous MD simulation for liquid−solid transition of the 1,3-dimethylimidazolium chloride ionic liquid confined between two parallel graphite walls.[225] Interestingly, the capacitance exhibits two maximums on both positive (Figure 13E) and negative (not shown) sides of the voltage. The unusual double camel curves can be attributed to ionophilic effects that lead to the depletion of co-ions at high voltage.

Qualitatively, the "vapor-liquid-like" phase transition for ionic systems in confined geometry has been well understood. The capillary phenomena can be described with cDFT,[47,226−231] van der Waals-type square-gradient methods,[232] the field-theoretical approach,[233] and the Landau−Ginzburg expansion.[86,234] As shown in Figure 14, the confinement leads to a narrowed vapor−liquid coexistence region and reduces both the critical temperature and the critical density as the pore width is reduced. The phase transition leads to discontinuity in the dependence of the surface charge on the electrical potential and the divergence of the capacitance at the critical point. In addition to slit and cylindrical pores, the ionic-vapor−liquid transition may take place in disordered porous matrices.[235] While the single-pore model is oversimplified for actual electrodes, we expect that the qualitative behavior of capillary condensation is independent of the pore shape and size distribution.

3.8. Quantum Capacitance

As discussed above (Section 2.4), quantum capacitance is associated with the variation of the electron density of the electrode in response to the voltage. The basic concept may be illustrated by considering a model electrode consisting of a few layers of graphene in contact with an electrolyte solution as shown schematically in Figure 15A. While the total capacitance can be calculated, in principle, from a grand-potential model that accounts for both electronic and ionic distributions, the rigid-band approximation (RBA) is often adopted to circumvent theoretical difficulties in predicting the electronic structure of the electrode in a liquid environment. As illustrated in Figure 15B, RBA assumes that the electron density of state (DOS) has a shape invariant with the electrode voltage. At a given electron chemical potential μ_e, the total electron charge can be estimated from[236]

$$Q_e \approx -e\int_{-\infty}^{\infty} \mathrm{d}E D_0(E)[f(E) - f(E-\mu_e)] \tag{37}$$

where $D_0(E)$ stands for the DOS at the potential of zero charge (pzc), and $f(E)$ is the Fermi−Dirac distribution function. Accordingly, we can calculate the quantum capacitance by

https://doi.org/10.1021/acs.chemrev.2c00097
Chem. Rev. XXXX, XXX, XXX−XXX

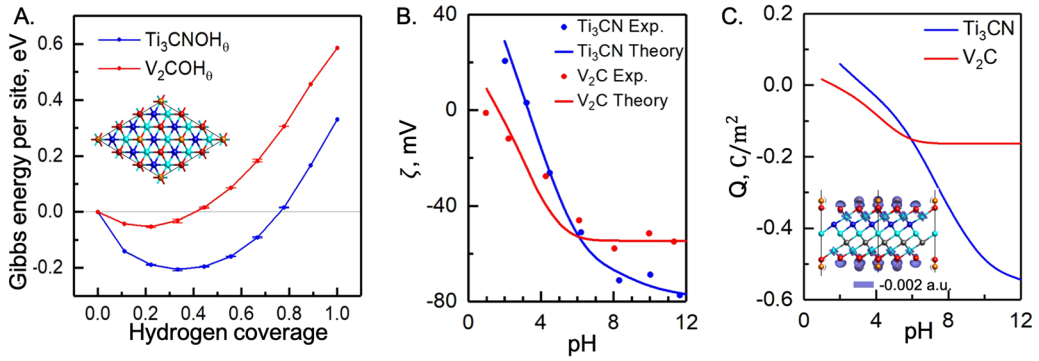

Figure 16. A. The formation Gibbs energies for two neutral MXenes at different surface coverages of hydrogen atoms (θ) predicted by Joint-DFT. The inset shows the surface configuration of the most stable structure for Ti_3CN. B. The pH dependence of the zeta potential and C. the surface charge density of the MXenes predicted by cDFT (lines). The symbols are experimental data, and the inset shows the delocalization of the surface charge upon charging. Adapted from ref 250. Copyright 2021 American Chemical Society.

differentiating the electron charge with respect to the electron chemical potential

$$C_Q = \frac{e^2}{4k_BTA}\int_{-\infty}^{\infty} D_0(E)\,\mathrm{sech}^2\left(\frac{E-\mu_e}{2k_BT}\right) \tag{38}$$

where A is the electrode surface area. Note that the total electron charge and the net charge of the electrode differ only by a constant related to the nuclear charge of the electrode atoms.

While RBA allows for the easy calculation of electrode charge from the DOS at pzc, it does not account for the influence of charging/discharging on the local electrical potential and charge distributions. The polarization effects include contributions from both the electrons and the electrolyte as manifested in the local charge distributions. The variations of the electrical potential can be subsequently used to define the dielectric capacitance and EDL capacitance, respectively (Figure 15C and D). Because the voltage encompasses the total electrical potential drop from the electrode to the electrolyte, the total capacitance is equivalent to that for quantum, dielectric, and EDL capacitance in a sequential connection[237]

$$\frac{1}{C_{total}} = \frac{1}{C_Q} + \frac{1}{C_\epsilon} + \frac{1}{C_{EDL}} \tag{39}$$

As the quantum capacitance is intrinsically related to electronic compressibility, a positive quantity for state systems, eq 39 suggests that the quantum effects always reduce the overall capacitance.

Figure 15E illustrates various components of the total capacitance predicted by Joint-DFT. It shows that the dielectric capacitance falls monotonically as the number of graphene layers increases from 2 to 5. The trend is opposite for the quantum capacitance, while the EDL capacitance of the diffuse layer remains a constant. For the particular system considered, the diffuse layer dominates the total capacitance, but the quantum and dielectric contributions are clearly non-negligible. We note in passing that the dielectric capacitance should not be confused with the image-charge effects that are conventionally considered to account for the screened ion−ion interactions due to the dielectric discontinuity at the electrode−electrolyte interface. Recent MD simulation studies indicate that the image charge near a metal surface may promote charge separation in the confined electrolyte, leading to a greater capacitance under an electric field.[238]

As discussed above, a number of theoretical approaches have been developed to describe electronic and ionic distributions self-consistently. While the importance of electronic structure has been emphasized in existing methods, further development is desirable toward a more faithful description of electrode−electrolyte interactions. Nevertheless, first-principle calculations reveal insights into charge storage mechanisms that cannot be captured by conventional EDL models. For example, Joint-DFT calculations indicate that quantum capacitance is important for the single-layer graphene, but its contribution to the total capacitance diminishes as the number of graphene layers increases.[236] Theoretical results from a combination of KS-DFT and MD simulation suggest that N-doping graphene in the 1 M $LiSO_4$ electrolyte has insignificant effects on the capacitance because the quantum capacitance is much higher than the EDL capacitance.[239,240] As most porous carbons have nanopores with stacked graphene layers at the surface, the theoretical investigations provide a good estimate of various chemical effects (e.g., doping) on the electrochemical performance.[241,242]

3.9. Pesudocapacitance

Pseudocapacitors are characterized by electron transfer at the electrode−electrolyte interface.[2] The conventional model was introduced by Conway and Gileadi based on the Frumkin isotherm.[243] To elucidate the basic idea, consider the under-potential deposition of a proton ($M + H^+ + e^- \rightarrow MH$) as an example. The Frumkin isotherm predicts that the surface coverage of hydrogen atoms θ is determined by

$$\frac{\theta}{1-\theta} = KC_{H^+}\exp[-\beta\psi_s e - g\theta] \tag{40}$$

where C_{H^+} stands for the bulk proton concentration, K is the proton binding constant, ψ_s is the electrical potential at the electrode surface, and $g > 0$ is a phenomenological parameter describing interactions between adsorbed hydrogen atoms. Because each proton carries one positive charge, the pesudocapacitance is thus given by

$$C_\phi = \frac{\partial Q_F}{\partial \psi_s} = \beta N_s e^2 \frac{\theta(1-\theta)}{1+g\theta(1-\theta)} \tag{41}$$

where $Q_F = -N_s\theta e$ is the electronic charge due to the surface reaction, and N_s stands for the number of proton binding sites per unit area. Numerically, a large value of g makes the dependence of the capacitance on the voltage resemble that of a

https://doi.org/10.1021/acs.chemrev.2c00097
Chem. Rev. XXXX, XXX, XXX−XXX

capacitor rather than that predicted by the Nernst equation for faradaic reactions.[244]

First-principles investigation of ruthenia-based pseudocapacitor suggests that the charge transfer at the electrode−electrolyte interface is not a local event as represented by the Nernst equation but involves the variation of the electronic structure of the entire electrode.[245] In other words, the Langmuir-type surface reaction does not provide a faithful description of the electrochemical behavior. Theoretical prediction of the charge transfer is challenging because the electronic structure depends not only on the electrical potential and electrolyte composition but also on the configuration of the adsorbed species in a highly heterogeneous environment.[246] The grand-canonical approach discussed above is not directly applicable to charge transfer without an explicit consideration of the electronic structure of both the electrode and reactive species. To circumvent such difficulties, existing methods to calculate pesudocapacitance are mostly focused on the specific binding of individual ions[247,248] or take a continuum approach to represent the electrolyte solution, often with the further assumption of a constant EDL capacitance.[249]

The first-principles approach for a self-consistent description of both the electrode and electrolyte has been actively pursed in recent years, and new developments are foreseeable. Before such methods (and reliable computer programs) are available, a combination of quantum and classical methods may serve some practical needs. For example, Figure 16 shows the atomic structure and surface charge of MXenes (i.e., 2D materials consisting of transition-metal carbides and/or nitrides) predicted by complementary first-principles and cDFT calculations. The first-principles method, here based on Joint-DFT, allows for the prediction of MXene termination at the neutral state. Meanwhile, in combination with a microkinetic model for surface reactions, cDFT can be used to predict the surface charge and composition in response to the electrode voltage and solution condition.[250] Although the hybrid method requires experimental data to fix the potential of zero charge and kinetic constants, it provides quantitative descriptions of the atomic composition as well as the electrochemical behavior of the layered nanostructured materials that are promising for diverse technological applications.[49]

4. DYNAMICS OF EDL CHARGING

EDL charging is a complex process coupling electro-osmotic flow, surface reactions, concentration, and pressure gradients. The charging dynamics is also closely dependent on the properties of both the electrolyte and electrode along with initial and boundary conditions. Although all factors could be considered through MD simulation in combination with first-principle calculations, the brute-force approach is computationally demanding even for relatively simple systems. In this section, we first summarize conventional macroscopic and microscopic models for describing the charging dynamics of porous electrodes. Next, we review recent developments and highlight their similarities and differences. Main results from the theoretical analysis will be discussed again in the context of capacitive energy storage along with relevant supports from molecular simulation and experimental characterization.

4.1. Classical Porous Electrode Theory

The dynamics of electrochemical processes is conventionally described by the volume-averaged porous electrode theory, a one-dimensional (1D) macroscopic model pioneered by Newman and co-workers.[54] The original concepts stem from the seminal work by Newman and Tobias published about 60 years ago.[251] Johnson and Newman first described the transient behavior of double-layer charging along with the energy and power densities of electrochemical capacitors.[252] Lin et al. extended the mathematical procedure to account for the charging dynamics with both pseudocapacitance and EDL capacitance.[253] More recently, Ferguson and Bazant reformulated the porous electrode theory using the principles of nonequilibrium thermodynamics and the Cahn−Hilliard theory of phase transformations.[254] Extensive surveys of the early literature are available in Newman's classical text on electrochemical systems.[54]

As shown schematically in Figure 17, an electrochemical cell for capacitive energy storage consists of two porous electrodes,

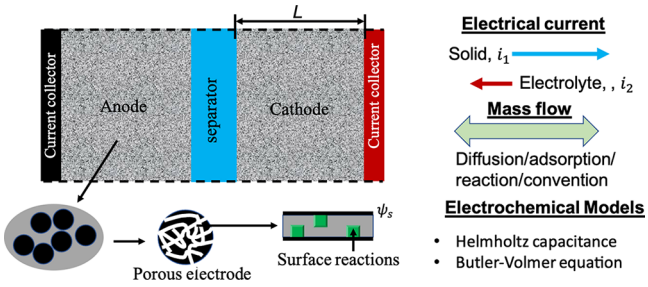

Figure 17. Schematic diagram of an electrochemical cell for capacitive energy storage. In the 1D representation of the porous electrodes, the electrical current and ion concentrations are described in terms of volume-averaged quantities varying only in the direction perpendicular to the cross section of the cell.

one positive and one negative, surrounded by an electrolyte. From a macroscopic perspective, the porous electrodes can be characterized by average porosity ϱ, specific surface area ϑ, and effective conductivity K_1. The classical porous electrode theory assumes that all dynamic variables can be represented by average quantities changing only in the direction perpendicular to the electrochemical cell. The charging dynamics is typically described in terms of a quantitative relation between the electrical current and the electrode voltage. Averaged over the cross-sectional area, the current density is described by Ohm's law[54]

$$i_n = -K_n \frac{\partial \psi_n}{\partial x} \tag{42}$$

where subscripts $n = 1$ and 2 represent the porous electrode and electrolyte, respectively, and x is the coordinate perpendicular to the parallel electrodes. The effective conductivity of the electrode depends on the pore structure and inherent conductivity of the solid material, and that for the confined electrolyte is often predicted by the empirical relation $K_2 = K_2^0 \varrho^{1.5}$, where K_2^0 is the conductivity of the bulk solution.[54]

The total current transferred from the electrode to the electrolyte includes contributions from the capacitive adsorption of ionic species and surface reactions[255]

$$\frac{\partial i_2}{\partial x} = \vartheta C_d \frac{\partial \Delta\psi}{\partial t} + \vartheta j_\phi \tag{43}$$

where $\Delta\psi \equiv \psi_1 - \psi_2$ is the difference between the local electrical potential of the solid ψ_1 and that of the electrolyte ψ_2, C_d is the differential capacity per unit area, and j_ϕ stands for the additional

https://doi.org/10.1021/acs.chemrev.2c00097
Chem. Rev. XXXX, XXX, XXX−XXX

current density due to chemisorption. Although pseudocapacitance is not necessarily affiliated with faradaic reactions,[256] its contribution is often described by the Butler−Volmer equation

$$j_\phi = j_\phi^0(e^{\alpha_a\varphi_o} - e^{-\alpha_c\varphi_o}) \tag{44}$$

where j_ϕ^0 stands for the exchange current density of a particular surface reaction, α_a and α_c are the anodic and cathodic transfer coefficients, respectively, and $\varphi_o \equiv (\Delta\psi - E_0)e/k_BT$ is the reduced overpotential with E_0 being the equilibrium potential for the electrode reaction. Charge balance requires

$$\frac{\partial i_1}{\partial x} + \frac{\partial i_2}{\partial x} = 0 \tag{45}$$

With the assumptions of no concentration gradient in the electrodes and the absence of pseudocapacitance, analytical expressions can be obtained relating the two electrical currents and the electrode voltage.[257] For general cases, a numerical scheme is required to solve the partial differential equations for the currents and local ion concentrations.[258,259]

The classical porous electrode theory provides a powerful mathematical framework to describe the dynamic behavior of electrode processes including the evolution of the local electrolyte concentration. It is often used to analyze the influence of electrode porosity, conductivity, and surface reactions on various charging modes (e.g., potentiostatic, potentiodynamic, and galvanostatic charging). However, the macroscopic procedure employs a large number of semiempirical parameters with drastic assumptions on capacitive processes (e.g., constant capacitance). To attain microscopic insights into charging dynamics and ion transport in porous electrodes, we often rely on simplified pore models.

4.2. Governing Equations for Ion Transport and Charging Dynamics

The molecular theories of ion transport and charging dynamics are mostly based on the Poisson-Nernst−Planck (PNP) equations. Similar equations but with corrections to thermodynamic nonideality can be derived in the context of nonequilibrium thermodynamics or classical time-dependent density functional theory (TDDFT).[260] In this subsection, we review the master equations for describing mass and charge transport in ionic systems. Their applications to model systems and specific problems of practical interest will be elucidated in the following subsections.

As is well documented, the PNP equations correspond to the ideal-solution model of ion transport. They predict that ion flux (relative the medium or solvent) is linearly proportional to the gradient of the local electrochemical potential

$$\mathbf{j}_i = -\upsilon_i\rho_i\nabla\mu_i \tag{46}$$

where υ_i stands for the ion mobility at infinite dilution. Substituting into the above equation the electrochemical potential of an ideal solution (id)

$$\mu_i^{id} = k_BT\ln(\rho_i\Lambda_i^3) + Z_ie\psi \tag{47}$$

leads to

$$\mathbf{j}_i = -D_i\left[\nabla\rho_i + \frac{\rho_iq_i}{k_BT}\nabla\psi\right] \tag{48}$$

where $q_i = Z_ie$ and $D_i = k_BT\upsilon_i$ are the ion charge and diffusivity, respectively. From the equation of continuity

$$\frac{\partial\rho_i}{\partial t} = -\nabla\cdot\mathbf{j}_i \tag{49}$$

we obtain the time-dependent form of the Nernst−Planck (NP) equation

$$\frac{\partial\rho_i}{\partial t} = D_i\nabla^2\rho_i + \nabla\cdot\rho_i\upsilon_iq_i\nabla\psi \tag{50}$$

where the first term on the right accounts for ion diffusion, and the second term represents electromigration, i.e., the ion flux due to the drift velocity $\mathbf{v}_i = -\upsilon_iq_i\nabla\psi$. A convection term, $\rho_i\mathbf{v}_0$, should be added to the flux in the presence of a net flow with solvent velocity $\mathbf{v}_0$.

At finite electrolyte concentrations, the NP equation must be modified in order to account for ion−ion interactions and correlation effects. In most cases, the modification amounts to the addition of an excess term in the electrochemical potential

$$\mu_i = k_BT\ln\rho_i + q_i\psi + \mu_i^{ex} \tag{51}$$

While conventional electrokinetic theories frequently express μ_i^{ex} in terms of the ionic activity coefficient derived from bulk electrolyte solution models, TDDFT provides a systematic way to describe the thermodynamic nonideality of inhomogeneous ionic systems.[260] At a finite ion concentration, the ion−ion interactions and correlation effects also affect the ion mobility.[261,262] The combined effects of thermodynamic nonideality and hydrodynamic interactions may lead to diffusive-convective transition.[263]

In practical applications, the NP equation is often formulated in terms of the local charge density $q \equiv \sum_i\rho_iq_i$ or the local total ion concentration $\rho_s \equiv \sum\rho_i$. For a system containing symmetric cations and anions with $D = D_+ = D_-$ and $Z = Z_+ = -Z_-$, the time evolution of the local charge density can be deduced from eq 50

$$\frac{\partial q}{\partial t} = D\nabla^2q + \frac{DZ^2e^2}{k_BT}\nabla\cdot(\rho_s\nabla\psi) \tag{52}$$

and that for the total ion concentration is

$$\frac{\partial\rho_s}{\partial t} = D\nabla^2\rho_s + \frac{D}{k_BT}\nabla\cdot(q\nabla\psi). \tag{53}$$

For weakly charged systems, the total ion concentration may be assumed spatially invariant. In that case, application of the Poisson equation to eq 52 leads to the Debye-Falkenhagen equation

$$\frac{\partial q}{\partial t} = D[\nabla^2q - \kappa^2q] \tag{54}$$

where $\kappa = \sqrt{\beta\rho_sZ^2e^2/\epsilon}$ is the Debye screening parameter. For one-dimensional systems, eq 54 has been solved analytically.[264,265]

Eqs 50, 52, and 53 can be solved numerically with appropriate initial and boundary conditions. For systems with faradaic reactions, these equations can also be combined with microkinetic models[266] and, in the presence of heat transfer or a net flow, with the Fourier equation[267] or the Navier−Stokes equation,[268−270] respectively. For concentrated electrolytes, the effects of interparticle interactions are commonly accounted for with a thermodynamic model for the excess chemical potential (μ_i^{ex}). Although the simple relation between ion flux and electrochemical potential, eq 46, is no more valid at high ion concentrations, the diffusion equation often keeps its conven-

https://doi.org/10.1021/acs.chemrev.2c00097
Chem. Rev. XXXX, XXX, XXX−XXX

tional form for simplicity, often with the ion mobility or diffusivity treated as a phenomenological parameter instead of a matrix.[101]

4.3. Pore-Scale Analysis

Pore-scale modeling provides a useful link between the microscopic details of ion transport and macroscopic patterns underlying the charging dynamics of porous electrodes. In many circumstances, the adoption of a single-pore model facilitates the derivation of analytical equations for both electrical current and variation of ion concentrations in response to an applied voltage. The analytical results not only are convenient for practical use but also are often instrumental in gaining fundamental insights into electrochemical processes that otherwise may be too complicated for theoretical analysis.

4.3.1. Transmission-Line Model. Huang et al. summarized the early literature and recent developments of the transmission-line (TL) model.[271] Here, our discussion is focused on its connection with the NP equation as originally established by de Levie in the early 1960s.[272] de Levie's model represents one of the most popular approaches to describe the charging dynamics of electrodes from the perspective of individual pores. It has been routinely used in the analysis of experimental electrochemical impedance spectra (EIS) of various porous electrodes.[273]

The basic idea of the TL model stems from the linearized NP equation. It assumes that the local ion densities are linearly dependent on the electrical potential

$$\frac{\partial \rho_i}{\partial t} \approx D_i \nabla^2 \rho_i + \rho_i^0 \upsilon_i q_i \nabla^2 \psi \tag{55}$$

where ρ_i^0 is the ion concentration in the bulk solution. Eq 55 is applicable to weakly charged systems containing a dilute electrolyte solution. Because of charge neutrality, $\sum_i \rho_i^0 q_i = 0$, it suggests that, in the presence of a symmetric electrolyte with monovalent ions of the same diffusion coefficient ($\upsilon_+ = \upsilon_- = \upsilon$), the total ion concentration ($\rho_s = \rho_+ + \rho_-$) follows Fick's law of diffusion

$$\frac{\partial \rho_s}{\partial t} = D \nabla^2 \rho_s \tag{56}$$

A comparison of eqs 53 and 56 reveals that the linearized NP equation neglects the effects of local charge on ion transport. In other words, it implies that the charge neutrality is satisfied almost everywhere inside the pore.

The linearized NP equation provides a convenient starting point to understand the charging dynamics for a straight pore of arbitrary shape (Figure 18). With additional assumptions that (i) the electrode is a perfect conductor; (ii) the pore size is much larger than the Debye screening length λ, and (iii) the EDL capacitance is a constant given by $C_d = \epsilon/\lambda$, the linearized NP equation predicts that both the electrical potential in the electrolyte (ψ) and the surface charge density of the electrode (q) respond to an applied potential according to the diffusion equation[274]

$$\frac{\partial q}{\partial t} = \mathcal{D}\frac{\partial^2 q}{\partial^2 x} \quad \text{and} \quad \frac{\partial \psi}{\partial t} = \mathcal{D}\frac{\partial^2 \psi}{\partial^2 x} \tag{57}$$

where x stands for the coordinate in the direction of the pore length, $\mathcal{D} \equiv \mathcal{A}D/(\mathcal{P}\lambda)$ is an effective diffusivity with $\mathcal{A}$ being the cross section area of the pore and $\mathcal{P}$ being the pore perimeter. For a straight pore, $l \equiv \mathcal{A}/\mathcal{P}$ is equal to the pore volume divided by its surface area (e.g., it is $a/2$ for a cylindrical pore of radius a). As the EDL capacitance is assumed as a constant, the local electrical potential in the electrolyte phase is linearly proportional to the surface charge density.

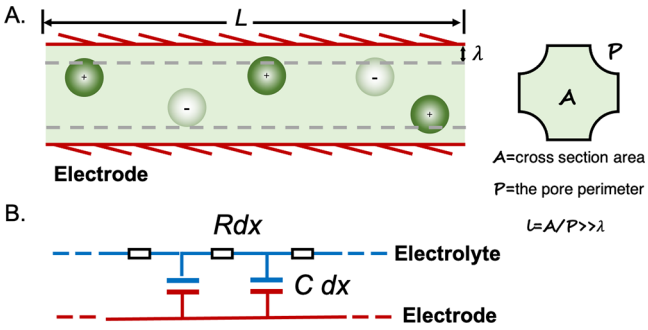

Figure 18. A. Schematic of a straight pore of length L, cross section area $\mathcal{A}$, and perimeter $\mathcal{P}$ containing a dilute electrolyte. B. When the Debye length λ is much smaller than the pore size (viz., $l = \mathcal{A}/\mathcal{P} \gg \lambda$), the charging dynamics can be represented by a transmission-line model with the resistance ($\mathcal{R}$) and EDL capacitance (C) per unit length treated as constants.

Eq 57 predicts that the time scale of EDL charging for a single pore of length L

$$\tau_{TL} \equiv \frac{L^2}{\mathcal{D}} = \frac{\lambda L^2}{Dl} \tag{58}$$

is, in general, different from the time scale of electrolyte diffusion, $\tau_D = L^2/D$. The physical meanings of these two time scales are also not the same. While τ_{TL} is affiliated with the accumulation of the surface charge, τ_D characterizes the time scale for the mass transport of neutral ion pairs. As discussed later, the diffusion time scale L^2/D emerges only at a later stage of charging when the applied potential is sufficiently large. For a dilute solution, the ionic conductivity is $K = \epsilon D/\lambda^2$. Accordingly, eq 58 can be alternatively written as

$$\tau_{TL} = \frac{C_d L^2}{Kl} \tag{59}$$

where $C_d = \epsilon/\lambda$ is again the Debye capacitance. As λ, D, K, and l are microscopic quantities that can be calculated from MD simulation while the pore length L is meso- or macroscopic, eqs 58 and 59 may be used to estimate the charging time of a macroscopic-scale device.[275]

The charging dynamics described by the linearized NP equation is equivalent to that of a transmission line (TL), i.e., an equivalent circuit consists of uniformly distributed resistors and capacitors, as illustrated in Figure 18, to account for ionic motions and electrical current due to the EDL charging, respectively. The TL model predicts that the variation of the electrical potential follows the diffusion equation

$$\frac{\partial^2 \psi}{\partial x^2} - (\mathcal{R}C)\frac{\partial \psi}{\partial t} = 0 \tag{60}$$

where $\mathcal{R}$ and C stand for the resistance and the EDL capacitance per unit pore length, respectively. Eq 60 is known as the TL equation, which is often adopted to fit experimental data from EIS measurements. A comparison of the TL equation with eq 57 reveals the physical significance of the TL parameters $C = \mathcal{P}C_d$, $\mathcal{R} = \lambda^2/(\mathcal{A}\epsilon D)$, and $\mathcal{R}C = \mathcal{D}^{-1}$.

https://doi.org/10.1021/acs.chemrev.2c00097
Chem. Rev. XXXX, XXX, XXX−XXX

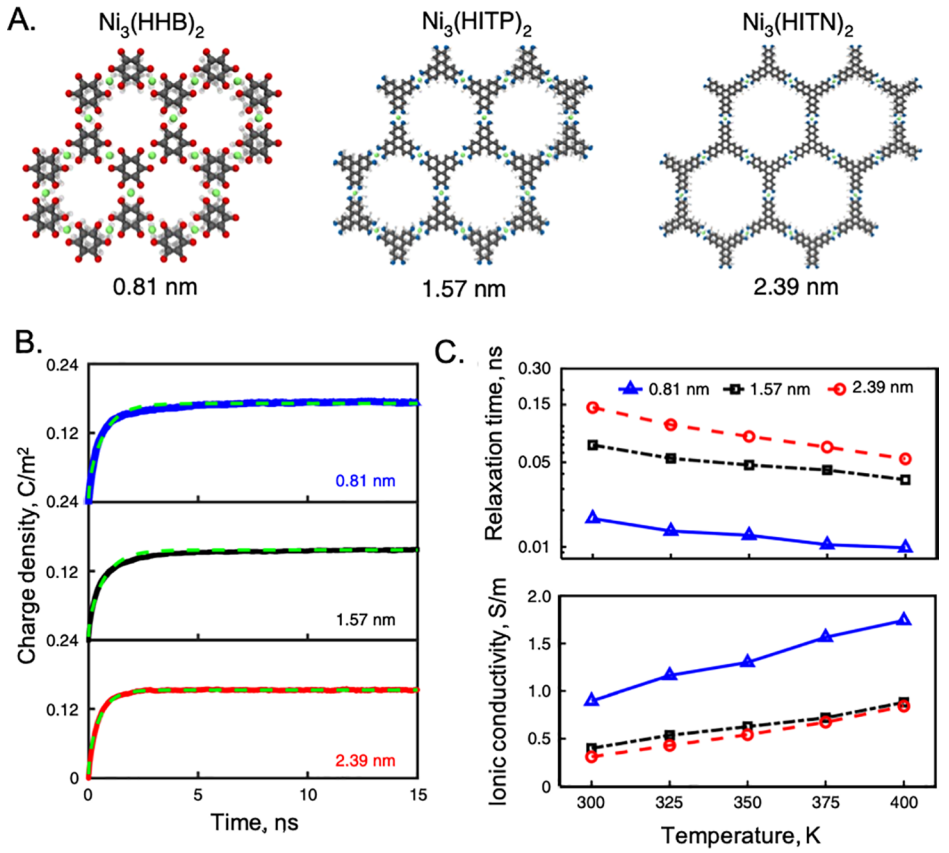

Figure 19. A. Atomic structure of quasi-1D pores in three MOF electrodes (the numbers at the bottom indicate effective pore diameters). B. Evolution of the charge density per surface area of positive MOF electrodes (ψ_s= 4 V) in [EMIM][BF_4] ionic liquid at 400 K. The solid lines are from MD simulation, and the dashed lines are fitted with the transmission-line model. C. Intrinsic relaxation time (top panel) and ionic conductivity (bottom panel) of the ionic liquid in the MOF pores at different temperatures. Reproduced with permission from ref 279. Copyright 2019 Springer Nature.

de Levie solved eq 60 analytically for a cylindrical pore of infinite length under potentiostatic, galvanostatic, galvano-harmonic, and potentio-harmonic charging.[272] For the potentiostatic charging of a straight pore, the initial and boundary conditions for eq 60 are given by $\psi(x, 0) = \psi(\infty, t) = 0$ and $\psi(0, t) = \psi_s$ (viz., the Dirichlet boundary condition). Accordingly, the electrical potential and the current density are given by[272]

$$\psi(x, t) = \psi_s \operatorname{erfc}(\sqrt{\tau/t})$$
$$i(x, t) = -\frac{1}{\mathcal{R}}\frac{\partial \psi}{\partial x} = \frac{\psi_s}{\mathcal{R}}\sqrt{\frac{\mathcal{R}C}{\pi t}}\exp(-\tau/t) \quad (61)$$

where $\operatorname{erfc}(x)$ is the complementary error function, $\tau \equiv x^2\mathcal{R}C/4$. Because the EDL capacitance is a constant, the time evolution of the local charge density can be directly obtained from eq 61[276]

$$q(x, t) = q_0 \operatorname{erfc}(\sqrt{\tau/t}) \quad (62)$$

where $q_0 = C\psi_s$ represents the equilibrium charge density of the electrode. Analytical solutions for eq 60 are also available with the Robin and Neumann boundary conditions, i.e., with $\psi(x, 0) = 0$ and $\partial\psi(x, t)/\partial x$ specified at the pore ends.[277,278]

For a straight pore of length L, the total charge accumulated per unit pore surface area of the electrode is given by[274,279]

$$Q(t) = \int_0^L q(x, t)\mathrm{d}x = Q_0\left[1 - \sum_{n=0}^{\infty}\frac{2}{A_n^2}\exp\left(-\frac{A_n^2 t}{\tau_{TL}}\right)\right] \quad (63)$$

where $A_n \equiv \pi(n + 1/2)$, and $Q_0 = C_d\psi_s$ is the equilibrium charge density. Taking the asymptotic limits of eq 63 leads to a square-root growth of the charge at short time[280]

$$Q(t)/Q_0 \approx \sqrt{\frac{\pi t}{\tau_{TL}}} \quad (64)$$

and an exponential relaxation at long time

$$Q(t)/Q_0 \approx 1 - \frac{8}{\pi^2}\exp\left(-\frac{\pi^2 t}{4\tau_{TL}}\right) \quad (65)$$

Strictly speaking, the linearized NP equation is valid only for electrochemical systems containing a dilute electrolyte in response to a weak electrode potential, i.e., when the surface potential ψ_s is comparable to k_BT/e. While these assumptions are not justified for practical systems, the TL model continues to see widespread use because, very often, it performs reasonably well thanks to the use of fitting parameters and/or cancellation of errors.[275,281] For example, Figure 19 shows the charging dynamics for metal−organic framework (MOF) electrodes in an ionic liquid. With the TL relaxation time as an adjustable parameter, the TL model was able to fit the MD simulation data at the applied potential as high as 4 V over a broad range of temperatures. Remarkably, it yields a reasonable relaxation time

https://doi.org/10.1021/acs.chemrev.2c00097
Chem. Rev. XXXX, XXX, XXX−XXX

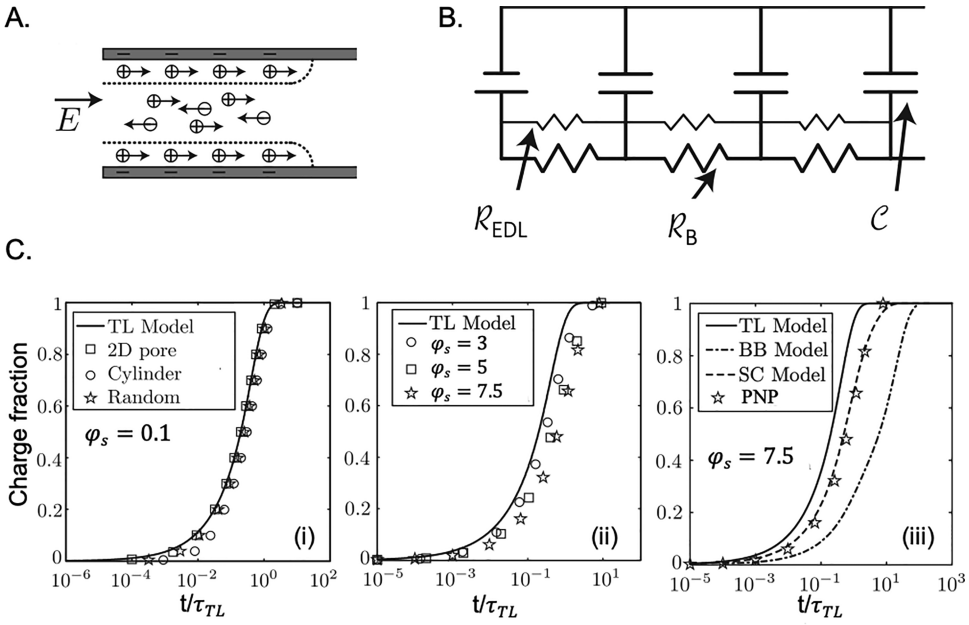

Figure 20. A. Schematic of ion motions in the center and surface regions of an electrode pore. B. The transmission-line model for describing the charging dynamics of a single pore. Here, $\mathcal{R}_{EDL}$ and $\mathcal{R}_B$ stand for the resistances per unit pore length for the surface and bulk ion conductions, respectively, and C is the EDL capacitance per unit pore length. C. Charging fraction, $Q(t)/Q_0$, versus the reduced charging time (t/τ_{TL}) during a potentiostatic charging process for (i) three straight pores of different morphologies at a low reduced applied potential ($\varphi_s \equiv \beta e\psi_s = 0.1$), (ii) the slit pore at higher electrode potentials ($\varphi_s = 3$, 5, and 7.5), and (iii) comparison of different charging models. Reproduced with permission from ref 274. Copyright 2004 American Physical Society.

in comparison with experiment.[279] Based on eq 59, the ionic conductivity was derived from the relaxation time and a constant EDL capacitance corresponding to electrode potential. As shown in Figure 19C, the TL model predicts that the ionic conductivity increases as the pore size falls. The surprising trend was attributed to the enhanced screening of electrostatic interactions due to the image charges induced by the pore walls (albeit the image effects are not accounted for by the TL model). Interestingly, MD simulation also reveals a non-monotonic relation between the charging rate and pore size due to in-plane structure transition.[282] In an earlier work,[280,283] Kondrat and Kornyshev demonstrated that the diffusion equation is also applicable to the charging dynamics of a metallic pore with a single layer of an ionic liquid. In that case, the diffusion coefficient was modified to reflect the screened ion−ion interactions due to the electronic polarizability of the metallic walls. The diffusion model was supported by MD simulation and experiments for charging and discharging dynamics of nanoporous supercapacitors with ionic liquids.[284]

4.3.2. Ion Adsorption and Surface Conductance. A number of theoretical procedures have been proposed to improve the TL model by circumventing the assumptions of a thin diffuse layer and a small applied potential.[285] For example, Biesheuvel and Bazant (BB) developed a modified TL model using the GCS theory for EDL capacitance and ion adsorption in the diffuse layer.[286] While de Levie's model suggests that the charging dynamics is independent of the electrical voltage, the BB model predicts that ion transport inside a straight pore is slowed significantly at higher potentials due to the nonlinear EDL capacitance and a net adsorption of ions in the electrode. Squires and co-workers extended the BB model by incorporating surface conduction due to ion mobility in the diffuse layer.[274]

Figure 20 compares the numerical results from the PNP equations with the predictions of de Levie's model and its recent modifications. As expected, de Levie's model (viz., eq 63) is able to reproduce the charging dynamics in excellent agreement with the PNP equations for three straight pores of different shapes at low charging potential (φ_s = 0.1 or $\psi_s \sim$ 2.5 mV). At slightly higher potentials, eq 63 performs reasonably well because the charge fraction is relatively insensitive to the applied potential. At dimensionless potential φ_s = 7.5 or $\psi_s \sim$ 200 mV, the surface conduction (SC), i.e., the current due to ion transport within the diffuse layer, becomes more important. While the SC model reproduces the numerical results from the PNP equations, the charging time was underestimated by de Levie's model yet overpredicted by the BB model. More recently, Aslyamov and Janssen provided analytical solutions to the nonlinear PNP equations and explained the initial RC-like relaxation and a diffusion time scale L^2/D at a later stage of charging at moderate to high applied potentials.[287]

4.3.3. Bridging the Gap between Small and Large Pores. The TL model breaks down when the diffuse layer thickness becomes comparable to the pore size (viz., $\lambda \sim l$). If the total ion concentration inside the pore is approximately invariant in the axial direction, the radial flux of charge in the electrolyte phase is negligible. In that case, Gupta et al. demonstrated that the electrical potential at the center of a cylindrical pore follows a diffusion equation similar to that given by de Levie's model (eq 60) but with different expressions for the resistance and EDL capacitance[288]

$$C = \frac{\pi a^2 \epsilon}{\lambda^2}$$

$$\mathcal{R} = \frac{\lambda^2}{\pi a^2 \epsilon D I_0(a/\lambda)} \tag{66}$$

where $I_n(r)$ stands for the nth-order modified Bessel function of the first kind, and a is the radius of the cylindrical pore. Because

https://doi.org/10.1021/acs.chemrev.2c00097
Chem. Rev. XXXX, XXX, XXX−XXX

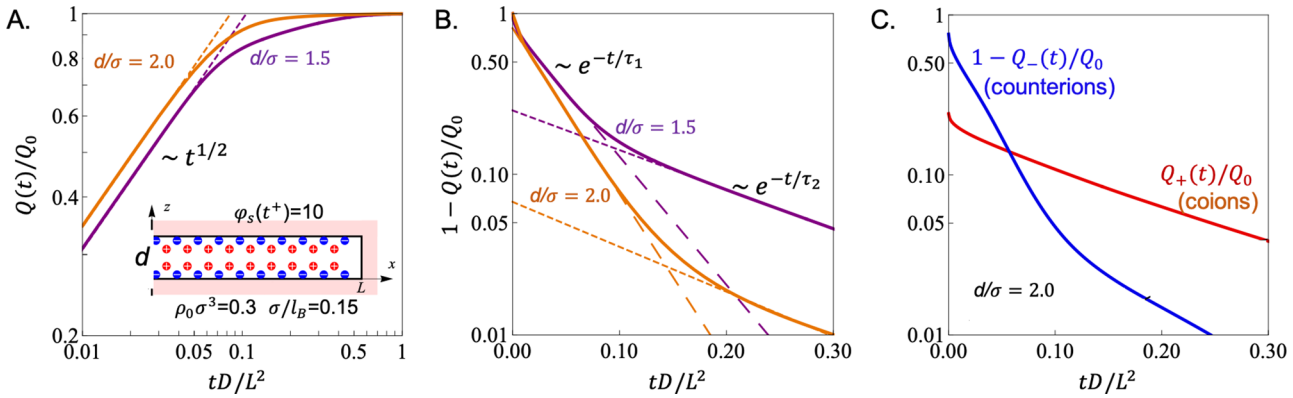

Figure 21. Charge evolution at early (A) and late (B) stages of charging for a slit pore in a concentrated electrolyte solution predicted by TDDFT. The model system approximates charging at 0.25 V for a porous electrode made of two-dimensional materials (e.g., graphene or MXenes) in a 4 M organic electrolyte (ion diameter $\sigma = 0.5$ nm) with the dielectric constant of 17 at room temperature. C. Contributions of cations and anions to the total charge pore charge. Reproduced from ref 289. CC BY: Creative Commons Attribution.

the diffuse layer occupies the entire cylindrical pore, the contribution of the EDL capacitor to the electrode charging is affiliated with a volumetric current source instead of a current proportional to the surface area in the thin diffuse layer limit. The effective resistance is reduced due to the enhanced ion concentration inside the pore.

More general expressions for the charging dynamics have been derived for cylindrical pores of arbitrary size under small applied potentials.[285] With the assumption of quasi-equilibrium for ion distributions in the radial direction, the linearized PB equation yields a simple expression for the local charge density

$$q(r) \sim \Delta\psi I_0(ra/\lambda) \tag{67}$$

where $\Delta\psi \equiv \psi_m - \psi_s$ stands for the difference between the electrical potential in the pore surface and at the pore center. At small applied potentials, the perturbation analysis predicts that the potential at the pore center follows the diffusion equation

$$\frac{\partial\psi_m}{\partial t} = \mathcal{D}'\frac{\partial^2\psi_m}{\partial^2 x} \tag{68}$$

where $\mathcal{D}' = \mathcal{D}I_0(a/\lambda)/I_1(a/\lambda)$. Accordingly to eq 68, the time scale for charging a cylindrical pore of length L is

$$\tau_{cyl} = \frac{2\lambda L^2}{aD}\frac{I_1(a/\lambda)}{I_0(a/\lambda)} \tag{69}$$

In the thin double-layer limit, $\lambda \ll a$ and $I_1(a/\lambda) \approx I_0(a/\lambda)$ so that $\tau_{cyl} \approx \frac{2\lambda L^2}{aD}$, the same as that predicted by the TL model, eq 58. In the overlapping double-layer limit, $\lambda \gg a$, we obtain $\tau_{cyl} \approx L^2/D$ from $I_0(a/\lambda) \approx 1$ and $I_1(a/\lambda) \approx a/(2\lambda)$, which is the same as the time scale of diffusion.

4.3.4. Analysis beyond the Dilute-Solution Paradigm. So far the pore-scale analysis has been primarily focused on the PNP equations. The dilute-solution model neglects ion−ion interactions and is not particularly relevant to the majority of electrochemical systems of practical interest. At finite ion concentrations, the thermodynamic nonideality can be incorporated into the PNP equations by adopting a local excess chemical potential for each ionic species

$$\mu_i^{ex}(\mathbf{r}) = \frac{\delta F^{ex}}{\delta\rho_i(\mathbf{r})} \tag{70}$$

Although the excess Helmholtz energy does not account for the influence of ion−ion interactions on ion mobility, diverse models are readily available to describe the EDL capacitance and other thermodynamic quantities in the equilibrium limit.

TDDFT was used, probably for the first time, by Aslyamov and co-workers to investigate the charging dynamics of porous electrodes in organic electrolyte solutions.[289] As shown in Figure 21, the model system consists of a slit pore in contact with an electrolyte solution represented by the restricted primitive model (RPM). The parameters were selected to mimic those corresponding to a nanoporous electrode such as graphene or MXenes in an organic electrolyte, and the excess chemical potential was derived from one of the most accurate versions cDFT to describe excluded-volume effects and electrostatic correlations.[118] TDDFT predicts that the evolution of the total charge follows a power law of the exponent 1/2 in the early stage of charging, followed by consecutive exponential decays in late time (Figure 21A and B). In the early and intermediate stages of charging, the dynamic behavior is remarkably similar to that predicted by the TL model, eqs 64 and 65, even at large voltage and high electrolyte concentration. The good agreement explains, at least in part, the successful applications of the TL model for practical systems. However, one should keep in mind that the time scale of relaxation, which is typically treated as an adjustable parameter in practical applications of the TL model, is, in general, dependent on the pore geometry and the electrolyte concentration as well as the applied potential.

For nanopore charging in a concentrated electrolyte solution, TDDFT predicts that the charge relaxation is notably slowed at late times. The second exponential decay agrees with earlier analytical results[286,287] and was also observed in MD simulation[290] and experiments.[291] At the late stage, the sluggish charging was attributed to the hindered release of co-ions due to the increase of the counterion concentration. Because of the crowding effects, counterion adsorption and co-ion release are strongly correlated.[292,293] While such correlation plays an important role for EDL charging in concentrated electrolytes,[294] it is relatively insignificant for dilute solutions as described by the TL model. Based on the numerical results from the TDDFT calculations over a broad range of conditions, Aslyamov et al. found that the two relaxation time scales can be estimated from[289]

https://doi.org/10.1021/acs.chemrev.2c00097
Chem. Rev. XXXX, XXX, XXX−XXX

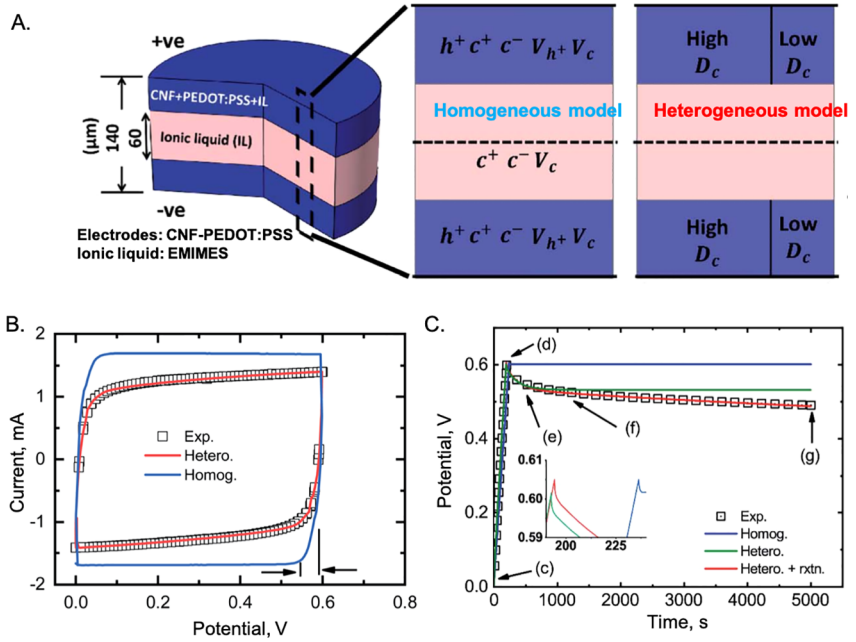

Figure 22. Modeling the dynamics of conducting polymer supercapacitors with the PNP equations. A. Schematic of the electrochemical cell and parameters used in the homogeneous (middle) and heterogeneous (right) models. Here, h^+ and $c^{\pm}$ stand for the concentration of holes and ionic species, V_{h^+} and V_c are the potentials of the electrode and electrolyte, respectively, and $\mathbf{D}_c$ represents a set of diffusion coefficients for the charge carriers. The heterogeneous model consists of two domains with different sets of $\mathbf{D}_c$. B. Cyclic voltammograms (scan rate 10 mV/s) fitted with the homogeneous and heterogeneous models. C. A comparison of the self-discharging potentials from theory and experiment. Reproduced with permission from ref 301. Copyright 2016 Royal Society of Chemistry.

$$\tau_1 \approx \frac{4}{\pi^2}\frac{Q_0 L^2}{e\rho_s^{\infty}\varphi_s dD}$$

$$\tau_2 \approx [\rho_s^{\infty}/\rho_s^{\infty}(\sigma/2) + 0.6(d/\sigma - 1)/\varphi_s]\frac{L^2}{D} \quad (71)$$

where d and L are the pore width and length, respectively, ρ_s^{∞} is the total ion density inside the pore at equilibrium, $\rho_s^{\infty}(\sigma/2)$ is the total contact density, and φ_s is the reduced surface potential. For charging a large pore at low electrolyte concentration, τ_1 becomes identical to τ_{TL}.

Importantly, TDDFT predicts reasonable time scales for the charging of a porous electrode and, thus, is able to bridge the enormous gap between ionic activities and device-level dynamics. For example, the initial relaxation time corresponding to the results shown in Figure 21B is 700 s for pore width d/σ = 1.5 and 400 s for d/σ = 2, which is about the same order of magnitude in comparison to experimentally observed charging time for supercapacitors. The characteristic time of pore charging is not the same as that corresponding to EDL formation at a planar surface. We note in passing that many assumptions can be avoided by solving PNP or TDDFT equations numerically, which becomes less of an issue even for high-dimensional systems as the computers become more and more powerful and user-friendly computer programs are readily available.[295,296]

4.4. Charging Dynamics for Electrochemical Cells

A canonical setup for understanding the dynamics of EDL charging consists of two parallel electrodes separated by a symmetric electrolyte, i.e., cations and anions have identical properties except opposite charge. An exhaustive historical review of the early literature can be found in the seminal paper by Bazant et al.[265] The model system is analogous to that typically used in the classical porous electrode theory but without the conducting matrix. Not only is the one-dimensional setup convenient for the theoretical analysis, but also it is directly applicable to certain electrochemical systems where the conducting matrix can be represented by a dielectric medium.

4.4.1. Equivalent-Circuit Model. One of the simplest representations of EDL charging is provided by an equivalent circuit (EC) model with a sequential connection of an electrical resistor and a capacitor for each electrode. For two parallel electrodes separated by a dilute electrolyte, we may estimate the resistance $\mathcal{R}$ from ion diffusivity D and half-cell length L, $\mathcal{R} = L\lambda^2/D\epsilon$, and the EDL capacitance from the linearized PB equation, $C_d = \epsilon/\lambda$. When the electrolyte is confined between two parallel electrodes applied with a sudden potential difference, the EC model predicts that the charge density at each electrode surface is an exponential function of the charging time t

$$Q(t) = Q_0(1 - e^{-t/\tau_{EC}}) \quad (72)$$

where $\tau_{EC} = L\lambda/D$ stands for the relaxation time, and Q_0 is the surface charge density at equilibrium. Note that the time scale for EDL formation $\tau_{EC} = L\lambda/D$ is much smaller in comparison with that for charging a single pore predicted by the TL model, $\tau_{TL} = L^2\lambda/Dl$. The ratio of these two time scales is equal to the pore length divided by the pore size, $L/l \gg 1$, which has been confirmed by direct measurements of nanoslit pore charging.[297]

4.4.2. The Debye-Falkenhagen Approximation. The Debye-Falkenhagen equation, eq 54, is often used to describe the charging dynamics for two parallel electrodes separated by a dilute solution. With appropriate boundary and initial conditions, the one-dimensional differential equation is amenable to analytical solutions.[264,298] The exact results indicate that the transient behavior of the charge density, as well as other

https://doi.org/10.1021/acs.chemrev.2c00097
Chem. Rev. XXXX, XXX, XXX−XXX

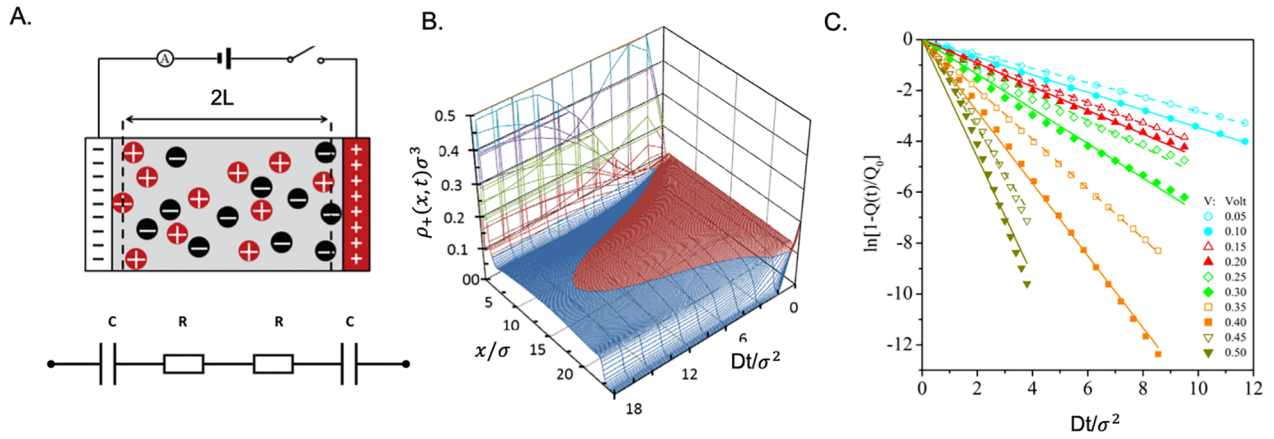

Figure 23. A. Schematic of an EDL cell and the corresponding equivalent circuit model. B. Evolution of the cation density near the anode during the early stage of charging ($\varphi_s = -10$). C. The decay of the surface charge at different applied potentials. In all cases, the reduced temperature is $l_B/\sigma = 1.834$, and the reduced bulk ion concentration is $\rho_0\sigma^3 = 0.125$. Reproduced with permission from ref 260. Copyright 2014 IOP Publishing (United Kingdom).

dynamic quantities, is characterized by contributions from an infinite number of exponential terms with different successive relaxation times. The leading term corresponds to the long-time decay of the charging dynamics and has a relaxation time of[264]

$$\tau_1 = \begin{cases} \frac{L\lambda}{D}[1 + O(\lambda/L)] & \text{if } L/\lambda \gg 1 \\ \frac{4L^2}{\pi^2 D}[1 + O(L^2/\lambda^2)] & \text{if } L/\lambda \ll 1 \end{cases} \quad (73)$$

Eq 73 suggests that the EC model is valid only when the cell width L is much larger than the Debye length λ. In the opposite limit, i.e., when the distance between the two electrodes is much smaller than the Debye length, the ion concentration is almost uniform so that the charging dynamics is dictated by ion diffusion as predicted by the single pore model (eq 69). The relaxation time predicted by eq 73 agrees well with lattice Boltzmann electrokinetics (LBE) simulations that account for both solvent and ion dynamics. The good agreement affirms that, at dilute conditions, neither thermodynamic nor transport nonideality is insignificant for the EDL charging under a weak applied potential.[270]

4.4.3. Conducting-Polymer Supercapacitors. For EDL charging at a finite applied potential, analytical solutions of the PNP equations exist only for a few limiting cases.[299] In general, the PNP equations need to be solved numerically even for dilute systems.[300] Toward that end, the literature is vast. The PNP equations have been routinely applied to ion transport in biological, environmental, colloidal, and electrochemical systems and beyond.

Figure 22 illustrates a recent example for modeling the cyclic voltammograms (CVs) and self-discharging potentials of conducting polymer supercapacitors.[301] With the point-charge model for holes in the conducting polymer and ionic species in an ionic liquid and with the assumption of a constant volumetric capacitance at the electrode−electrolyte interface, the PNP equations were able to describe diverse experimental data including the charging dynamics of supercapacitors and self-discharging characteristics and impedance spectroscopy. The impressive performance is probably not simply due to the adoption of adjustable parameters or cancellation of errors. The charge carriers of the polymer electrode (viz., holes) are essentially point charges as assumed by the PB equation. Furthermore, an ionic liquid may be described as a dilute electrolyte due to the strong association between cations and anions.[302] These factors may explain the excellent performance of the PNP equations for representing the charging behavior of conducting polymers in an ionic liquid. Successful application of the PNP equations was also reported for describing the dynamic behavior of the electric potential and charge densities of graphene oxide membranes.[303]

4.4.4. EDL Charging at Finite Ion Concentrations. As mentioned above, thermodynamic nonideality can be readily incorporated into the PNP equations. With the local excess chemical represented by one of the equilibrium models for inhomogeneous ionic systems, the MPNP equations (viz., TDDFT) can be used to examine the charging dynamics at large surface potentials and finite electrolyte concentrations.[304−307]

To illustrate, Figure 23 shows evolutions of the local counterion density and surface charge density for the same parallel-electrodes system but with the electrolyte solution represented by the primitive model. Even with a relatively simple expression for the excess chemical potential, analytical solutions are no more attainable.[308] Nevertheless, the relaxation time may be estimated from numerical results with the assumption of exponential decays (Figure 23). While the dilute-solution theory predicts that the relaxation time is independent of the applied potential, TDDFT calculations indicate a reduction of the charging time as the surface potential increases.[260] A monotonic decrease of the response time is expected because a higher electrode voltage results in a stronger electric field thereby accelerating ionic motions. Interestingly, TDDFT predicts that the relaxation time depends on the electrolyte concentration nonmonotonically at large applied potentials. Unlike that predicted by the EC model, the response time first rises as the electrolyte concentration increases and falls at large ion concentration due to the reduction in the EDL thickness.

TDDFT was also used to investigate ion flux in response to an AC voltage on a symmetric binary electrolyte confined between two parallel plates.[309] It predicts the dynamical layering of the ions near the confining walls and coherent motion of condensed ions in response to variation of the electrical field. The resonance effect was attributed to the field-induced ion condensation at the capacitor plates.

https://doi.org/10.1021/acs.chemrev.2c00097
Chem. Rev. XXXX, XXX, XXX−XXX

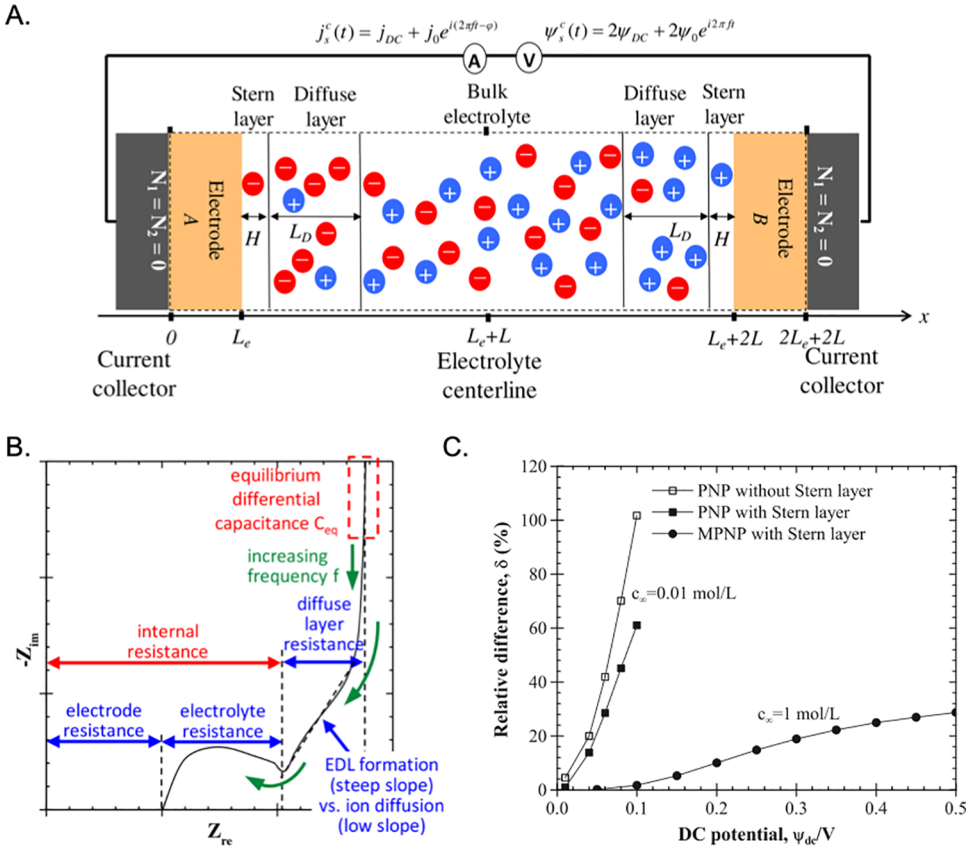

Figure 24. A. Schematic of an EDL cell simulated with the MPNP equations. B. Physical interpretations of the Nyquist plot. C. Relative difference between EIS and double-layer capacitances, $\delta \equiv |C_{EIS} - C_d|/C_d$, versus the DC potential predicted by the PNP equations with or without a Stern layer at the bulk ion concentration c_∞ = 0.01 mol/L and by the MPNP equations with a Stern layer at bulk ion concentration c_∞ = 1 mol/L. The Stern layer thickness is 0.33 nm, and ion diffusivity $D = 2 \times 10^{-9}$ m^2/s. (A and B) Reproduced from ref 313. Copyright 2018 American Chemical Society. (C) Reproduced with permission from ref 314. Copyright 2012 Elsevier.

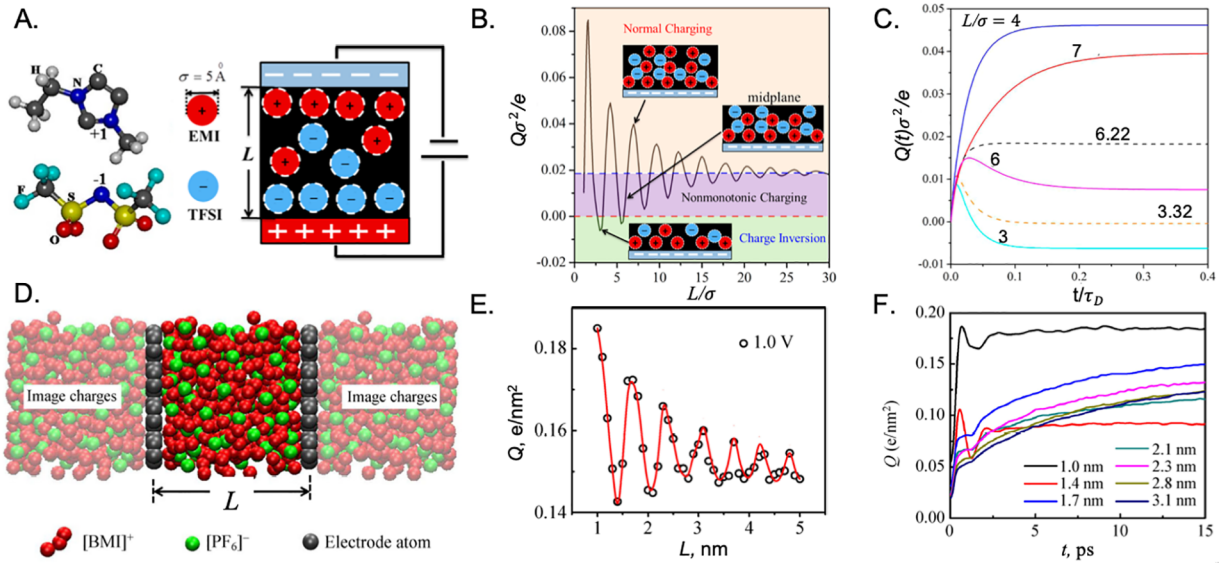

Figure 25. A. A model electrochemical cell for EDL charging in an ionic liquid. B. Equilibrium surface charge density versus the cell width predicted by cDFT. C. Evolution of surface charge density with time for different cell widths. D. A snapshot of the ionic distributions from MD simulation. E. The equilibrium surface charge density of the positive electrode versus the separation between the electrodes. F. The charging dynamics at different cell widths predicted by MD after the application of 1.0 V voltage bias. (A–C) Reproduced from ref 317. Copyright 2014 American Chemical Society. (D–F) Reproduced with permission from ref 320. Copyright 2015 Springer Science+Business Media.

4.4.5. Physical Interpretation of Electrochemical Techniques. Pilon and co-workers reported that the modified PNP (MPNP) equations were able to reproduce the basic features of EDL charging as typically characterized by various

https://doi.org/10.1021/acs.chemrev.2c00097
Chem. Rev. XXXX, XXX, XXX−XXX

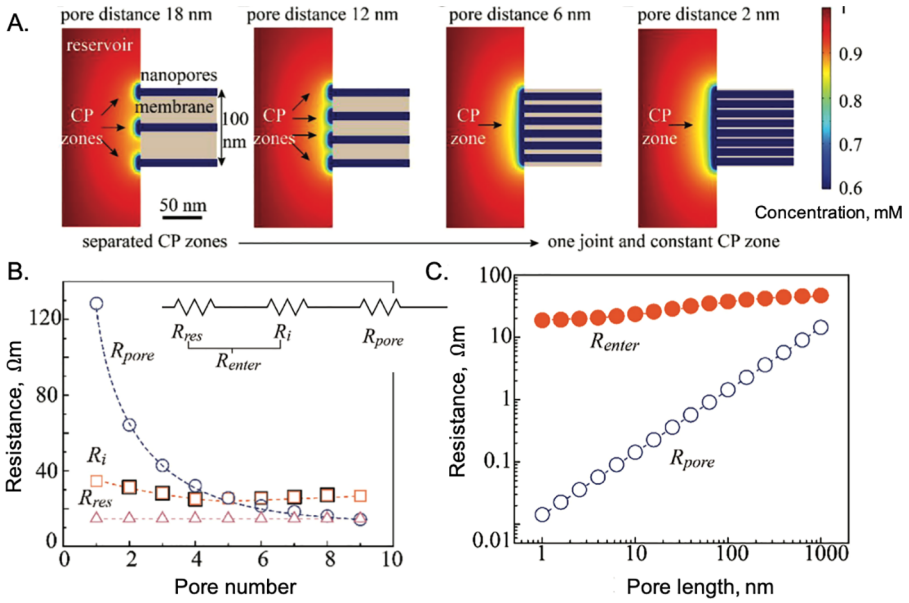

Figure 26. Entrance effects on ion transport in nanopores. A. The anion concentration predicted by the PNP equations shows the convergence of concentration polarization (CP) zones as the interpore distance falls. B. The reservoir resistance (R_{res}), interfacial resistance (R_i), and pore resistance (R_{pore}) versus the number of slit pores of 10 nm in width and 0.5 μm in length. C. The pore length effect on resistance. Reproduced with permission from ref 321. Copyright 2019 Wiley-VCH.

electrochemical analyses.[310] Figure 24 presents the typical computational setup to represent an EDL cell. One essential input for the one-dimensional description of charging dynamics is the local ionic conductivity

$$K(x) = D\left[\frac{Z^2e^2}{k_BT}\rho_s + \frac{\partial q}{\partial \psi} + \frac{\sigma^3(\rho_+ - \rho_-)}{1 - \rho_s\sigma^3}\frac{\partial \rho_s}{\partial \psi}\right] \quad (74)$$

The above equation can be derived from eq 52 after the correction of nonideality due to ion size with the lattice-gas model.[308] Without the electrical potential ψ, eq 74 is reduced to the electrical conductivity of a dilute solution, $K_0 = 2Z^2e^2D\rho_0/k_BT$. Eq 74 was extended to asymmetric electrolyte mixtures that accounts for differences in ion size and diffusivity[311] and to carbon electrodes with three-dimensional ordered structures.[312]

In combination with Ohm's law for the electrodes and electrolyte, the MPNP equations were used to describe electrochemical impedance spectroscopy (EIS), cyclic voltammetry (CV), and galvanostatic cycling (GC).[310] Although a direct comparison with experimental data is not feasible due to the simplicity of the model, the numerical results provide useful insight into various experimental quantities that are conventionally interpreted only from macroscopic perspectives. For example, Figure 24B and C illustrates the physical meanings of a typical Nyquist plot interpreted according to the EDL model and a comparison of the EIS and equilibrium capacitances predicted by the same model. One rather unexpected discovery was that EIS measurements systematically overestimated the EDL capacitance for dilute electrolyte solutions while underestimating it for concentrated electrolyte solutions subject to large electric potential.[313] The physics-based numerical simulations helped identify the intrinsic limitations of EIS measurements and settled down a long-time controversy on the origin of the discrepancy between EIS and equilibrium capacitances.

4.4.6. EDL Charging in Ionic Liquids. A number of theoretical studies have been devoted to the charging dynamics of electrochemical cells containing concentrated electrolytes or ionic liquids.[85,315−319] A conventional approach is to use the TDDFT or MPNP equations to account for the excess chemical potential. For example, Figure 25 shows the evolution of the surface charge predicted by TDDFT for a model ionic liquid confined between two parallel electrodes.[317] The oscillatory dependence of the equilibrium surface charge with the cell thickness is expected from the long-range layer-by-layer distributions of cations and anions and accords with MD simulations.[320] However, upon the application of a voltage between the two electrodes, the time evolution of the surface charge predicted by TDDFT is noticeably different from that observed in simulation.

As shown in Figure 25, TDDFT predicts three charging schemes corresponding to normal, oscillatory, and charge inversion that may emerge at equilibrium conditions. However, such schemes were less evident from MD simulation.[320] Nevertheless, neither TDDFT and MD yield an exponential decay of the charging curve as predicted by dilute solution models. The charging dynamics was also investigated with the MPNP equation based on the BSK theory of ionic liquids.[85,318,319] Interestingly, the nonmonotonic variation of the surface charge density versus time was predicted only after a semiempirical mobility matrix was incorporated into the electrodiffusion equation (viz., eq 46)

$$\mathbf{j}_i = -\upsilon_i\rho_i(1 - \rho_s a^3)\nabla\mu_i \quad (75)$$

where a is the lattice spacing in the BSK theory. In essence, the extra term on the right side of eq 75, $(1 - \rho_s a^3)$, accounts for the effect of free space on ion mobility ensuring the disappearance of diffusion at high densities. While the mean-field correction leads to the overcharging at a short-time scale reminiscent of that shown in Figure 25F, the nonmontonic evolutions of the surface charge density predicted by theory and MD simulation are distinctively different. In particular, the continuous theories do not capture the pronounced oscillation of the surface charge density during the initial stage of charging.

https://doi.org/10.1021/acs.chemrev.2c00097
Chem. Rev. XXXX, XXX, XXX−XXX

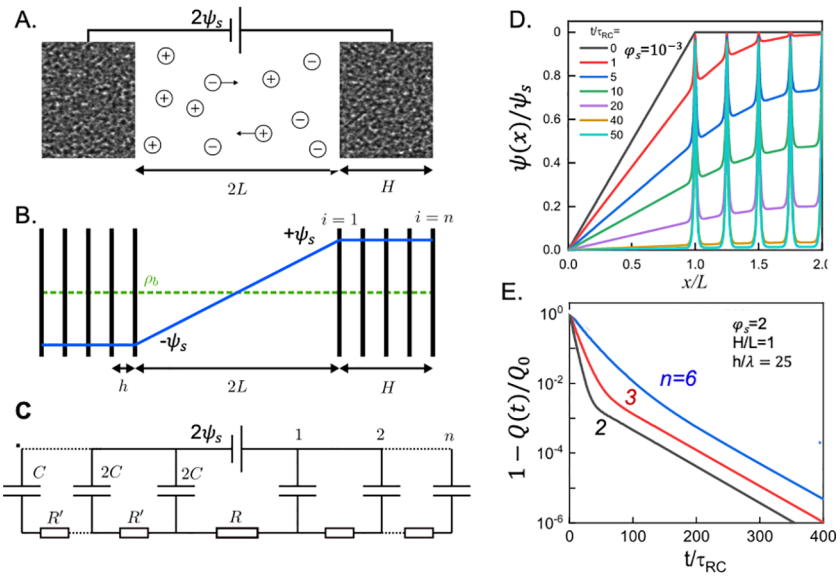

Figure 27. A. Schematic of two porous electrodes separated by a stagnant diffusion layer of length 2L. B. Each electrode is represented by parallel metallic sheets of equal separation (h). C. The transmission line (TL) model. D. The evolution of the reduced electrical potential at a small applied voltage ($10^{-3}k_BT/e$) and low electrolyte concentration (λ = 2.5 μm). E. The evolution of the total charge at a large applied voltage (ψ_s = $2k_BT/e$). Reproduced with permission from ref 323. Copyright 2020 American Physical Society.

4.5. Capturing the Microstructure of Porous Electrodes

Neither single-pore analysis nor the parallel-wall model accounts for the microscopic structure of porous electrodes. In practice, the electrodes are mostly amorphous with irregular, interconnected pores varying from atomic to macroscopic scales. Such effects can be incorporated by considering the pore size/shape distributions and network connectivity. Alternatively, idealized porous structures can be constructed to capture the overall effects on how the microscopic structure of a porous electrode affects ion transport and charging dynamics.

4.5.1. Pore-Orifice Effects. One common practice in extending the single-pore model to porous electrodes is by adding a static diffusion layer (SDL) at the entrance of individual pores.[286,288] In the limit of the thin double layer inside the pore (viz., the pore size much larger than the Debye length λ), the transition region between SDL and the pore orifice is often neglected such that it is electrically neutral and has an ion concentration the same as that in the bulk.[274] In the overlapping double-layer limit (viz., small pores), the transition region contributes to the changes in the electric potential and charge density over a length scale comparable to the pore size. In this case, the PNP equations may be solved by modifying the boundary conditions.[285]

Gao et al. investigated the entrance effects on ion transport through a single nanopore and multiple parallel pores by numerically solving the two-dimensional PNP equations.[321] As shown in Figure 26A, the concentration polarization (CP) zone near the entrance converges into a joint transition region when the interpore distance becomes comparable with the pore width. While the pore resistance is linearly dependent on the pore length and reduced proportionally as the number of pores increases, the entrance resistance (R_{ent}) is relatively insensitive to the pore length and number density and eventually dominates the ion transport when the number of parallel nanopores is sufficiently large (Figure 26B and C). The dominance of the entering resistance explains the exceptional electrochemical properties of supercapacitor electrodes composed of granular carbide-derived carbon (CDC) particles reported by Dyatkin et al.[322] Although larger CDC granules have longer micropores, they offer more micropore surface areas and reduce the electrode resistance. As a result, the electrodes made of larger CDC particles yield higher EDL capacitance and lower resistivity than those composed of smaller, milled particles. It should be noted that the physics underlying electrode charging is very different from ion transport through parallel channels as shown in Figure 26. While the former is affiliated with EDL formation, the latter is driven by thermodynamic forces due to the difference in certain potentials at the two ends of each channel (e.g., electric field, pressure, or concentration gradients). Nevertheless, the entrance effects are expected to be important in both cases. Because electrode charging is noticeably different from ion transport through parallel channels, it would be interesting to examine such an effect on the dynamics of multipore charging directly.

4.5.2. Stack-Electrode Model. To introduce the effects of pore structure on the charging behavior, Lian et al.[323] proposed an electrode model containing many parallel metallic sheets of equal separation (h). These sheets are permeable to ion diffusion and allow for the simultaneous application of an electrical potential. As shown in Figure 27, the so-called stacked-electrode model is equivalent to the TL model for a straight pore in a dilute solution with a relaxation time scale of[278]

$$\tau_{TLM} = (2 + 2H/3L)\frac{n\lambda L}{D} \tag{76}$$

where parameters n, H, and L are the number of parallel sheets per electrode, the electrode thickness, and the length of a stagnant diffusion layer before each electrode, respectively. Numerical results from the linearized PNP equations corroborate eq 76 for potentiostatic charging at a small voltage. At large voltages, however, the charge density exhibits a biexponential decay (Figure 27E) with the relaxation at the early time dictated by τ_{TLM} and the late time dictated by ion diffusion

$$\tau_{ad} = \alpha(L + H)^2/D \tag{77}$$

https://doi.org/10.1021/acs.chemrev.2c00097
Chem. Rev. XXXX, XXX, XXX−XXX

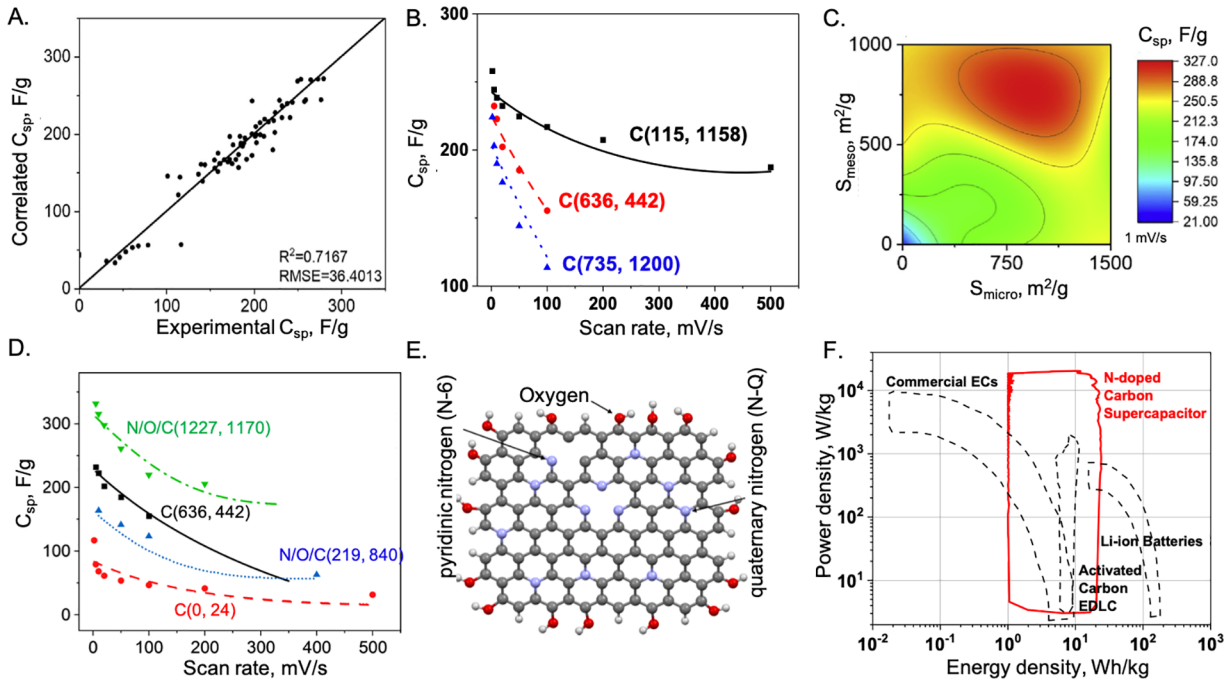

Figure 28. A. Correlation of experimental data with an artificial neural network (ANN) for the specific capacitance of activated carbons in a 6 M KOH aqueous solution. B. ANN prediction of specific capacitance versus the scan rate (lines) in comparison with experimental data (symbols). The numbers in the parentheses denote micro- and meso-pore specific surface areas in the units of m^2/g. C. Specific capacitance versus the surface areas of micropores and mesopores predicted by ANN. D. The same as B but for N/O codoped carbons with different surface compositions. E. The optimized structure of a N/O codoped carbon electrode predicted by the ANN model. F. Ragone plot for supercapacitors made of N/O codoped carbon electrodes. Reproduced from refs 328 and 329. Copyright 2020 American Chemical Society.

where parameter $\alpha \sim 0.1$ can be empirically correlated with h/λ. The two time scales differ by orders of magnitude for thin electrodes but become similar when the number of layers is large as for the case of supercapacitors. Conceptually, they may be affiliated with EDL formation and ion diffusion as discussed earlier for the charging behavior of a single pore, i.e., $2n\lambda L/D$ represents the time scale of EDL charging for $2n$ parallel pores (cathode and anode), and $(L + H)^2/D$ corresponds to the time scale of ion diffusion.

In comparison with the single-pore model, one advantage of the stack-electrode model is that it involves only 1D calculations of the charge density and ionic density profiles. The numerical simplicity allows for TDDFT calculations to account for thermodynamic nonideality and faradaic reactions that may be explored in the future work.

4.5.3. Machine Learning. Whereas pore-network models for describing ion transport in porous media have been well established,[324] understanding the influence of the hierarchical pore structure on charging dynamics from a molecular perspective is particularly challenging because of the system size and microscopic irregularities. On the one hand, the structure of porous electrodes is typically characterized with gas-adsorption experiments based on the simple models of pore shape and size distributions. Whereas the procedure is adequate to estimate the porosity and specific surface area, it offers little information on pore connectivity and the interactions of charge carriers with the porous material that are essential for understanding the dynamic behavior of practical electrochemical systems. On the other hand, the physical behavior of an ionic fluid in porous electrodes is fundamentally different from that of gas molecules. Although realistic porous models have been constructed by mimicking materials synthesis or the morphological structure from experiments, the nanoscale structure may not be representative of the hierarchical structure of a macroscopic electrode.

Several theoretical investigations have been reported to understand the influence of electrode structure on charging dynamics.[325] For example, Sakaguchi and Baba proposed fractal models to mimic the porous structures of various activated carbons and investigated their influences on the charging behavior by solving the two-dimensional PNP equations.[276,326] The numerical results suggest power-law variations of the relaxation time as a function of the system size, temperature, and ion concentration. The exponent was found consistent with the fractional dimension for the porous media. Wang and Pilon constructed 3D model electrodes consisting of closely packed monodispersed mesoporous carbon spheres.[312,327] The 3D models were able to describe gravimetric capacitances of carbon electrodes in good agreement with experimental data.

For realistic electrodes, uncertainties in the microscopic structure are virtually unavoidable, and their practical use mostly hinges on dynamic processes at conditions far from equilibrium. To quantify the charging behavior and off-equilibrium properties of EDL as typically measured in experiments, machine learning (ML) methods become an attractive alternative to physics-based modeling. For example, the artificial neural network (ANN) was used to correlate the electrochemical performance of supercapacitors in terms of the scan rate and various characterizations of carbon electrodes including micropore and mesopore specific surface areas and the extent of heteroatom doping (Figure 28).[328,329] The ML model is able to account for the synergistic effects of nitrogen and oxygen doping and identify the structural features of carbon electrodes that lead to higher energy and power density. Excellent reviews are

https://doi.org/10.1021/acs.chemrev.2c00097
Chem. Rev. XXXX, XXX, XXX−XXX

available on applications of ML methods to quantify the performance of energy storage devices.[330,331]

5. CONCLUSIONS

In a landmark publication on EDL modeling,[74] Kornyshev remarked "In a democratic society, you can model anything the way you want, but will your model be close to reality?". As discussed in the present review, EDL models are diverse and numerous, ranging from various modifications of the PB equation, lattice-gas models, Ising models, and all sorts of cDFT methods to first-principles approaches such as joint-DFT and various grand-canonical methods. In principle, the equilibrium models can be extended to describe time-dependent phenomena by combination with transport equations with or without considering kinetic correlations. Moreover, machine-learning (ML) methods can be trained as a surrogate of physics-based models when extensive data are available. As myriad chemical events may take place at the electrode−electrolyte interface or within the micropores of an electrode, every EDL model reflects certain aspects of reality. From a practical perspective, simple−particularly analytical−models are valuable to attain physical insights and gain qualitative understanding. However, more sophisticated models are necessary in order to describe the rich behavior of EDL under realistic conditions. For materials discovery and device optimization, we desire quantitative models that are physically sound, computationally efficient, and numerically reliable over a broad range of parameter space and operation conditions. As of today, an EDL model accounting for all aspects the microscopic structure and dynamics is yet to be developed. Nevertheless, very often even simple models, such as the PNP equations or analytical results obtained after further approximations, might find applications to seemingly complicated systems such as supercapacitors consisting of conducting polymers or ionic liquids.

In this review, we have analyzed recent theoretical developments for describing the nonclassical EDL structure and charging behavior such as oscillatory ion distributions, interfacial phase transitions, and nonlocal charge transfer. We have also discussed the key hypotheses of various EDL models and elucidated their applications in the context of capacitive energy storage. While a direct comparison of different models is hard to make because they vary in scope and complexity, we offered an analysis of their similarities, advantages, and limitations in representing thermodynamic nonideality owing to intermolecular interactions and correlation effects. In particular, a special effort has been made to connect recent theoretical developments with the macroscopic models of electrochemical systems that remain popular in engineering applications.

Looking into the future, we anticipate further developments of first-principles methods to describe the electrodes and electrolytes on an equal footing. While impressive progress has already been made in this direction, there are still major obstacles to treat interactions between electrons and ionic species in a nonempirical way. Many existing methods describe the electronic properties by quantum-mechanical calculations but electrolyte/solvent effects with classical models. While the hybrid approach is computationally efficient for understanding the qualitative behavior of the EDL structure and surface reactions, the numerical performance is often unsatisfactory even for relatively simple systems such as metal electrodes in contact with a dilute solution. Besides, the hybrid approach is problematic for describing charge transfer between an electrode and chemical species in the surrounding electrolyte.[246] In particular, electrochemical energy storage mostly deals with porous electrodes and concentrated electrolytes that are beyond the applicability of continuous solvent models or dilute solution theories.[49] The integration of quantum and classical equations has inherent limitations due to the incompatibility of quantum and classical theoretical frameworks (e.g., electrons do not interact with the Lennard-Jones particles). A fully quantum-mechanical approach is thus necessary in order to account for the electronic structure of all components in the EDL, which encompasses atomic species from both the electrolyte and electrode. Recent *ab initio* MD simulations have demonstrated such capabilities, but their applications to larger systems will probably require the adoption of ML force fields, which are still at the early stage of development.[332] Alternatively, the quantum/quantum embedding methods are promising to treat the electronic structure and solution conditions in a self-consistent manner. In comparison with brute-force quantum-mechanical calculations, the embedding methods reduce the computational cost by employing a lower level of quantum methods for the thermodynamic environment. Toward that end, the development of an accurate description of the interactions between subquantum systems will be a fruitful area for future theoretical research. The all-first-principles approach will enable not only a faithful description of the EDL structure with atomic details but also quantitative predictions of charge transfer and other electrochemical activities underpinning energy storage and chemical conversion.

In comparison with the equilibrium properties of EDL, the dynamic behavior underlying energy storage and charge transfer remains much less understood. Because of the complexity of porous electrodes, the single-pore analysis is often insufficient to describe ion transport and surface reactions relevant to realistic electrochemical devices. Besides, one may question the applicability of the primitive model or dilute solution theories such as PNP equations to charge transfer and ion transport in micropores. Furthermore, reliable theoretical tools are yet to be developed to describe the coupled effects of quantum and classical dynamics for electrochemical systems at off-equilibrium conditions. For these reasons, we expect further applications of ML methods to correlate the performance of electrochemical systems with materials characteristics and operation conditions. The electrokinetic behavior of realistic electrodes depends on a large number of highly nonlinear processes ranging from EDL formation, ionic motions, and surface reactions to charging/discharging of macroscopic devices and materials aging and degradation. As the parameter space for electrodes and electrolytes is vast, investigating every combination of parameters is inefficient from either computational or experimental perspectives. As a valuable alternative to the physics-based modeling, data-driven methods are useful not only for capturing the intrinsic properties of electrodes (e.g., pore architecture, surface chemistry, and pore-size distribution) as well as electrolytes (e.g., ionic structure and chemical composition) but also for predicting the EDL performance in terms of both equilibrium and dynamic measures. With sufficient training data from experiments and/or theoretical predictions, the combination of physics-based models and ML methods will be able to extract quantitative relationships between input and output variables based on various neural networks or statistical algorithms. Without evoking the physical details of experimental systems and thermodynamic conditions, the data-driven approach will allow for the correlation of the

https://doi.org/10.1021/acs.chemrev.2c00097
Chem. Rev. XXXX, XXX, XXX−XXX

EDL behavior with the properties of materials even at conditions far away from equilibrium.

AUTHOR INFORMATION

Corresponding Author

Jianzhong Wu − *Department of Chemical and Environmental Engineering, University of California, Riverside, California 92521, United States;* orcid.org/0000-0002-4582-5941; Phone: +001 (1) 951 827 2413; Email: jwu@engr.ucr.edu; Fax: +001 (1) 951 827 5696

Complete contact information is available at: https://pubs.acs.org/10.1021/acs.chemrev.2c00097

Notes

The author declares no competing financial interest.

Biography

Jianzhong Wu received his Ph.D. in Chemical Engineering from the University of California, Berkeley, and M.S. and B.S. degrees from Tsinghua University, Beijing. He has been a faculty member at the University of California, Riverside, since 2001. His research is directed at development and application of statistical-mechanical methods for predicting the microscopic structure and physicochemical properties of inhomogeneous fluids, soft matter, and biological systems.

ACKNOWLEDGMENTS

This work was sponsored as part of the Fluid Interface Reactions, Structures and Transport (FIRST) Center, an Energy Frontier Research Center funded by the U.S. Department of Energy (DOE), Office of Basic Energy Sciences. The author's computational work used resources of the National Energy Research Scientific Computing Center (NERSC), a DOE Office of Science User Facility supported by the Office of Science of the U.S. Department of Energy, under Contract DE-AC02-05CH11231. The author thanks Dr. Cheng Lian and co-workers at ECUST for the impetus to prepare this review and researchers at the FIRST center for many years of productive collaboration.

REFERENCES

(1) Helmholtz, H. Ueber Einige Gesetze Der Vertheilung Elektrischer Ströme in Körperlichen Leitern Mit Anwendung Auf Die Thierisch-Elektrischen Versuche. *Ann. Phys.* **1853**, *165*, 211−233.

(2) Fleischmann, S.; Mitchell, J. B.; Wang, R.; Zhan, C.; Jiang, D.-e.; Presser, V.; Augustyn, V. Pseudocapacitance: From Fundamental Understanding to High Power Energy Storage Mater. *Chem. Rev.* **2020**, *120*, 6738−6782.

(3) Nitopi, S.; Bertheussen, E.; Scott, S. B.; Liu, X.; Engstfeld, A. K.; Horch, S.; Seger, B.; Stephens, I. E. L.; Chan, K.; Hahn, C.; Nørskov, J. K.; Jaramillo, T. F.; Chorkendorff, I. Progress and Perspectives of Electrochemical CO2 Reduction on Copper in Aqueous Electrolyte. *Chem. Rev.* **2019**, *119*, 7610−7672.

(4) Simon, P.; Gogotsi, Y. Perspectives for Electrochemical Capacitors and Related Devices. *Nat. Mater.* **2020**, *19*, 1151−1163.

(5) Yang, Z.; Zhang, J.; Kintner-Meyer, M. C. W.; Lu, X.; Choi, D.; Lemmon, J. P.; Liu, J. Electrochemical Energy Storage for Green Grid. *Chem. Rev.* **2011**, *111*, 3577−3613.

(6) Zhao, J.; Burke, A. F. Review on Supercapacitors: Technologies and Performance Evaluation. *J. Energy Chem.* **2021**, *59*, 276−291.

(7) Horn, M.; MacLeod, J.; Liu, M.; Webb, J.; Motta, N. Supercapacitors: A New Source of Power for Electric Cars? *Econ. Anal. Policy* **2019**, *61*, 93−103.

(8) Beguin, F.; Frackowiak, E. *Supercapacitors: Materials, Systems, and Applications; Materials for sustainable energy and development*; Wiley-VCH: Weinheim, 2013; pp xxviii, 569pp.

(9) Yu, A.; Chabot, V.; Zhang, J. *Electrochemical Supercapacitors for Energy Storage and Delivery: Fundamentals and Applications; Electrochemical Energy Storage and Conversion*; CRC Press: 2017; DOI: 10.1201/b14671.

(10) Brogioli, D. Extracting Renewable Energy From a Salinity Difference Using a Capacitor. *Phys. Rev. Lett.* **2009**, *103*, 058501.

(11) Gouy, M. On the Constitution of the Electric Charge at the Surface of an Electrolyte. *C. R. Acad. Sci.* **1909**, *149*, 654−657.

(12) Chapman, D. L. LI. A Contribution to the Theory of Electrocapillarity. *Philos. Mag.* **1913**, *25*, 475−481.

(13) Stern, O. Zur Theorie Der Elektrolytischen Doppelschicht. *Z. Elektrochem. Angew. Phys. Chem.* **1924**, *30*, 508−516.

(14) Wang, X.; Liu, K.; Wu, J. Demystifying the Stern Layer at a Metal−Electrolyte Interface: Local Dielectric Constant, Specific Ion Adsorption, and Partial Charge Transfer. *J. Chem. Phys.* **2021**, *154*, 124701.

(15) Grahame, D. C. The Electrical Double Layer and the Theory of Electrocapillarity. *Chem. Rev.* **1947**, *41*, 441−501.

(16) Li, C. K.; Huang, J. Impedance Response of Electrochemical Interfaces: Part I. Exact Analytical Expressions for Ideally Polarizable Electrodes. *J. Electrochem. Soc.* **2020**, *167*, 166517.

(17) Stillinger, F. H.; Kirkwood, J. G. Theory of the Diffuse Double Layer. *J. Chem. Phys.* **1960**, *33*, 1282−1290.

(18) Carnie, S. L.; Torrie, G. M. The Statistical-Mechanics of the Electrical Double-Layer. *Adv. Chem. Phys.* **2007**, *56*, 141−253.

(19) Attard, P. *Adv. Chem. Phys.*; John Wiley & Sons, Ltd.: 1996; Vol. *92*, Chapter 1, pp 1−159.

(20) Outhwaite, C. W.; Bhuiyan, L. B. On the Modified Poisson−Boltzmann Closure for Primitive Model Electrolytes at High Concentration. *J. Chem. Phys.* **2021**, *155*, 014504.

(21) Evans, R.; Sluckin, T. A Density Functional Theory for Inhomogeneous Charged Fluids. *Mol. Phys.* **1980**, *40*, 413−435.

(22) Petsev, D. N.; van Swol, F.; Frink, L. J. D. In *Molecular Theory of Electric Double Layers*; Petsev, D. N., van Swol, F., Frink, L. J. D., Eds.; 2053-2563; IOP Publishing: 2021; pp 7-1 to 7-65.

(23) Härtel, A. Structure of Electric Double Layers in Capacitive Systems and to What Extent (Classical) Density Functional Theory Describes It. *J. Phys.: Condens. Matter* **2017**, *29*, 423002.

(24) Forsman, J.; Woodward, C. E.; Szparaga, R. In *Computational Electrostatics for Biological Applications: Geometric and Numerical Approaches to the Description of Electrostatic Interaction Between Macromolecules*; Rocchia, W., Spagnuolo, M., Eds.; Springer International Publishing: Cham, 2015; pp 17−38, DOI: 10.1007/978-3-319-12211-3_2.

(25) Pizio, O.; Sokolowski, S. In *Solid State Electrochemistry II: Electrodes, Interfaces and Ceramic Membranes*; Kharton, V. V., Ed.; Wiley-VCH Verlag GmbH & Co. KGaA: 2011; pp 73−124, DOI: 10.1002/9783527635566.ch3.

(26) Rice, O. K. Application of the Fermi Statistics to the Distribution of Electrons Under Fields in Metals and the Theory of Electrocapillarity. *Phys. Rev.* **1928**, *31*, 1051−1059.

(27) Lang, N. D.; Kohn, W. Theory of Metal Surfaces: Charge Density and Surface Energy. *Phys. Rev. B* **1970**, *1*, 4555−4568.

(28) Lang, N. D.; Kohn, W. Theory of Metal Surfaces: Work Function. *Phys. Rev. B* **1971**, *3*, 1215−1223.

(29) Schmickler, W. Electronic Effects in the Electric Double Layer. *Chem. Rev.* **1996**, *96*, 3177−3200.

(30) Sakaushi, K.; Kumeda, T.; Hammes-Schiffer, S.; Melander, M. M.; Sugino, O. Advances and Challenges for Experiment and Theory for Multi-Electron Multi-Proton Transfer at Electrified Solid-Liquid Interfaces. *Phys. Chem. Chem. Phys.* **2020**, *22*, 19401−19442.

(31) Sundararaman, R.; Arias, T. A. *Atomic-Scale Modelling of Electrochemical Systems*; John Wiley & Sons, Ltd.: 2021; Chapter 4, pp 139−172, DOI: 10.1002/9781119605652.ch4.

(32) Groβ, A. Grand-Canonical Approaches to Understand Structures and Processes at Electrochemical Interfaces From an Atomistic Perspective. *Curr. Opin. Electrochem.* **2021**, *27*, 100684.
(33) Watts-tobin, R. J. The Interface Between a Metal and an Electrolytic Solution. *Philos. Mag.* **1961**, *6*, 133−153.
(34) Mott, N.; Watts-Tobin, R. The Interface Between a Metal and an Electrolyte. *Electrochim. Acta* **1961**, *4*, 79−107.
(35) Gonella, G.; Backus, E. H. G.; Nagata, Y.; Bonthuis, D. J.; Loche, P.; Schlaich, A.; Netz, R. R.; Kühnle, A.; McCrum, I. T.; Koper, M. T. M.; Wolf, M.; Winter, B.; Meijer, G.; Campen, R. K.; Bonn, M. Water at Charged Interfaces. *Nat. Rev. Chem.* **2021**, *5*, 466−485.
(36) Huang, J.; Malek, A.; Zhang, J.; Eikerling, M. H. Non-Monotonic Surface Charging Behavior of Platinum: A Paradigm Change. *J. Phys. Chem. C* **2016**, *120*, 13587−13595.
(37) Le, J.-B.; Fan, Q.-Y.; Li, J.-Q.; Cheng, J. Molecular Origin of Negative Component of Helmholtz Capacitance at Electrified Pt(111)/Water Interface. *Sci. Adv.* **2020**, *6*, No. eabb1219.
(38) Huang, J. Surface Charging Behaviors of Electrocatalytic Interfaces With Partially Charged Chemisorbates. *Curr. Opin. Electrochem.* **2022**, *33*, 100938.
(39) Lee, S. S.; Koishi, A.; Bourg, I. C.; Fenter, P. Ion Correlations Drive Charge Overscreening and Heterogeneous Nucleation at Solid ExtendashAqueous Electrolyte Interfaces. *Proc. Natl. Acad. Sci. U. S. A.* **2021**, *118*, e2105154118.
(40) Comtet, J.; Niguès, A.; Kaiser, V.; Coasne, B.; Bocquet, L.; Siria, A. Nanoscale Capillary Freezing of Ionic Liquids Confined Between Metallic Interfaces and the Role of Electronic Screening. *Nat. Mater.* **2017**, *16*, 634−639.
(41) Jeon, Y.; Vaknin, D.; Bu, W.; Sung, J.; Ouchi, Y.; Sung, W.; Kim, D. Surface Nanocrystallization of an Ionic Liquid. *Phys. Rev. Lett.* **2012**, *108*, 055502.
(42) Mezger, M.; Schröder, H.; Reichert, H.; Schramm, S.; Okasinski, J. S.; Schöder, S.; Honkimäki, V.; Deutsch, M.; Ocko, B. M.; Ralston, J.; Rohwerder, M.; Stratmann, M.; Dosch, H. Molecular Layering of Fluorinated Ionic Liquids at a Charged Sapphire (0001) Surface. *Science* **2008**, *322*, 424−428.
(43) Mao, X.; Brown, P.; Červinka, C.; Hazell, G.; Li, H.; Ren, Y.; Chen, D.; Atkin, R.; Eastoe, J.; Grillo, I.; Padua, A. A. H.; Costa Gomes, M. F.; Hatton, T. A. Self-Assembled Nanostructures in Ionic Liquids Facilitate Charge Storage at Electrified Interfaces. *Nat. Mater.* **2019**, *18*, 1350−1357.
(44) Kornyshev, A. A.; Qiao, R. Three-Dimensional Double Layers. *J. Phys. Chem. C* **2014**, *118*, 18285−18290.
(45) Bedanov, V. M.; Peeters, F. m. c. M. Ordering and Phase Transitions of Charged Particles in a Classical Finite Two-Dimensional System. *Phys. Rev. B* **1994**, *49*, 2667−2676.
(46) Schlaich, A.; Jin, D.; Bocquet, L.; Coasne, B. Electronic Screening Using a Virtual Thomas−Fermi Fluid for Predicting Wetting and Phase Transitions of Ionic Liquids at Metal Surfaces. *Nat. Mater.* **2022**, *21*, 237.
(47) Liu, K.; Wu, J. Wettability of Ultra-Small Pores of Carbon Electrodes by Size-Asymmetric Ionic Fluids. *J. Chem. Phys.* **2020**, *152*, 054708.
(48) Zhan, C.; Lian, C.; Zhang, Y.; Thompson, M. W.; Xie, Y.; Wu, J.; Kent, P. R. C.; Cummings, P. T.; Jiang, D.-e.; Wesolowski, D. J. Computational Insights into Materials and Interfaces for Capacitive Energy Storage. *Adv. Sci.* **2017**, *4*, 1700059.
(49) Wang, X.; Salari, M.; Jiang, D.-e.; Chapman Varela, J.; Anasori, B.; Wesolowski, D. J.; Dai, S.; Grinstaff, M. W.; Gogotsi, Y. Electrode Material-Ionic Liquid Coupling for Electrochemical Energy Storage. *Nat. Rev. Mater.* **2020**, *5*, 787−808.
(50) Shao, Y.; El-Kady, M. F.; Sun, J.; Li, Y.; Zhang, Q.; Zhu, M.; Wang, H.; Dunn, B.; Kaner, R. B. Design and Mechanisms of Asymmetric Supercapacitors. *Chem. Rev.* **2018**, *118*, 9233−9280.
(51) Scalfi, L.; Salanne, M.; Rotenberg, B. Molecular Simulation of Electrode-Solution Interfaces. *Annu. Rev. Phys. Chem.* **2021**, *72*, 189−212.
(52) Fedorov, M. V.; Kornyshev, A. A. Ionic Liquids at Electrified Interfaces. *Chem. Rev.* **2014**, *114*, 2978−3036.
(53) Jeanmairet, G.; Rotenberg, B.; Salanne, M. Microscopic Simulations of Electrochemical Double-Layer Capacitors. *Chem. Rev.* **2022**, DOI: 10.1021/acs.chemrev.1c00925.
(54) Newman, J. S.; Balsara, N. P. *Electrochemical Systems*, 4th ed. ed.; Wiley: Hoboken, NJ, 2019; 608pp.
(55) Schmickler, W.; Santos, E. *Interfacial Electrochemistry*, 2nd ed.; Springer: 2010; pp Heidelberg; New York, pp xiv, 272pp, DOI: 10.1007/978-3-642-04937-8.
(56) Bard, A. J.; Faulkner, L. R. *Electrochemical Methods: Fundamentals and Applications*, 2nd ed.; Wiley: New York, 2001; pp xxi, 833pp.
(57) Damaskin, B. B.; Petrii, O. A. Historical Development of Theories of the Electrochemical Double Layer. *J. Solid State Electrochem.* **2011**, *15*, 1317−1334.
(58) Bedrov, D.; Piquemal, J.-P.; Borodin, O.; MacKerell, A. D.; Roux, B.; Schröder, C. Molecular Dynamics Simulations of Ionic Liquids and Electrolytes Using Polarizable Force Fields. *Chem. Rev.* **2019**, *119*, 7940−7995.
(59) Wang, Z.-G. In *Variational Methods in Molecular Modeling*; Wu, J., Ed.; Springer Singapore: Singapore, 2017; pp 1−29, DOI: 10.1007/978-981-10-2502-0_1.
(60) Fawcett, W. R. Monte Carlo Studies of Ion Size Effects in the Diffuse Double Layer. *Electrochim. Acta* **2009**, *54*, 4997−5005.
(61) Ojha, K.; Doblhoff-Dier, K.; Koper, M. T. M. Double-Layer Structure of the Pt(111) ExtendashAqueous Electrolyte Interface. *Proc. Natl. Acad. Sci. U. S. A.* **2022**, *119*, e2116016119.
(62) Su, M.; Wang, Y. T. A Brief Review of Continuous Models for Ionic Solutions: The Poisson-Boltzmann and Related Theories. *Commun. Theor. Phys.* **2020**, *72*, 067601.
(63) Naji, A.; Kanduč, M.; Forsman, J.; Podgornik, R. Perspective: Coulomb Fluids—Weak Coupling, Strong Coupling, in Between and Beyond. *J. Chem. Phys.* **2013**, *139*, 150901.
(64) Doblhoff-Dier, K.; Koper, M. T. M. Modeling the Gouy−Chapman Diffuse Capacitance With Attractive Ion−Surface Interaction. *J. Phys. Chem. C* **2021**, *125*, 16664−16673.
(65) Shin, S.-J.; Kim, D. H.; Bae, G.; Ringe, S.; Choi, H.; Lim, H.-K.; Choi, C. H.; Kim, H. On the Importance of the Electric Double Layer Structure in Aqueous Electrocatalysis. *Nat. Commun.* **2022**, *13*, 174.
(66) Park, Y. S.; Kang, I. S. Multi-Ionic Effects on the Equilibrium and Dynamic Properties of Electric Double Layers Based on the Bikerman Correction. *J. Electroanal. Chem.* **2021**, *880*, 114923.
(67) May, S. Differential Capacitance of the Electric Double Layer: Mean-Field Modeling Approaches. *Curr. Opin. Electrochem.* **2019**, *13*, 125−131.
(68) Antypov, D.; Barbosa, M. C.; Holm, C. Incorporation of Excluded-Volume Correlations Into Poisson-Boltzmann Theory. *Phys. Rev. E* **2005**, *71*, 061106.
(69) Bikerman, J. XXXIX. Structure and Capacity of Electrical Double Layer. *Philos. Mag.* **1942**, *33*, 384−397.
(70) Bazant, M. Z.; Kilic, M. S.; Storey, B. D.; Ajdari, A. Towards an Understanding of Induced-Charge Electrokinetics at Large Applied Voltages in Concentrated Solutions. *Adv. Colloid Interface Sci.* **2009**, *152*, 48−88.
(71) Henderson, D.; Boda, D. Insights From Theory and Simulation on the Electrical Double Layer. *Phys. Chem. Chem. Phys.* **2009**, *11*, 3822−3830.
(72) Petsev, D. N.; van Swol, F.; Frink, L. J. D. *Molecular Theory of Electric Double Layers*; 2053-2563; IOP Publishing: 2021.
(73) Goodwin, Z. A. H.; de Souza, J. P.; Bazant, M. Z.; Kornyshev, A. A. In *Encyclopedia of Ionic Liquids*; Zhang, S., Ed.; Springer Singapore: Singapore, 2021; pp 1−13.
(74) Kornyshev, A. A. Double-Layer in Ionic Liquids: Paradigm Change? *J. Phys. Chem. B* **2007**, *111*, 5545−5557.
(75) Kilic, M. S.; Bazant, M. Z.; Ajdari, A. Steric Effects in the Dynamics of Electrolytes at Large Applied Voltages. I. Double-Layer Charging. *Phys. Rev. E* **2007**, *75*, 021502.
(76) Borukhov, I.; Andelman, D.; Orland, H. Adsorption of Large Ions From an Electrolyte Solution: A Modified Poisson-Boltzmann Equation. *Electrochim. Acta* **2000**, *46*, 221−229.

https://doi.org/10.1021/acs.chemrev.2c00097
Chem. Rev. XXXX, XXX, XXX−XXX

(77) Oldham, K. B. A. Gouy−Chapman−Stern Model of the Double Layer at a (Metal)/(Ionic Liquid) Interface. *J. Electroanal. Chem.* **2008**, *613*, 131−138.
(78) Freise, V. Zur Theorie der diffusen Doppelschicht. *Z. Elektrochem* **1952**, *56*, 822−827.
(79) Wu, J.; Jiang, T.; Jiang, D.-e.; Jin, Z.; Henderson, D. A classical density functional theory for interfacial layering of ionic liquids. *Soft Matter* **2011**, *7*, 11222−11231.
(80) Jiang, D.-e.; Meng, D.; Wu, J. Density Functional Theory for Differential Capacitance of Planar Electric Double Layers in Ionic Liquids. *Chem. Phys. Lett.* **2011**, *504*, 153−158.
(81) Mezger, M.; Roth, R.; Schröder, H.; Reichert, P.; Pontoni, D.; Reichert, H. Solid-Liquid Interfaces of Ionic Liquid Solutions—Interfacial Layering and Bulk Correlations. *J. Chem. Phys.* **2015**, *142*, 164707.
(82) Bazant, M. Z.; Storey, B. D.; Kornyshev, A. A. Double Layer in Ionic Liquids: Overscreening Versus Crowding. *Phys. Rev. Lett.* **2011**, *106*, 046102.
(83) de Souza, J. P.; Bazant, M. Z. Continuum Theory of Electrostatic Correlations at Charged Surfaces. *J. Phys. Chem. C* **2020**, *124*, 11414−11421.
(84) Santangelo, C. D. Computing Counterion Densities at Intermediate Coupling. *Phys. Rev. E* **2006**, *73*, 041512.
(85) Lee, A. A.; Kondrat, S.; Vella, D.; Goriely, A. Dynamics of Ion Transport in Ionic Liquids. *Phys. Rev. Lett.* **2015**, *115*, 106101.
(86) Chao, H.; Wang, Z.-G. Effects of Surface Transition and Adsorption on Ionic Liquid Capacitors. *J. Phys. Chem. Lett.* **2020**, *11*, 1767−1772.
(87) Maggs, A. C.; Podgornik, R. General theory of asymmetric steric interactions in electrostatic double layers. *Soft Matter* **2016**, *12*, 1219−1229.
(88) Podgornik, R. General Theory of Charge Regulation and Surface Differential Capacitance. *J. Chem. Phys.* **2018**, *149*, 104701.
(89) Zhang, Y.; Huang, J. Treatment of Ion-Size Asymmetry in Lattice-Gas Models for Electrical Double Layer. *J. Phys. Chem. C* **2018**, *122*, 28652−28664.
(90) de Souza, J. P.; Goodwin, Z. A. H.; McEldrew, M.; Kornyshev, A. A.; Bazant, M. Z. Interfacial Layering in the Electric Double Layer of Ionic Liquids. *Phys. Rev. Lett.* **2020**, *125*, 116001.
(91) Avni, Y.; Adar, R. M.; Andelman, D. Charge Oscillations in Ionic Liquids: A Microscopic Cluster Model. *Phys. Rev. E* **2020**, *101*, 010601.
(92) Budkov, Y. A.; Zavarzin, S. V.; Kolesnikov, A. L. Theory of Ionic Liquids With Polarizable Ions on a Charged Electrode. *J. Phys. Chem. C* **2021**, *125*, 21151−21159.
(93) Gupta, A.; Govind Rajan, A.; Carter, E. A.; Stone, H. A. Ionic Layering and Overcharging in Electrical Double Layers in a Poisson-Boltzmann Model. *Phys. Rev. Lett.* **2020**, *125*, 188004.
(94) Vatamanu, J.; Borodin, O.; Smith, G. D. Molecular Simulations of the Electric Double Layer Structure, Differential Capacitance, and Charging Kinetics for N-Methyl-N-Propylpyrrolidinium Bis-(Fluorosulfonyl)Imide at Graphite Electrodes. *J. Phys. Chem. B* **2011**, *115*, 3073−3084.
(95) Evans, R. The Nature of the Liquid-Vapour Interface and Other Topics in the Statistical Mechanics of Non-Uniform, Classical Fluids. *Adv. Phys.* **1979**, *28*, 143−200.
(96) Hansen, J.-P.; McDonald, I. R. *Theory of Simple Liquids: With Applications of Soft Matter*, 4th ed.; Elsevier/AP: Amstersdam, 2013; pp xv, 619pp.
(97) Roth, R. Fundamental Measure Theory for Hard-Sphere Mixtures: A Review. *J. Phys.: Condens. Matter* **2010**, *22*, 063102.
(98) Lutsko, J. F. *Adv. Chem. Phys.*; John Wiley & Sons, Ltd.: 2010; Chapter 1, pp 1−92, DOI: 10.1002/9780470564318.ch1.
(99) Wu, J. In *Variational Methods in Molecular Modeling*; Wu, J., Ed.; Springer Singapore: Singapore, 2017; pp 65−99, DOI: 10.1007/978-981-10-2502-0_3.
(100) Borgis, D.; Luukkonen, S.; Belloni, L.; Jeanmairet, G. Accurate Prediction of Hydration Free Energies and Solvation Structures Using Molecular Density Functional Theory With a Simple Bridge Functional. *J. Chem. Phys.* **2021**, *155*, 024117.
(101) te Vrugt, M.; Löwen, H.; Wittkowski, R. Classical Dynamical Density Functional Theory: From Fundamentals to Applications. *Adv. Phys.* **2020**, *69*, 121−247.
(102) Voukadinova, A.; Valiskó, M.; Gillespie, D. Assessing the Accuracy of Three Classical Density Functional Theories of the Electrical Double Layer. *Phys. Rev. E* **2018**, *98*, 012116.
(103) Rosenfeld, Y. Free-Energy Model for the Inhomogeneous Hard-Sphere Fluid Mixture and Density-Functional Theory of Freezing. *Phys. Rev. Lett.* **1989**, *63*, 980−983.
(104) Yu, Y.-X.; Wu, J. Structures of Hard-Sphere Fluids From a Modified Fundamental-Measure Theory. *J. Chem. Phys.* **2002**, *117*, 10156−10164.
(105) Roth, R.; Evans, R.; Lang, A.; Kahl, G. Fundamental Measure Theory for Hard-Sphere Mixtures Revisited: The White Bear Version. *J. Phys.: Condens. Matter* **2002**, *14*, 12063−12078.
(106) Gillespie, D.; Nonner, W.; Eisenberg, R. S. Density Functional Theory of Charged, Hard-Sphere Fluids. *Phys. Rev. E* **2003**, *68*, 031503.
(107) Wang, Z.; Liu, L.; Neretnieks, I. The Weighted Correlation Approach for Density Functional Theory: A Study on the Structure of the Electric Double Layer. *J. Phys.: Condens. Matter* **2011**, *23*, 175002.
(108) Blum, L. Mean Spherical Model for Asymmetric Electrolytes. *Mol. Phys.* **1975**, *30*, 1529−1535.
(109) Roth, R.; Gillespie, D. Shells of Charge: A Density Functional Theory for Charged Hard Spheres. *J. Phys.: Condens. Matter* **2016**, *28*, 244006.
(110) Jiang, J.; Gillespie, D. Revisiting the Charged Shell Model: A Density Functional Theory for Electrolytes. *J. Chem. Theory Comput.* **2021**, *17*, 2409−2416.
(111) Henderson, D.; Blum, L. Some Exact Results and the Application of the Mean Spherical Approximation to Charged Hard Spheres Near a Charged Hard Wall. *J. Chem. Phys.* **1978**, *69*, 5441−5449.
(112) Silvestre-Alcantara, W.; Bhuiyan, L. B.; Jiang, J.; Wu, J. Z.; Henderson, D. Contact Value Relations and Density Functional Theory for the Electrical Double Layer. *Mol. Phys.* **2014**, *112*, 3144−3151.
(113) Henderson, D.; Boda, D. On a Conjecture of Fawcett. *J. Electroanal. Chem.* **2005**, *582*, 16−20.
(114) Jiang, J.; Cao, D.; Henderson, D.; Wu, J. Revisiting Density Functionals for the Primitive Model of Electric Double Layers. *J. Chem. Phys.* **2014**, *140*, 044714.
(115) Jiang, J.; Cao, D.; Henderson, D.; Wu, J. A contact-corrected density functional theory for electrolytes at an interface. *Phys. Chem. Chem. Phys.* **2014**, *16*, 3934−3938.
(116) Lee, L. L. *Molecular Thermodynamics of Electrolyte Solutions*; World Scientific Publishing Company: Singapore; Hackensack, NJ, 2021; pp xii, 296pp.
(117) Lee, J. W.; Nilson, R. H.; Templeton, J. A.; Griffiths, S. K.; Kung, A.; Wong, B. M. Comparison of Molecular Dynamics With Classical Density Functional and Poisson-Boltzmann Theories of the Electric Double Layer in Nanochannels. *J. Chem. Theory Comput.* **2012**, *8*, 2012−2022.
(118) Pizio, O.; Sokołowski, S.; Sokołowska, Z. Electric Double Layer Capacitance of Restricted Primitive Model for an Ionic Fluid in Slit-Like Nanopores: A Density Functional Approach. *J. Chem. Phys.* **2012**, *137*, 234705.
(119) Forsman, J.; Woodward, C. E.; Trulsson, M. A Classical Density Functional Theory of Ionic Liquids. *J. Phys. Chem. B* **2011**, *115*, 4606−4612.
(120) Li, B.; Ma, K.; Wang, Y. L.; Turesson, M.; Woodward, C. E.; Forsman, J. Fused Coarse-Grained Model of Aromatic Ionic Liquids and Their Behaviour at Electrodes. *Phys. Chem. Chem. Phys.* **2016**, *18*, 8165−8173.
(121) Wu, J.; Li, Z. Density-Functional Theory for Complex Fluids. *Annu. Rev. Phys. Chem.* **2007**, *58*, 85−112.
(122) Zhou, M.; Wu, J. A GPU Implementation of Classical Density Functional Theory for Rapid Prediction of Gas Adsorption in Nanoporous Materials. *J. Chem. Phys.* **2020**, *153*, 074101.

https://doi.org/10.1021/acs.chemrev.2c00097
Chem. Rev. XXXX, XXX, XXX−XXX

(123) Frumkin, A. XLIII. On the Theory of Electrocapillarity: II. *Philos. Mag.* **1920**, *40*, 375−385.
(124) Badiali, J.; Rosinberg, M.; Goodisman, J. Effect of Solvent on Properties of the Liquid Metal Surface. *J. Electroanal. Chem. Interface Electrochem.* **1981**, *130*, 31−45.
(125) Abidi, N.; Lim, K. R. G.; Seh, Z. W.; Steinmann, S. N. Atomistic Modeling of Electrocatalysis: Are We There Yet? *WIREs Comput. Mol. Sci.* **2021**, *11*, No. e1499.
(126) Leung, K. DFT Modelling of Explicit Solid-Solid Interfaces in Batteries: Methods and Challenges. *Phys. Chem. Chem. Phys.* **2020**, *22*, 10412−10425.
(127) Yang, X.-H.; Zhuang, Y.-B.; Zhu, J.-X.; Le, J.-B.; Cheng, J. Recent Progress on Multiscale Modeling of Electrochemistry. *WIREs Comput. Mol. Sci.* **2021**, e1559.
(128) Monroe, C. W. Mechanics of the Ideal Double-Layer Capacitor. *J. Electrochem. Soc.* **2020**, *167*, 013550.
(129) Luryi, S. Quantum Capacitance Devices. *Appl. Phys. Lett.* **1988**, *52*, 501−503.
(130) Kondrat, S.; Kornyshev, A.; Stoeckli, F.; Centeno, T. The Effect of Dielectric Permittivity on the Capacitance of Nanoporous Electrodes. *Electrochem. Commun.* **2013**, *34*, 348−350.
(131) Gauthier, J. A.; Ringe, S.; Dickens, C. F.; Garza, A. J.; Bell, A. T.; Head-Gordon, M.; Nørskov, J. K.; Chan, K. Challenges in Modeling Electrochemical Reaction Energetics With Polarizable Continuum Models. *ACS Catal.* **2019**, *9*, 920−931.
(132) Haruyama, J.; Ikeshoji, T.; Otani, M. Electrode Potential From Density Functional Theory Calculations Combined With Implicit Solvation Theory. *Phys. Rev. Mater.* **2018**, *2*, 095801.
(133) Kovalenko, A.; Hirata, F. Self-Consistent Description of a Metal−Water Interface by the Kohn−Sham Density Functional Theory and the Three-Dimensional Reference Interaction Site Model. *J. Chem. Phys.* **1999**, *110*, 10095−10112.
(134) Sato, H. A. Modern Solvation Theory: Quantum Chemistry and Statistical Chemistry. *Phys. Chem. Chem. Phys.* **2013**, *15*, 7450−7465.
(135) Nishihara, S.; Otani, M. Hybrid Solvation Models for Bulk, Interface, and Membrane: Reference Interaction Site Methods Coupled With Density Functional Theory. *Phys. Rev. B* **2017**, *96*, 115429.
(136) Schwarz, K.; Sundararaman, R. The Electrochemical Interface in First-Principles Calculations. *Surf. Sci. Rep.* **2020**, *75*, 100492.
(137) Letchworth-Weaver, K.; Arias, T. A. Joint Density Functional Theory of the Electrode-Electrolyte Interface: Application to Fixed Electrode Potentials, Interfacial Capacitances, and Potentials of Zero Charge. *Phys. Rev. B* **2012**, *86*, 075140.
(138) Melander, M. M. Grand Canonical Ensemble Approach to Electrochemical Thermodynamics, Kinetics, and Model Hamiltonians. *Curr. Opin. Electrochem.* **2021**, *29*, 100749.
(139) Melander, M. M.; Kuisma, M. J.; Christensen, T. E. K.; Honkala, K. Grand-Canonical Approach to Density Functional Theory of Electrocatalytic Systems: Thermodynamics of Solid-Liquid Interfaces at Constant Ion and Electrode Potentials. *J. Chem. Phys.* **2019**, *150*, 041706.
(140) Bhandari, A.; Peng, C.; Dziedzic, J.; Anton, L.; Owen, J. R.; Kramer, D.; Skylaris, C.-K. Electrochemistry From First-Principles in the Grand Canonical Ensemble. *J. Chem. Phys.* **2021**, *155*, 024114.
(141) Mathew, K.; Kolluru, V. S. C.; Mula, S.; Steinmann, S. N.; Hennig, R. G. Implicit Self-Consistent Electrolyte Model in Plane-Wave Density-Functional Theory. *J. Chem. Phys.* **2019**, *151*, 234101.
(142) Dziedzic, J.; Bhandari, A.; Anton, L.; Peng, C.; Womack, J. C.; Famili, M.; Kramer, D.; Skylaris, C.-K. Practical Approach to Large-Scale Electronic Structure Calculations in Electrolyte Solutions via Continuum-Embedded Linear-Scaling Density Functional Theory. *J. Phys. Chem. C* **2020**, *124*, 7860−7872.
(143) Huang, J.; Chen, S.; Eikerling, M. Grand-Canonical Model of Electrochemical Double Layers From a Hybrid Density−Potential Functional. *J. Chem. Theory Comput.* **2021**, *17*, 2417−2430.
(144) Huang, J. Hybrid Density-Potential Functional Theory of Electric Double Layers. *Electrochim. Acta* **2021**, *389*, 138720.
(145) Guo, W.; Yu, C.; Li, S. F.; Qiu, J. S. Toward Commercial-Level Mass-Loading Electrodes for Supercapacitors: Opportunities, Challenges and Perspectives. *Energy Environ. Sci.* **2021**, *14*, 576−601.
(146) Lian, C.; Liu, K.; Tian, Y.; Wesolowski, D. J.; Wu, J. *Handbook of Porous Materials*; Chapter 1, pp 1−69.
(147) Da Silva, L. M.; Cesar, R.; Moreira, C. M.; Santos, J. H.; De Souza, L. G.; Pires, B. M.; Vicentini, R.; Nunes, W.; Zanin, H. Reviewing the Fundamentals of Supercapacitors and the Difficulties Involving the Analysis of the Electrochemical Findings Obtained for Porous Electrode Materials. *Energy Storage Mater.* **2020**, *27*, 555−590.
(148) Chmiola, J.; Yushin, G.; Gogotsi, Y.; Portet, C.; Simon, P.; Taberna, P. L. Anomalous Increase in Carbon Capacitance at Pore Sizes Less Than 1 Nanometer. *Science* **2006**, *313*, 1760−1763.
(149) Centeno, T. A.; Sereda, O.; Stoeckli, F. Capacitance in Carbon Pores of 0.7 to 15 Nm: A Regular Pattern. *Phys. Chem. Chem. Phys.* **2011**, *13*, 12403−12406.
(150) Garcia-Gomez, A.; Moreno-Fernandez, G.; Lobato, B.; Centeno, T. A. Constant Capacitance in Nanopores of Carbon Monoliths. *Phys. Chem. Chem. Phys.* **2015**, *17*, 15687−15690.
(151) Jäckel, N.; Simon, P.; Gogotsi, Y.; Presser, V. Increase in Capacitance by Subnanometer Pores in Carbon. *ACS Energy Lett.* **2016**, *1*, 1262−1265.
(152) Huang, J.; Sumpter, B.; Meunier, V. A Universal Model for Nanoporous Carbon Supercapacitors Applicable to Diverse Pore Regimes, Carbon Materials, and Electrolytes. *Chem. - Eur. J.* **2008**, *14*, 6614−6626.
(153) Shim, Y.; Kim, H. J. Nanoporous Carbon Supercapacitors in an Ionic Liquid: A Computer Simulation Study. *ACS Nano* **2010**, *4*, 2345−2355.
(154) Feng, G.; Qiao, R.; Huang, J.; Sumpter, B. G.; Meunier, V. Ion Distribution in Electrified Micropores and Its Role in the Anomalous Enhancement of Capacitance. *ACS Nano* **2010**, *4*, 2382−2390.
(155) Jiang, D.-e.; Jin, Z.; Wu, J. Oscillation of Capacitance Inside Nanopores. *Nano Lett.* **2011**, *11*, 5373−5377.
(156) Wu, P.; Huang, J.; Meunier, V.; Sumpter, B. G.; Qiao, R. Complex Capacitance Scaling in Ionic Liquids-Filled Nanopores. *ACS Nano* **2011**, *5*, 9044−9051.
(157) Feng, G.; Cummings, P. T. Supercapacitor Capacitance Exhibits Oscillatory Behavior as a Function of Nanopore Size. *J. Phys. Chem. Lett.* **2011**, *2*, 2859−2864.
(158) Jiang, D.-e.; Jin, Z.; Henderson, D.; Wu, J. Solvent Effect on the Pore-Size Dependence of an Organic Electrolyte Supercapacitor. *J. Phys. Chem. Lett.* **2012**, *3*, 1727−1731.
(159) Kondrat, S.; Georgi, N.; Fedorov, M. V.; Kornyshev, A. A. A Superionic State in Nano-Porous Double-Layer Capacitors: Insights From Monte Carlo Simulations. *Phys. Chem. Chem. Phys.* **2011**, *13*, 11359−11366.
(160) Kondrat, S.; Perez, C. R.; Presser, V.; Gogotsi, Y.; Kornyshev, A. A. Effect of Pore Size and Its Dispersity on the Energy Storage in Nanoporous Supercapacitors. *Energy Environ. Sci.* **2012**, *5*, 6474−6479.
(161) Xing, L.; Vatamanu, J.; Borodin, O.; Bedrov, D. On the Atomistic Nature of Capacitance Enhancement Generated by Ionic Liquid Electrolyte Confined in Subnanometer Pores. *J. Phys. Chem. Lett.* **2013**, *4*, 132−140.
(162) Varanasi, S. R.; Bhatia, S. K. Capacitance Optimization in Nanoscale Electrochemical Supercapacitors. *J. Phys. Chem. C* **2015**, *119*, 17573−17584.
(163) Varanasi, S. R.; Farmahini, A. H.; Bhatia, S. K. Complementary Effects of Pore Accessibility and Decoordination on the Capacitance of Nanoporous Carbon Electrochemical Supercapacitors. *J. Phys. Chem. C* **2015**, *119*, 28809−28818.
(164) Urita, K.; Urita, C.; Fujita, K.; Horio, K.; Yoshida, M.; Moriguchi, I. The Ideal Porous Structure of EDLC Carbon Electrodes With Extremely High Capacitance. *Nanoscale* **2017**, *9*, 15643−15649.
(165) Neal, J. N.; Wesolowski, D. J.; Henderson, D.; Wu, J. Electric Double Layer Capacitance for Ionic Liquids in Nanoporous Electrodes: Effects of Pore Size and Ion Composition. *J. Mol. Liq.* **2018**, *270*, 145−150.

https://doi.org/10.1021/acs.chemrev.2c00097
Chem. Rev. XXXX, XXX, XXX−XXX

(166) Yang, F. Size Effect on Electric-Double-Layer Capacitances of Conducting Structures. *Phys. Lett. A* **2019**, *383*, 2353−2360.
(167) Lahrar, E. H.; Simon, P.; Merlet, C. Carbon−Carbon Supercapacitors: Beyond the Average Pore Size or How Electrolyte Confinement and Inaccessible Pores Affect the Capacitance. *J. Chem. Phys.* **2021**, *155*, 184703.
(168) Lian, Z.; Chao, H.; Wang, Z.-G. Effects of Confinement and Ion Adsorption in Ionic Liquid Supercapacitors With Nanoporous Electrodes. *ACS Nano* **2021**, *15*, 11724−11733.
(169) Kondrat, S.; Kornyshev, A. Superionic State in Double-Layer Capacitors With Nanoporous Electrodes. *J. Phys.: Condens. Matter* **2011**, *23*, 022201.
(170) Jiang, D.-e.; Wu, J. Microscopic Insights Into the Electrochemical Behavior of Nonaqueous Electrolytes in Electric Double-Layer Capacitors. *J. Phys. Chem. Lett.* **2013**, *4*, 1260−1267.
(171) Merlet, C.; Rotenberg, B.; Madden, P. A.; Taberna, P.-L.; Simon, P.; Gogotsi, Y.; Salanne, M. On the Molecular Origin of Supercapacitance in Nanoporous Carbon Electrodes. *Nat. Mater.* **2012**, *11*, 306−310.
(172) Huang, J.; Sumpter, B.; Meunier, V. Theoretical Model for Nanoporous Carbon Supercapacitors. *Angew. Chem., Int. Ed.* **2008**, *47*, 520−524.
(173) Largeot, C.; Portet, C.; Chmiola, J.; Taberna, P.-L.; Gogotsi, Y.; Simon, P. Relation Between the Ion Size and Pore Size for an Electric Double-Layer Capacitor. *J. Am. Chem. Soc.* **2008**, *130*, 2730−2731.
(174) Kondrat, S.; Pérez, C. R.; Presser, V.; Gogotsi, Y.; Kornyshev, A. A. Effect of Pore Size and Its Dispersity on the Energy Storage in Nanoporous Supercapacitors. *Energy Environ. Sci.* **2012**, *5*, 6474−6479.
(175) Mo, T.; Zeng, L.; Wang, Z.; Kondrat, S.; Feng, G. Symmetrizing Cathode-Anode Response to Speed up Charging of Nanoporous Supercapacitors. *Green Energy Environ* **2022**, *7*, 95−104.
(176) Huang, J.; Sumpter, B. G.; Meunier, V.; Yushin, G.; Portet, C.; Gogotsi, Y. Curvature Effects in Carbon Nanomaterials: Exohedral Versus Endohedral Supercapacitors. *J. Mater. Res.* **2010**, *25*, 1525−1531.
(177) Feng, G.; Jiang, D.-e.; Cummings, P. T. Curvature Effect on the Capacitance of Electric Double Layers at Ionic Liquid/Onion-Like Carbon Interfaces. *J. Chem. Theory Comput.* **2012**, *8*, 1058−1063.
(178) Ma, K.; Woodward, C. E.; Forsman, J. Classical Density Functional Study on Interfacial Structure and Differential Capacitance of Ionic Liquids Near Charged Surfaces. *J. Phys. Chem. C* **2014**, *118*, 15825−15834.
(179) Janssen, M. Curvature Affects Electrolyte Relaxation: Studies of Spherical and Cylindrical Electrodes. *Phys. Rev. E* **2019**, *100*, 042602.
(180) Aslyamov, T.; Sinkov, K.; Akhatov, I. Electrolyte Structure Near Electrodes With Molecular-Size Roughness. *Phys. Rev. E* **2021**, *103*, L060102.
(181) Keshavarzi, E.; Abareghi, M.; Helmi, A. Curvature Dependence of the Camel-Bell Curve Transition on the Capacitance Curve of Spherical Electric Double-Layer in Porous Electrodes: Density Functional Theory. *Electrochim. Acta* **2019**, *313*, 303−310.
(182) Yang, J.; Gallegos, A.; Lian, C.; Deng, S.; Liu, H.; Wu, J. Curvature Effects on Electric-Double-Layer Capacitance. *Chin. J. Chem. Eng.* **2021**, *31*, 145−152.
(183) Bo, Z.; Li, C.; Yang, H.; Ostrikov, K.; Yan, J.; Cen, K. Design of Supercapacitor Electrodes Using Molecular Dynamics Simulations. *Nano-Micro Lett.* **2018**, *10*, 33.
(184) Reindl, A.; Bier, M.; Dietrich, S. Electrolyte Solutions at Curved Electrodes. I. Mesoscopic Approach. *J. Chem. Phys.* **2017**, *146*, 154703.
(185) Reindl, A.; Bier, M.; Dietrich, S. Electrolyte Solutions at Curved Electrodes. II. Microscopic Approach. *J. Chem. Phys.* **2017**, *146*, 154704.
(186) Lian, C.; Jiang, D.-e.; Liu, H.; Wu, J. A Generic Model for Electric Double Layers in Porous Electrodes. *J. Phys. Chem. C* **2016**, *120*, 8704−8710.
(187) Seebeck, J.; Merlet, C.; Meißner, R. H. Elucidating Curvature-Capacitance Relationships in Carbon-Based Supercapacitors. *Phys. Rev. Lett.* **2022**, *128*, 086001.
(188) Ma, K.; Wang, X.; Forsman, J.; Woodward, C. E. Molecular Dynamic Simulations of Ionic Liquid's Structural Variations From Three to One Layers Inside a Series of Slit and Cylindrical Nanopores. *J. Phys. Chem. C* **2017**, *121*, 13539−13548.
(189) Jäckel, N.; Rodner, M.; Schreiber, A.; Jeongwook, J.; Zeiger, M.; Aslan, M.; Weingarth, D.; Presser, V. Anomalous or Regular Capacitance? The Influence of Pore Size Dispersity on Double-Layer Formation. *J. Power Sources* **2016**, *326*, 660−671.
(190) Bohinc, K.; Bossa, G. V.; May, S. Incorporation of Ion and Solvent Structure Into Mean-Field Modeling of the Electric Double Layer. *Advances in colloid and interface science* **2017**, *249*, 220−233.
(191) Fleharty, M. E.; van Swol, F.; Petsev, D. N. Solvent Role in the Formation of Electric Double Layers With Surface Charge Regulation: A Bystander or a Key Participant? *Phys. Rev. Lett.* **2016**, *116*, 048301.
(192) Henderson, D.; Jiang, D.-e.; Jin, Z.; Wu, J. Application of Density Functional Theory to Study the Double Layer of an Electrolyte With an Explicit Dimer Model for the Solvent. *J. Phys. Chem. B* **2012**, *116*, 11356−11361.
(193) Jiang, D. E.; Wu, J. Z. Unusual Effects of Solvent Polarity on Capacitance for Organic Electrolytes in a Nanoporous Electrode. *Nanoscale* **2014**, *6*, 5545−5550.
(194) Pal, B.; Yang, S.; Ramesh, S.; Thangadurai, V.; Jose, R. Electrolyte Selection for Supercapacitive Devices: A Critical Review. *Nanoscale Adv.* **2019**, *1*, 3807−3835.
(195) Niedermeyer, H.; Hallett, J. P.; Villar-Garcia, I. J.; Hunt, P. A.; Welton, T. Mixtures of Ionic Liquids. *Chem. Soc. Rev.* **2012**, *41*, 7780−7802.
(196) Van Aken, K. L.; Beidaghi, M.; Gogotsi, Y. Formulation of Ionic-Liquid Electrolyte to Expand the Voltage Window of Supercapacitors. *Angew. Chem., Int. Ed.* **2015**, *54*, 4806−4809.
(197) Lian, C.; Liu, K.; Van Aken, K. L.; Gogotsi, Y.; Wesolowski, D. J.; Liu, H. L.; Jiang, D. E.; Wu, J. Z. Enhancing the Capacitive Performance of Electric Double-Layer Capacitors With Ionic Liquid Mixtures. *ACS Energy Lett.* **2016**, *1*, 21−26.
(198) Lian, C.; Liu, H.; Li, C.; Wu, J. Hunting Ionic Liquids With Large Electrochemical Potential Windows. *AIChE J.* **2019**, *65*, 804−810.
(199) Lian, C.; Liu, H.; Wu, J. Ionic Liquid Mixture Expands the Potential Window and Capacitance of a Supercapacitor in Tandem. *J. Phys. Chem. C* **2018**, *122*, 18304−18310.
(200) Osti, N. C.; Gallegos, A.; Dyatkin, B.; Wu, J.; Gogotsi, Y.; Mamontov, E. Mixed Ionic Liquid Improves Electrolyte Dynamics in Supercapacitors. *J. Phys. Chem. C* **2018**, *122*, 10476−10481.
(201) Fang, A.; Smolyanitsky, A. Simulation Study of the Capacitance and Charging Mechanisms of Ionic Liquid Mixtures Near Carbon Electrodes. *J. Phys. Chem. C* **2019**, *123*, 1610−1618.
(202) Neal, J. N.; Wesolowski, D. J.; Henderson, D.; Wu, J. Ion Distribution and Selectivity of Ionic Liquids in Microporous Electrodes. *J. Chem. Phys.* **2017**, *146*, 174701.
(203) Alam, M. T.; Islam, M. M.; Okajima, T.; Ohsaka, T. Electrical Double Layer in Mixtures of Room-Temperature Ionic Liquids. *J. Phys. Chem. C* **2009**, *113*, 6596−6601.
(204) Wang, X.; Mehandzhiyski, A. Y.; Arstad, B.; Van Aken, K. L.; Mathis, T. S.; Gallegos, A.; Tian, Z.; Ren, D.; Sheridan, E.; Grimes, B. A.; Jiang, D.-e.; Wu, J.; Gogotsi, Y.; Chen, D. Selective Charging Behavior in an Ionic Mixture Electrolyte-Supercapacitor System for Higher Energy and Power. *J. Am. Chem. Soc.* **2017**, *139*, 18681−18687.
(205) Costa, R.; Voroshylova, I. V.; Cordeiro, M. N. D.; Pereira, C. M.; Silva, A. F. Enhancement of Differential Double Layer Capacitance and Charge Accumulation by Tuning the Composition of Ionic Liquids Mixtures. *Electrochim. Acta* **2018**, *261*, 214−220.
(206) Gallegos, A.; Lian, C.; Dyatkin, B.; Wu, J. Side-Chain Effects on the Capacitive Behaviour of Ionic Liquids in Microporous Electrodes. *Mol. Phys.* **2019**, *117*, 3603−3613.
(207) Dyatkin, B.; Osti, N. C.; Gallegos, A.; Zhang, Y.; Mamontov, E.; Cummings, P. T.; Wu, J.; Gogotsi, Y. Electrolyte Cation Length Influences Electrosorption and Dynamics in Porous Carbon Supercapacitors. *Electrochim. Acta* **2018**, *283*, 882−893.

https://doi.org/10.1021/acs.chemrev.2c00097
Chem. Rev. XXXX, XXX, XXX−XXX

(208) Henderson, D.; Lamperski, S.; Bari Bhuiyan, L.; Wu, J. The Tail Effect on the Shape of an Electrical Double Layer Differential Capacitance Curve. *J. Chem. Phys.* **2013**, *138*, 144704.
(209) Yang, J.; Lian, C.; Liu, H. Chain Length Matters: Structural Transition and Capacitance of Room Temperature Ionic Liquids in Nanoporous Electrodes. *Chem. Eng. Sci.* **2020**, *227*, 115927.
(210) Pitawela, N. R.; Shaw, S. K. Imidazolium Triflate Ionic Liquids' Capacitance−Potential Relationships and Transport Properties Affected by Cation Chain Lengths. *ACS Meas. Sci. Au* **2021**, *1*, 117−130.
(211) Lian, C.; Su, H.; Liu, H.; Wu, J. Electrochemical Behavior of Nanoporous Supercapacitors With Oligomeric Ionic Liquids. *J. Phys. Chem. C* **2018**, *122*, 14402−14407.
(212) Forse, A. C.; Griffin, J. M.; Merlet, C.; Bayley, P. M.; Wang, H.; Simon, P.; Grey, C. P. NMR Study of Ion Dynamics and Charge Storage in Ionic Liquid Supercapacitors. *J. Am. Chem. Soc.* **2015**, *137*, 7231−7242.
(213) Liu, K.; Wu, J. Boosting the Performance of Ionic-Liquid-Based Supercapacitors With Polar Additives. *J. Phys. Chem. C* **2016**, *120*, 24041−24047.
(214) Liu, K.; Lian, C.; Henderson, D.; Wu, J. Impurity Effects on Ionic-Liquid-Based Supercapacitors. *Mol. Phys.* **2017**, *115*, 454−464.
(215) Lian, C.; Liu, K.; Liu, H.; Wu, J. Impurity Effects on Charging Mechanism and Energy Storage of Nanoporous Supercapacitors. *J. Phys. Chem. C* **2017**, *121*, 14066−14072.
(216) Cats, P.; van Roij, R. The Differential Capacitance as a Probe for the Electric Double Layer Structure and the Electrolyte Bulk Composition. *J. Chem. Phys.* **2021**, *155*, 104702.
(217) Schröer, W.; Vale, V. R. Liquid ExtendashLiquid Phase Separation in Solutions of Ionic Liquids: Phase Diagrams, Corresponding State Analysis and Comparison With Simulations of the Primitive Model. *J. Phys.: Condens. Matter* **2009**, *21*, 424119.
(218) Hayes, R.; Warr, G. G.; Atkin, R. Structure and Nanostructure in Ionic Liquids. *Chem. Rev.* **2015**, *115*, 6357−6426.
(219) Groda, Y.; Dudka, M.; Kornyshev, A. A.; Oshanin, G.; Kondrat, S. Superionic Liquids in Conducting Nanoslits: Insights From Theory and Simulations. *J. Phys. Chem. C* **2021**, *125*, 4968−4976.
(220) Bedanov, V. M.; Peeters, F. M. Ordering and Phase-Transitions of Charged-Particles in a Classical Finite 2-Dimensional System. *Phys. Rev. B* **1994**, *49*, 2667−2676.
(221) Dudka, M.; Kondrat, S.; Bénichou, O.; Kornyshev, A. A.; Oshanin, G. Superionic Liquids in Conducting Nanoslits: A Variety of Phase Transitions and Ensuing Charging Behavior. *J. Chem. Phys.* **2019**, *151*, 184105.
(222) Schmickler, W.; Henderson, D. Charge Storage in Two-Dimensional Systems. *J. Electroanal. Chem.* **2020**, *872*, 114101.
(223) Stanley, H. E. *Introduction to Phase Transitions and Critical Phenomena*; Oxford University Press: New York, 1987; pp xx, 308pp.
(224) Lee, A. A.; Perkin, S. Ion−Image Interactions and Phase Transition at Electrolyte−Metal Interfaces. *J. Phys. Chem. Lett.* **2016**, *7*, 2753−2757.
(225) Sha, M.; Wu, G.; Fang, H.; Zhu, G.; Liu, Y. Liquid-To-Solid Phase Transition of a 1,3-Dimethylimidazolium Chloride Ionic Liquid Monolayer Confined Between Graphite Walls. *J. Phys. Chem. C* **2008**, *112*, 18584−18587.
(226) Liu, K.; Zhang, P.; Wu, J. Does Capillary Evaporation Limit the Accessibility of Nonaqueous Electrolytes to the Ultrasmall Pores of Carbon Electrodes? *J. Chem. Phys.* **2018**, *149*, 234708.
(227) Pizio, O.; Patrykiejew, A.; Sokołowski, S. Phase Behavior of Ionic Fluids in Slitlike Pores: A Density Functional Approach for the Restricted Primitive Model. *J. Chem. Phys.* **2004**, *121*, 11957−11964.
(228) Pizio, O.; Sokołowski, S. Phase Behavior of the Restricted Primitive Model of Ionic Fluids With Association in Slitlike Pores. Density-Functional Approach. *J. Chem. Phys.* **2005**, *122*, 144707.
(229) Szparaga, R.; Woodward, C. E.; Forsman, J. Capillary Condensation of Ionic Liquid Solutions in Porous Electrodes. *J. Phys. Chem. C* **2013**, *117*, 1728−1734.
(230) Szparaga, R.; Woodward, C. E.; Forsman, J. Theoretical Prediction of the Capacitance of Ionic Liquid Films. *J. Phys. Chem. C* **2012**, *116*, 15946−15951.
(231) Lu, H. D.; Stenberg, S.; Woodward, C. E.; Forsman, J. Structural Transitions at Electrodes, Immersed in Simple Ionic Liquid Models. *Soft Matter* **2021**, *17*, 3876−3885.
(232) Cruz, C.; Kondrat, S.; Lomba, E.; Ciach, A. Effect of Proximity to Ionic Liquid-Solvent Demixing on Electrical Double Layers. *J. Mol. Liq.* **2019**, *294*, 111368.
(233) Loubet, B.; Manghi, M.; Palmeri, J. A Variational Approach to the Liquid-Vapor Phase Transition for Hardcore Ions in the Bulk and in Nanopores. *J. Chem. Phys.* **2016**, *145*, 044107.
(234) Limmer, D. T. Interfacial Ordering and Accompanying Divergent Capacitance at Ionic Liquid-Metal Interfaces. *Phys. Rev. Lett.* **2015**, *115*, 256102.
(235) Holovko, M.; Patsahan, T.; Patsahan, O. Application of the Ionic Association Concept to the Study of the Phase Behaviour of Size-Asymmetric Ionic Fluids in Disordered Porous Media. *J. Mol. Liq.* **2017**, *235*, 53−59.
(236) Zhan, C.; Neal, J.; Wu, J.; Jiang, D.-e. Quantum Effects on the Capacitance of Graphene-Based Electrodes. *J. Phys. Chem. C* **2015**, *119*, 22297−22303.
(237) Zhan, C.; Jiang, D.-e. Contribution of Dielectric Screening to the Total Capacitance of Few-Layer Graphene Electrodes. *J. Phys. Chem. Lett.* **2016**, *7*, 789−794.
(238) Son, C. Y.; Wang, Z.-G. Image-Charge Effects on Ion Adsorption Near Aqueous Interfaces. *Proc. Natl. Acad. Sci. U. S. A.* **2021**, *118*, No. e2020615118.
(239) da Silva, D. A. C.; Paulista Neto, A. J.; Pascon, A. M.; Fileti, E. E.; Fonseca, L. R. C.; Zanin, H. G. Combined Density Functional Theory and Molecular Dynamics Simulations to Investigate the Effects of Quantum and Double-Layer Capacitances in Functionalized Graphene as the Electrode Material of Aqueous-Based Supercapacitors. *J. Phys. Chem. C* **2021**, *125*, 5518−5524.
(240) Zhang, B.; Peng, Z.; Song, L.; Wu, X.; Fu, X. Computational Screening Toward Quantum Capacitance of Transition-Metals and Vacancy Doped/Co-Doped Graphene as Electrode of Supercapacitors. *Electrochim. Acta* **2021**, *385*, 138432.
(241) Zhan, C.; Zhang, Y.; Cummings, P. T.; Jiang, D.-e. Enhancing graphene capacitance by nitrogen: effects of doping configuration and concentration. *Phys. Chem. Chem. Phys.* **2016**, *18*, 4668−4674.
(242) Zhan, C.; Zhang, Y.; Cummings, P. T.; Jiang, D.-e. Computational Insight Into the Capacitive Performance of Graphene Edge Planes. *Carbon* **2017**, *116*, 278−285.
(243) Conway, B. E.; Gileadi, E. Kinetic theory of pseudo-capacitance and electrode reactions at appreciable surface coverage. *Trans. Faraday Soc.* **1962**, *58*, 2493−2509.
(244) Costentin, C.; Saveant, J. M. Energy Storage: Pseudocapacitance in Prospect. *Chem. Sci.* **2019**, *10*, 5656−5666.
(245) Ozolins, V.; Zhou, F.; Asta, M. Ruthenia-Based Electrochemical Supercapacitors: Insights From First-Principles Calculations. *Acc. Chem. Res.* **2013**, *46*, 1084−1093.
(246) Fleischmann, S.; Zhang, Y.; Wang, X.; Cummings, P. T.; Wu, J.; Simon, P.; Gogotsi, Y.; Presser, V.; Augustyn, V. Continuous Transition From Double-Layer to Faradaic Charge Storage in Confined Electrolytes. *Nat. Energy* **2022**, *7*, 222−228.
(247) Ando, Y.; Okubo, M.; Yamada, A.; Otani, M. Capacitive Versus Pseudocapacitive Storage in MXene. *Adv. Funct. Mater.* **2020**, *30*, 2000820.
(248) Hörmann, N. G.; Reuter, K. Thermodynamic Cyclic Voltammograms Based on Ab Initio Calculations: Ag(111) in Halide-Containing Solutions. *J. Chem. Theory Comput.* **2021**, *17*, 1782−1794.
(249) Zhan, C.; Naguib, M.; Lukatskaya, M.; Kent, P. R. C.; Gogotsi, Y.; Jiang, D.-e. Understanding the MXene Pseudocapacitance. *J. Phys. Chem. Lett.* **2018**, *9*, 1223−1228.
(250) Wang, X.; Ong, G. M.; Naguib, M.; Wu, J. Theoretical Insights Into MXene Termination and Surface Charge Regulation. *J. Phys. Chem. C* **2021**, *125*, 21771−21779.

https://doi.org/10.1021/acs.chemrev.2c00097
Chem. Rev. XXXX, XXX, XXX−XXX

(251) Newman, J. S.; Tobias, C. W. Theoretical Analysis of Current Distribution in Porous Electrodes. *J. Electrochem. Soc.* **1962**, *109*, 1183.
(252) Johnson, A. M.; Newman, J. Desalting by Means of Porous Carbon Electrodes. *J. Electrochem. Soc.* **1971**, *118*, 510−517.
(253) Lin, C.; Ritter, J. A.; Popov, B. N.; White, R. E. A Mathematical Model of an Electrochemical Capacitor With Double-Layer and Faradaic Processes. *J. Electrochem. Soc.* **1999**, *146*, 3168−3175.
(254) Ferguson, T. R.; Bazant, M. Z. Nonequilibrium Thermodynamics of Porous Electrodes. *J. Electrochem. Soc.* **2012**, *159*, A1967−A1985.
(255) Lin, C. Q.; Popov, B. N.; Ploehn, H. J. Modeling the Effects of Electrode Composition and Pore Structure on the Performance of Electrochemical Capacitors. *J. Electrochem. Soc.* **2002**, *149*, A167−A175.
(256) Brousse, T.; Bélanger, D.; Long, J. W. To Be or Not to Be Pseudocapacitive? *J. Electrochem. Soc.* **2015**, *162*, A5185−A5189.
(257) Srinivasan, V.; Weidner, J. W. Mathematical Modeling of Electrochemical Capacitors. *J. Electrochem. Soc.* **1999**, *146*, 1650−1658.
(258) Lin, C.; Popov, B. N.; Ploehn, H. J. Modeling the Effects of Electrode Composition and Pore Structure on the Performance of Electrochemical Capacitors. *J. Electrochem. Soc.* **2002**, *149*, A167.
(259) Staser, J. A.; Weidner, J. W. Mathematical Modeling of Hybrid Asymmetric Electrochemical Capacitors. *J. Electrochem. Soc.* **2014**, *161*, E3267−E3275.
(260) Jiang, J.; Cao, D.; en Jiang, D.; Wu, J. Time-Dependent Density Functional Theory for Ion Diffusion in Electrochemical Systems. *J. Phys.: Condens. Matter* **2014**, *26*, 284102.
(261) Bruna, M.; Burger, M.; Ranetbauer, H.; Wolfram, M.-T. Cross-diffusion systems with excluded-volume effects and asymptotic gradient flow structures. *J. Nonlinear Sci.* **2017**, *27*, 687−719.
(262) Carrillo, J. A.; Filbet, F.; Schmidtchen, M. Convergence of a finite volume scheme for a system of interacting species with cross-diffusion. *Numer. Math.* **2020**, *145*, 473−511.
(263) Lobaskin, V.; Netz, R. R. Diffusive-Convective Transition in the Non-Equilibrium Charging of an Electric Double Layer. *EPL (Europhysics Letters)* **2016**, *116*, 58001.
(264) Janssen, M.; Bier, M. Transient Dynamics of Electric Double-Layer Capacitors: Exact Expressions Within the Debye-Falkenhagen Approximation. *Phys. Rev. E* **2018**, *97*, 052616.
(265) Bazant, M. Z.; Thornton, K.; Ajdari, A. Diffuse-Charge Dynamics in Electrochemical Systems. *Phys. Rev. E* **2004**, *70*, 021506.
(266) van Soestbergen, M.; Biesheuvel, P. M.; Bazant, M. Z. Diffuse-Charge Effects on the Transient Response of Electrochemical Cells. *Phys. Rev. E* **2010**, *81*, 021503.
(267) Janssen, M.; van Roij, R. Reversible Heating in Electric Double Layer Capacitors. *Phys. Rev. Lett.* **2017**, *118*, 096001.
(268) Marini Bettolo Marconi, U.; Melchionna, S. Charge Transport in Nanochannels: A Molecular Theory. *Langmuir* **2012**, *28*, 13727−13740.
(269) Werkhoven, B. L.; Everts, J. C.; Samin, S.; van Roij, R. Flow-Induced Surface Charge Heterogeneity in Electrokinetics Due to Stern-Layer Conductance Coupled to Reaction Kinetics. *Phys. Rev. Lett.* **2018**, *120*, 264502.
(270) Asta, A. J.; Palaia, I.; Trizac, E.; Levesque, M.; Rotenberg, B. Lattice Boltzmann Electrokinetics Simulation of Nanocapacitors. *J. Chem. Phys.* **2019**, *151*, 114104.
(271) Huang, J.; Gao, Y.; Luo, J.; Wang, S.; Li, C.; Chen, S.; Zhang, J. Editors' Choice extemdashReview extemdashImpedance Response of Porous Electrodes: Theoretical Framework, Physical Models and Applications. *J. Electrochem. Soc.* **2020**, *167*, 166503.
(272) de Levie, R. On Porous Electrodes in Electrolyte Solutions: I. Capacitance Effects. *Electrochim. Acta* **1963**, *8*, 751−780.
(273) Moškon, J.; Gaberščcek, M. Transmission Line Models for Evaluation of Impedance Response of Insertion Battery Electrodes and Cells. *J. Power Sources Advances* **2021**, *7*, 100047.
(274) Mirzadeh, M.; Gibou, F.; Squires, T. M. Enhanced Charging Kinetics of Porous Electrodes: Surface Conduction as a Short-Circuit Mechanism. *Phys. Rev. Lett.* **2014**, *113*, 097701.
(275) Péan, C.; Merlet, C.; Rotenberg, B.; Madden, P. A.; Taberna, P.-L.; Daffos, B.; Salanne, M.; Simon, P. On the Dynamics of Charging in Nanoporous Carbon-Based Supercapacitors. *ACS Nano* **2014**, *8*, 1576−1583.
(276) Sakaguchi, H.; Baba, R. Charging Dynamics of the Electric Double Layer in Porous Media. *Phys. Rev. E* **2007**, *76*, 011501.
(277) Posey, F. A.; Morozumi, T. Theory of Potentiostatic and Galvanostatic Charging of the Double Layer in Porous Electrodes. *J. Electrochem. Soc.* **1966**, *113*, 176.
(278) Janssen, M. Transmission Line Circuit and Equation for an Electrolyte-Filled Pore of Finite Length. *Phys. Rev. Lett.* **2021**, *126*, 136002.
(279) Bi, S.; Banda, H.; Chen, M.; Niu, L.; Chen, M.; Wu, T.; Wang, J.; Wang, R.; Feng, J.; Chen, T.; Dincă, M.; Kornyshev, A. A.; Feng, G. Molecular Understanding of Charge Storage and Charging Dynamics in Supercapacitors With MOF Electrodes and Ionic Liquid Electrolytes. *Nat. Mater.* **2020**, *19*, 552−558.
(280) Kondrat, S.; Wu, P.; Qiao, R.; Kornyshev, A. A. Accelerating Charging Dynamics in Subnanometre Pores. *Nat. Mater.* **2014**, *13*, 387−393.
(281) Gan, Z.; Wang, Y.; Wang, M.; Gao, E.; Huo, F.; Ding, W.; He, H.; Zhang, S. Ionophobic nanopores enhancing the capacitance and charging dynamics in supercapacitors with ionic liquids. *J. Mater. Chem. A* **2021**, *9*, 15985−15992.
(282) Mo, T.; Bi, S.; Zhang, Y.; Presser, V.; Wang, X.; Gogotsi, Y.; Feng, G. Ion Structure Transition Enhances Charging Dynamics in Subnanometer Pores. *ACS Nano* **2020**, *14*, 2395−2403.
(283) Kondrat, S.; Kornyshev, A. Charging Dynamics and Optimization of Nanoporous Supercapacitors. *J. Phys. Chem. C* **2013**, *117*, 12399−12406.
(284) Zeng, L.; Wu, T.; Ye, T.; Mo, T.; Qiao, R.; Feng, G. Modeling Galvanostatic Charge−Discharge of Nanoporous Supercapacitors. *Nat. Comput. Sci.* **2021**, *1*, 725−731.
(285) Henrique, F.; Zuk, P. J.; Gupta, A. Charging Dynamics of Electrical Double Layers Inside a Cylindrical Pore: Predicting the Effects of Arbitrary Pore Size. *Soft Matter* **2021**, *18*, 198−213.
(286) Biesheuvel, P. M.; Bazant, M. Z. Nonlinear Dynamics of Capacitive Charging and Desalination by Porous Electrodes. *Phys. Rev. E* **2010**, *81*, 031502.
(287) Aslyamov, T.; Janssen, M. Analytical Solution to the Poisson-Nernst-Planck Equations for the Charging of a Long Electrolyte-Filled Slit Pore. 2022, *arxiv.org/abs/2201.11672*. https://arxiv.org/abs/2201.11672 (accessed 2022-05-22).
(288) Gupta, A.; Zuk, P. J.; Stone, H. A. Charging Dynamics of Overlapping Double Layers in a Cylindrical Nanopore. *Phys. Rev. Lett.* **2020**, *125*, 076001.
(289) Aslyamov, T.; Sinkov, K.; Akhatov, I. Relation between Charging Times and Storage Properties of Nanoporous Supercapacitors. *Nanomaterials* **2022**, *12*, 587.
(290) Breitsprecher, K.; Holm, C.; Kondrat, S. Charge Me Slowly, I Am in a Hurry: Optimizing Charge−Discharge Cycles in Nanoporous Supercapacitors. *ACS Nano* **2018**, *12*, 9733−9741.
(291) Breitsprecher, K.; Janssen, M.; Srimuk, P.; Mehdi, B. L.; Presser, V.; Holm, C.; Kondrat, S. How to Speed Up Ion Transport in Nanopores. *Nat. Commun.* **2020**, *11*, 6085.
(292) Lee, A. A.; Kondrat, S.; Oshanin, G.; Kornyshev, A. A. Charging Dynamics of Supercapacitors With Narrow Cylindrical Nanopores. *Nanotechnology* **2014**, *25*, 315401.
(293) He, Y.; Qiao, R.; Vatamanu, J.; Borodin, O.; Bedrov, D.; Huang, J.; Sumpter, B. G. Importance of Ion Packing on the Dynamics of Ionic Liquids During Micropore Charging. *J. Phys. Chem. Lett.* **2016**, *7*, 36−42.
(294) Forse, A. C.; Merlet, C.; Griffin, J. M.; Grey, C. P. New Perspectives on the Charging Mechanisms of Supercapacitors. *J. Am. Chem. Soc.* **2016**, *138*, 5731−5744.
(295) Meng, D.; Zheng, B.; Lin, G.; Sushko, M. L. Numerical Solution of 3D Poisson-Nernst-Planck Equations Coupled with Classical Density Functional Theory for Modeling Ion and Electron Transport

https://doi.org/10.1021/acs.chemrev.2c00097
Chem. Rev. XXXX, XXX, XXX−XXX

in a Confined Environment. *Commun. Comput. Phys.* **2014**, *16*, 1298−1322.
(296) Liu, H.; Maimaitiyiming, W. Efficient, Positive, and Energy Stable Schemes for Multi-D Poisson−Nernst−Planck Systems. *J. Sci. Comput.* **2021**, *87*, 92.
(297) Tivony, R.; Safran, S.; Pincus, P.; Silbert, G.; Klein, J. Charging Dynamics of an Individual Nanopore. *Nat. Commun.* **2018**, *9*, 4203.
(298) Palaia, I. Charged systems in, out of, and driven to equilibrium: from nanocapacitors to cement. Theses, Université Paris Saclay (COmUE), 2019.
(299) Beunis, F.; Strubbe, F.; Marescaux, M.; Beeckman, J.; Neyts, K.; Verschueren, A. R. M. Dynamics of Charge Transport in Planar Devices. *Phys. Rev. E* **2008**, *78*, 011502.
(300) Højgaard Olesen, L.; Bazant, M. Z.; Bruus, H. Strongly Nonlinear Dynamics of Electrolytes in Large Ac Voltages. *Phys. Rev. E* **2010**, *82*, 011501.
(301) Bamgbopa, M. O.; Belaineh, D.; Mengistie, D. A.; Edberg, J.; Engquist, I.; Berggren, M.; Tybrandt, K. Modelling of Heterogeneous Ion Transport in Conducting Polymer Supercapacitors. *J. Mater. Chem. A* **2021**, *9*, 2184−2194.
(302) Gebbie, M. A.; Valtiner, M.; Banquy, X.; Fox, E. T.; Henderson, W. A.; Israelachvili, J. N. Ionic Liquids Behave as Dilute Electrolyte Solutions. *Proc. Natl. Acad. Sci. U. S. A.* **2013**, *110*, 9674−9679.
(303) Yang, J.; Hu, X.; Kong, X.; Jia, P.; Ji, D.; Quan, D.; Wang, L.; Wen, Q.; Lu, D.; Wu, J.; Jiang, L.; Guo, W. Photo-Induced Ultrafast Active Ion Transport Through Graphene Oxide Membranes. *Nat. Commun.* **2019**, *10*, 1171.
(304) Qing, L.; Zhao, S.; Wang, Z.-G. Surface Charge Density in Electrical Double Layer Capacitors With Nanoscale Cathode−Anode Separation. *J. Phys. Chem. B* **2021**, *125*, 625−636.
(305) Qing, L.; Jiang, J. Double-Edged Sword of Ion-Size Asymmetry in Energy Storage of Supercapacitors. *J. Phys. Chem. Lett.* **2022**, *13*, 1438−1445.
(306) Liu, Y. Multiscale Mechanisms of Reaction-Diffusion Process in Electrode Systems: A Classical Density Functional Study. *Chem. Eng. Sci.* **2020**, *227*, 115899.
(307) Ma, M.; Xu, Z.; Zhang, L. Modified Poisson−Nernst−Planck Model With Coulomb and Hard-Sphere Correlations. *SIAM J. Appl. Math.* **2021**, *81*, 1645−1667.
(308) Kilic, M. S.; Bazant, M. Z.; Ajdari, A. Steric Effects in the Dynamics of Electrolytes at Large Applied Voltages. II. Modified Poisson-Nernst-Planck Equations. *Phys. Rev. E* **2007**, *75*, 021503.
(309) Babel, S.; Eikerling, M.; Löwen, H. Impedance Resonance in Narrow Confinement. *J. Phys. Chem. C* **2018**, *122*, 21724−21734.
(310) Pilon, L.; Wang, H.; d'Entremont, A. Recent Advances in Continuum Modeling of Interfacial and Transport Phenomena in Electric Double Layer Capacitors. *J. Electrochem. Soc.* **2015**, *162*, A5158−A5178.
(311) Wang, H.; Thiele, A.; Pilon, L. Simulations of Cyclic Voltammetry for Electric Double Layers in Asymmetric Electrolytes: A Generalized Modified Poisson−Nernst−Planck Model. *J. Phys. Chem. C* **2013**, *117*, 18286−18297.
(312) Wang, H.; Pilon, L. Mesoscale Modeling of Electric Double Layer Capacitors With Three-Dimensional Ordered Structures. *J. Power Sources* **2013**, *221*, 252−260.
(313) Mei, B.-A.; Munteshari, O.; Lau, J.; Dunn, B.; Pilon, L. Physical Interpretations of Nyquist Plots for EDLC Electrodes and Devices. *J. Phys. Chem. C* **2018**, *122*, 194−206.
(314) Wang, H.; Pilon, L. Intrinsic Limitations of Impedance Measurements in Determining Electric Double Layer Capacitances. *Electrochim. Acta* **2012**, *63*, 55−63.
(315) Schammer, M.; Horstmann, B.; Latz, A. Theory of Transport in Highly Concentrated Electrolytes. *J. Electrochem. Soc.* **2021**, *168*, 026511.
(316) Gavish, N.; Elad, D.; Yochelis, A. From Solvent-Free to Dilute Electrolytes: Essential Components for a Continuum Theory. *J. Phys. Chem. Lett.* **2018**, *9*, 36−42.
(317) Jiang, J.; Cao, D.; Jiang, D.-e.; Wu, J. Kinetic Charging Inversion in Ionic Liquid Electric Double Layers. *J. Phys. Chem. Lett.* **2014**, *5*, 2195−2200.
(318) Zhao, H. Diffuse-Charge Dynamics of Ionic Liquids in Electrochemical Systems. *Phys. Rev. E* **2011**, *84*, 051504.
(319) Yochelis, A. Spatial Structure of Electrical Diffuse Layers in Highly Concentrated Electrolytes: A Modified Poisson−Nernst−Planck Approach. *J. Phys. Chem. C* **2014**, *118*, 5716−5724.
(320) Kong, X.; Lu, D.; Liu, Z.; Wu, J. Molecular Dynamics for the Charging Behavior of Nanostructured Electric Double Layer Capacitors Containing Room Temperature Ionic Liquids. *Nano Res.* **2015**, *8*, 931−940.
(321) Gao, J.; Liu, X.; Jiang, Y.; Ding, L.; Jiang, L.; Guo, W. Understanding the Giant Gap Between Single-Pore- And Membrane-Based Nanofluidic Osmotic Power Generators. *Small* **2019**, *15*, 1804279.
(322) Dyatkin, B.; Gogotsi, O.; Malinovskiy, B.; Zozulya, Y.; Simon, P.; Gogotsi, Y. High Capacitance of Coarse-Grained Carbide Derived Carbon Electrodes. *J. Power Sources* **2016**, *306*, 32−41.
(323) Lian, C.; Janssen, M.; Liu, H.; van Roij, R. Blessing and Curse: How a Supercapacitor's Large Capacitance Causes Its Slow Charging. *Phys. Rev. Lett.* **2020**, *124*, 076001.
(324) Gostick, J.; Aghighi, M.; Hinebaugh, J.; Tranter, T.; Hoeh, M. A.; Day, H.; Spellacy, B.; Sharqawy, M. H.; Bazylak, A.; Burns, A.; Lehnert, W.; Putz, A. OpenPNM: A Pore Network Modeling Package. *Comput. Sci. Eng.* **2016**, *18*, 60−74.
(325) Gayon Lombardo, A.; Simon, B. A.; Taiwo, O.; Neethling, S. J.; Brandon, N. P. A Pore Network Model of Porous Electrodes in Electrochemical Devices. *J. Energy Storage* **2019**, *24*, 100736.
(326) Sakaguchi, H.; Baba, R. Electric Double Layer on Fractal Electrodes. *Phys. Rev. E* **2007**, *75*, 051502.
(327) Wang, H.; Varghese, J.; Pilon, L. Simulation of Electric Double Layer Capacitors With Mesoporous Electrodes: Effects of Morphology and Electrolyte Permittivity. *Electrochim. Acta* **2011**, *56*, 6189−6197.
(328) Zhou, M.; Gallegos, A.; Liu, K.; Dai, S.; Wu, J. Insights From Machine Learning of Carbon Electrodes for Electric Double Layer Capacitors. *Carbon* **2020**, *157*, 147−152.
(329) Zhou, M.; Vassallo, A.; Wu, J. Data-Driven Approach to Understanding the In-Operando Performance of Heteroatom-Doped Carbon Electrodes. *ACS Appl. Energy Mater.* **2020**, *3*, 5993−6000.
(330) Gao, T.; Lu, W. Machine Learning Toward Advanced Energy Storage Devices and Systems. *iScience* **2021**, *24*, 101936.
(331) Dawson-Elli, N.; Lee, S. B.; Pathak, M.; Mitra, K.; Subramanian, V. R. Data Science Approaches for Electrochemical Engineers: An Introduction Through Surrogate Model Development for Lithium-Ion Batteries. *J. Electrochem. Soc.* **2018**, *165*, A1−A15.
(332) Li, H.; Zhou, M.; Sebastian, J.; Wu, J.; Gu, M. Efficient force field and energy emulation through partition of permutationally equivalent atoms. *J. Chem. Phys.* **2022**, *156*, 184307.

https://doi.org/10.1021/acs.chemrev.2c00097
Chem. Rev. XXXX, XXX, XXX−XXX